

RADBOUD UNIVERSITEIT NIJMEGEN

MASTER THESIS

Possible Indirect Detection of Dark Matter and its impact on LHC Supersymmetry searches

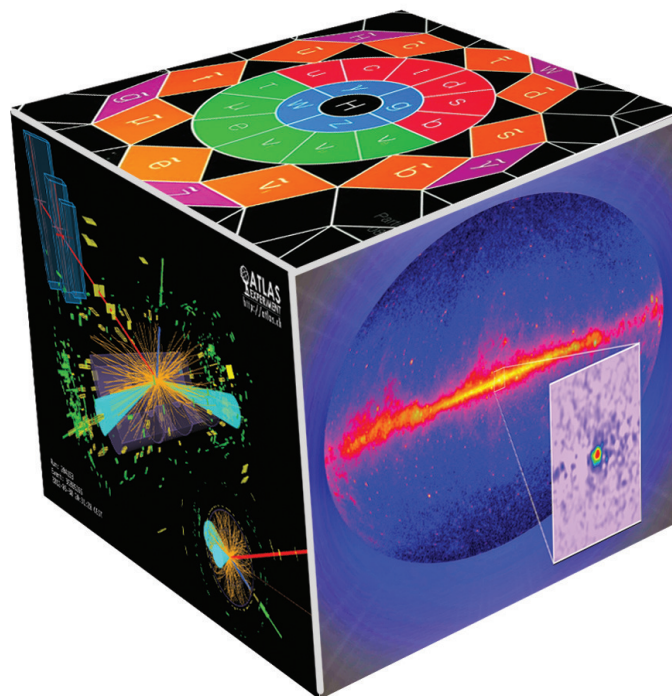
Supervisors:

Melissa van Beekveld

Prof. Dr. Wim Beenakker and

Dr. Sascha Caron

February 2016



Acknowledgements

I can claim, with certainty close to 1, that I have found the most accurate clock in the whole world. The Coma computing cluster, being even more accurate than atomic clocks, decided every Monday morning at 08.43 to stop working. It would report:

```
stale file handle
d????????? ? ? ? astro2
```

After sending the employees of CNCZ a few angry e-mails, I decided to visit them in person when this error appeared for the first time. They would tell me:

"Well, the guy who is supposed to be fixing this problem went home. . . He did not really know what to do about it. . ."

Fortunately, a day later, the CNCZ department managed to solve this problem. However, for some unknown reason, every Monday morning at 08.43, the same error would appear. It took the CNCZ department less time every week to get Coma out of the coma, and at the time of writing this thesis they arrived at a down time of only ~ 30 minutes.

I can not deny that sometimes, I felt exactly like the Coma cluster does each Monday morning at 08.43. Luckily, there are a lot of people who could reanimate me when I was in a state of *stale file handle*. First of all, I would like to thank Sascha and Wim for their efforts and time. Your teaching styles are very different, but both of you challenged me to do the best I ever imagine I could. Without your encouragements, I never would have gotten so far as I am now.

It turned out that useful discussions do not need to be held face-to-face. I had a lot of help from abroad, in the form of Alex Geringer-Sameth and Roberto Ruiz de Austri. I would like to thank you both for helping me with a variety of problems.

Last, but not least, I want to thank everyone who have proofread my thesis: Ruud, David, Bob en Stan. Each of you has delivered a totally independent set of remarks and comments, which made sure that the most shameful errors could be detected and removed. I also want to thank Sijbrand de Jong for agreeing to be the second corrector of my thesis.

Contents

Acknowledgements	ii
Contents	iv
Introduction	1
1 Particle Dark Matter	3
1.1 Evidence	4
1.1.1 Cosmological constraints	5
1.1.2 Distribution	6
1.2 Dark Matter candidates	7
1.2.1 The WIMP miracle	9
2 Supersymmetry	13
2.1 The Standard Model - a brief overview	13
2.1.1 Renormalization	18
2.2 Beyond the Standard Model	19
2.2.1 The hierarchy problem: The problem of a fat Higgs boson	20
2.2.2 Unification of gauge couplings	20
2.3 SUSY to the rescue!	21
2.3.1 Soft SUSY breaking terms	24
2.3.2 Neutralinos and charginos	25
3 Experimental constraints	27
3.1 Direct detection	28
3.2 Indirect detection	30
3.2.1 Dark Matter relic density	34
3.3 Particle accelerator searches	35
4 Annihilating Dark Matter	37
4.1 Astrophysical observations	38
4.1.1 Galactic Center	38
4.1.2 Reticulum II	39
4.2 Explanation in terms of WIMP dark matter	40
4.2.1 Simulation	40
4.2.2 Galactic Center	42
4.2.3 Reticulum II	44

4.3	Concluding remarks	47
5	LHC signature	48
5.1	Characteristics of proton-proton collisions	49
5.2	Tri-lepton final state search channel	51
5.3	Backgrounds to the tri-lepton final state	55
5.4	Monte Carlo generation	56
5.4.1	Expanding the signal set	57
5.5	Distinct features of signal	58
5.5.1	Reducible backgrounds	60
5.6	Signal selection criteria	62
5.6.1	Lepton efficiencies	62
5.6.2	Selection of the OSSF lepton pair	63
5.6.3	Final selection cuts	64
5.7	Results	66
5.7.1	Discussion	67
	Conclusion	71
	A Composition model points	73
	B Sensitivities for different cuts and background assumptions	79
	Acronyms	84
	Bibliography	86

Introduction

More than 3000 years ago, a Greek philosopher called Democritus, laid a fundamental milestone for modern particle physics: the concept of *particles* being indivisible. He believed that small pebbles could never be divided into smaller pebbles, and therefore are the elementary building blocks of everything we see in our world. The meaning of ‘particles’ has changed since then, but the search for a fundamental theory is still there: what are the most elementary building blocks which our world is made of?

The Standard Model of Particle Physics has helped us to gain insight into a possible answer to this question. This theory postulates three generations of quarks and leptons as elementary constituents of matter, which interact via three elementary forces: electromagnetism, the strong force and the weak force. The fourth fundamental force, gravity, is described by the theory of relativity. Despite the successes of the Standard Model, there remain experimental indications that the Standard Model is merely a low-energy realization of another Beyond the Standard Model theory. One widely studied Beyond the Standard Model theory is supersymmetry, which postulates for every Standard Model particle a superpartner, which has the same quantum numbers, but a spin different by $1/2$. A theoretical background for the Standard Model and its minimal supersymmetric extension is provided in chapter 2.

One of the goals of the Large Hadron Collider (LHC) is to search for new particles originating from Beyond the Standard Model theories. The LHC, situated at CERN, is designed to collide protons at a center-of-mass energy of $\sqrt{s} = 14$ TeV. The LHC is installed in a ring tunnel of 26.7 km circumference, ~ 100 meter under the surface of the Earth. Protons are supplied by a linear accelerator, then accelerated by a few consecutive synchrotrons. Eventually, the protons are bunched into the LHC with time spacings of ~ 25 ns. Specialised detectors, such as ATLAS and CMS, observe and reconstruct the interaction events and final state products. The LHC experiments have not yet found any convincing evidence of supersymmetry or other Beyond the Standard Model theories.

This thesis presents a new search strategy for supersymmetric particles with the ATLAS detector at the LHC. We will focus on one particular version of supersymmetry: the Minimal Supersymmetric extension of the Standard Model. The proposed search strategy is inspired by an observation from a different area of physics: the existence of dark matter. Baryonic matter, made up of protons and neutrons, is not the dominant form of material in the universe. The bulk of matter resides in an unknown form, that does not emit light (hence the name). Experimental results hint at dark matter consisting of Beyond the Standard Model particles. Weakly Interacting Massive Particles (WIMPs) are a well motivated class of dark matter particle candidates. A theoretical foundation for WIMPs can for example be found in the context of supersymmetry. In chapter 1 we will

review the evidence for dark matter and possible dark matter candidates. Experimental constraints on WIMPs and supersymmetry originating from astrophysical observations, particle accelerators and direct detection methods are reviewed in chapter 3.

A tantalizing possible astrophysical observation of dark matter comes from our Galactic Center, which shows an unexplained signal of high energetic photons. Large-scale structure formation simulations of galaxies predicts that dark matter is distributed in halos around galaxies. The halos are more dense in areas where the baryonic matter density is higher, such as the Galactic Center. This makes the Galactic Center an ideal region for dark matter annihilation. Could this energetic photon signal originate from dark matter annihilations? How can this observation be linked with particle accelerator experiments and with Beyond the Standard Model theories? These questions will be addressed in chapters 4 and 5 of this thesis.

Conventions

We will adopt natural units where $\hbar = c = 1$ and the Minkowski spacetime metric:

$$\eta_{\mu\nu} = \text{diag}(+1, -1, -1, -1).$$

We will use the specific representation of the 4×4 gamma matrices given by:

$$\gamma^0 = \begin{pmatrix} 0 & \mathbb{1}_2 \\ \mathbb{1}_2 & 0 \end{pmatrix}, \quad \gamma^k = \begin{pmatrix} 0 & \sigma^k \\ \bar{\sigma}^k & 0 \end{pmatrix},$$

where $\mathbb{1}_2$ is the 2×2 identity matrix and σ^k ($k = 1, 2, 3$) are the Pauli spin matrices given by:

$$\sigma^1 = \begin{pmatrix} 0 & 1 \\ 1 & 0 \end{pmatrix}, \quad \sigma^2 = \begin{pmatrix} 0 & -i \\ i & 0 \end{pmatrix}, \quad \sigma^3 = \begin{pmatrix} 1 & 0 \\ 0 & -1 \end{pmatrix},$$

and $\bar{\sigma}^k = -\sigma^k$. We will use the Einstein summation convention whenever there are two repeated indices:

$$x^\mu x_\mu = x^0 x_0 - x^1 x_1 - x^2 x_2 - x^3 x_3.$$

The partial derivative is defined as $\partial_\mu = \frac{\partial}{\partial x^\mu}$. We will use the slashed notation if a gamma matrix is contracted with a four-vector:

$$\not{x} = \gamma^\mu x_\mu$$

In the Standard Model, fermions are described by Dirac spinors (ψ). These objects are four-dimensional. The Dirac adjoint operation is defined as $\bar{\psi} = \psi^\dagger \gamma^0$, such that $\bar{\psi}\psi$ is a scalar. We use $\gamma^5 \equiv i\gamma^0\gamma^1\gamma^2\gamma^3$ to define the chiral projection operators P_L and P_R , where the subscripts indicate ‘left’ and ‘right’ respectively:

$$P_L = \frac{1}{2}(1 - \gamma^5), \quad P_R = \frac{1}{2}(1 + \gamma^5).$$

For a four-component Dirac spinor we can define the left- and right-handed components as:

$$\psi_L = P_L \psi, \quad \psi_R = P_R \psi.$$

Chapter 1

Particle Dark Matter

The standard model for cosmology states that the universe has been and still is expanding from a compressed phase called the *Big Bang*, which started 15 billion years ago. The Big Bang model finds its theoretical basis in combining general relativity with three assumptions: the universe is isotropic, homogeneous and the laws of physics are not unique to our place in the universe. The line element¹ can be parameterized as follows:

$$ds^2 = a^2 \left(\frac{dr^2}{1 - kr^2} + r^2 d\Omega^2 \right),$$

where the curvature parameter k can be negative, zero or positive, depending on whether we live in an open, flat or closed universe respectively. For $k = 0$ we get back Euclidean three-dimensional space. Due to the observed accelerated expansion of the universe, we know that the scale factor a depends on time. From Einstein's field equations, we can find the *Friedmann equation*, which tells us how a evolves in time:

$$\left(\frac{\dot{a}}{a} \right)^2 + \frac{k}{a^2} = \frac{8\pi G_N}{3} \rho_{\text{tot}}, \quad (1.1)$$

where G_N is Newton's constant and ρ_{tot} the total average energy density. Usually, $\frac{\dot{a}}{a}$ is replaced by $H(t)$, the Hubble parameter. Observations tell us that the present value, indicated by H_0 , is 67.8 ± 0.7 (km/s)/Mpc [1]. In this framework, the dimensionless Hubble parameter is often introduced, denoted by h , allowing us to write Hubble's parameter as $H_0 = h \cdot 100$ km s⁻¹ Mpc⁻¹.

We see from equation 1.1 that the universe is flat when the total energy density equals $\frac{3H^2}{8\pi G_N}$, a value indicated by the *critical density* ρ_c . Usually the current energy density of the universe is indicated by Ωh^2 , where $\Omega = \frac{\rho_{\text{tot}}}{\rho_c}$ and thus can be seen as the fraction of the total energy density to the critical density. Hence, $\Omega = 1$ is equivalent to having a flat universe.

Different forms of energy density exist: matter energy density (Ω_M) and vacuum energy density (Ω_Λ). The sum of these densities is indicated by Ω .

Observations such as the expansion of the universe and the *Cosmic Microwave Background* (CMB) support this standard model for cosmology. Other astrophysical observations suggest that Ω_M might be composed of two components: one visible baryonic component and one in the form of a large amount of non-luminous matter, matter which

¹The squared distance between points at a fixed time.

in cosmology is referred to as *dark matter* (DM). Although the existence of dark matter is accepted by most physicists, its nature remains unknown.

This chapter is organized as follows. First we will briefly review the evidence for dark matter. Then we will look at dark matter candidates. Finally we will look at the production mechanism in the early universe. The material of this chapter is based on ref. [2–7].

1.1 Evidence

The clearest evidence for the existence of dark matter comes from the observation of rotation curves of galaxies. By invoking Newtonian dynamics we find that the tangential velocities of stars (v) as function of their distance from the galactic center (r) is:

$$v = \sqrt{\frac{G_N M(r)}{r}}, \quad (1.2)$$

where G_N denotes Newton’s constant, $M(r) = 4\pi \int \rho(r)r^2 dr$ and $\rho(r)$ is the mass density profile. We expect $M(r)$ to be constant at large distance r , which means that the velocity will drop as $v \propto 1/\sqrt{r}$. We observe however that $v(r)$ shows little sign of falling off (figure 1.1(a)), which implies the existence of more matter than we observe. We observe that the rotation curves are flat at large radii, implying $M(r) \propto r$, which can be achieved if the mass density obeys a density profile of the form $\rho \propto \frac{1}{r^2}$ at large r .

According to general relativity, the curvature of space-time caused by a large amount of matter results in a deflection of light rays, a phenomenon called *gravitational lensing*. The deflection angle is proportional to the mass of the lens, so this can be used to probe the lens’ mass by observing the deflection of light originating from background objects.

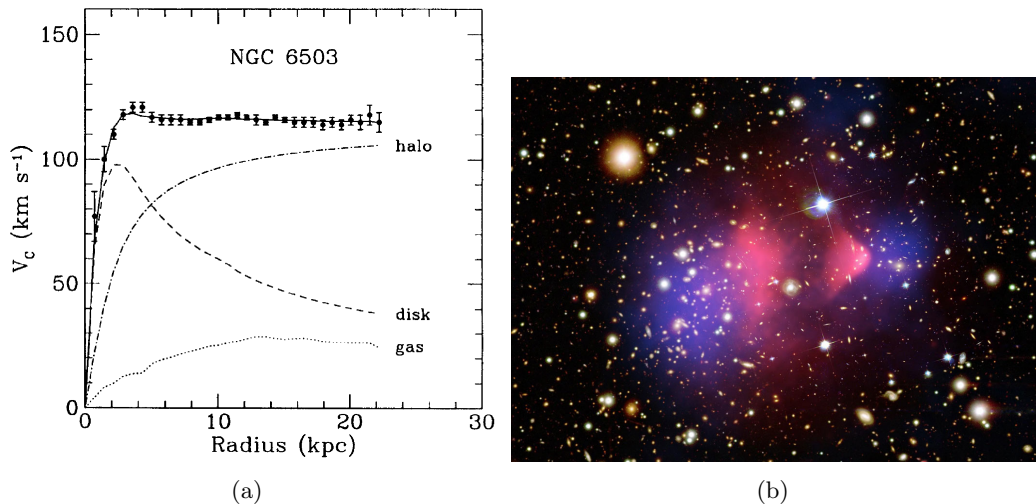


FIGURE 1.1: *Left*: Rotation curve of NGC 6503. The dotted, dashed and dash-dotted lines are from the contribution of gas, disk and dark matter respectively. Extracted from ref. [8]. *Right*: Observations from the Bullet Cluster. Hot gas observed in X-ray frequencies is indicated in red, dark matter inferred from gravitational lensing is indicated in blue.

An example of gravitational lensing can be found in the Bullet Cluster (figure 1.1(b)). This cluster consists of two separate galaxy clusters that have recently collided. Each component, being stars, gas and dark matter, behaves differently during the collision. In the collision, gas, observable in X-ray frequencies, interacts and slows down (indicated in red in the figure). The stars, observable in visible light, are not affected by the collision other than gravitationally. The total matter in the colliding clusters can be inferred from gravitational lensing. This reveals that most matter resides at the edges of the clusters, however in an invisible form (indicated in blue in the figure). The dark matter bypassed the gas during the collision, which implies that it is weakly interacting.

1.1.1 Cosmological constraints

The observations discussed so far cannot determine the total amount of dark matter in the universe. This information can however be extracted from the CMB. These photons were created when the first neutral atoms formed, approximately 300,000 years after the Big Bang in an epoch called *recombination*. The existence of photons originating from the early universe was predicted by George Gamov et al. in 1948 and later accidentally discovered by Penzias and Wilson in 1965 [9]. The high degree of isotropy in the CMB hints at an era of inflation: a time in which the universe expanded rapidly. Inflation solves the *flatness problem*, allowing k to take any value in the early universe as inflation forces k very close to 0 after this era. After its discovery, searches began for anisotropies in the CMB, as these anisotropies give the normalization of the density perturbations in the early universe, shortly after recombination. It wasn't until 1992 that the Cosmic Background Explorer (COBE) mapped these anisotropies, later followed by the Wilkinson Microwave Anisotropy Probe (WMAP, 2003) satellite and, very recently, the Planck satellite (2013). The latter reports of a dark matter relic density of $\Omega_{\text{DM}}h^2 = 0.1198 \pm 0.0026$ [1], where $h = H_0/(100 \text{ km/s per Mpc}) \simeq 0.68$ with H_0 the Hubble constant.

According to structure formation simulations, gravitational instability caused a growth of the density fluctuations over time. However, this growth can only be linear in the scale factor a and could only have started after recombination. We observe however much larger anisotropies in the present universe.

Non-baryonic dark matter can solve this problem, as this causes the perturbations to start to grow earlier. At the time of recombination, dark matter has already created gravitational wells for baryonic matter to fall into. For this theory to work, dark matter needs to be heavy (to ensure it is not relativistic at the time structure formation starts).

1.1.2 Distribution

Large-scale simulations, such as N-body simulations for rotation curves of galaxies, predict that dark matter is concentrated in halos around galaxies. Since 1995, when Navarro, Frenk and White proposed the first dark matter density profile [7], many phenomenological density profiles have been proposed [10]:

$$\begin{aligned} \text{NFW: } \rho_{\text{NFW}}(r) &= \rho_s \frac{r_s}{r} \left(1 + \frac{r}{r_s}\right)^{-2} \\ \text{Einasto: } \rho_{\text{Ein}}(r) &= \rho_s e^{-\frac{2}{\alpha} \left(\left(\frac{r}{r_s}\right)^\alpha - 1\right)} \\ \text{Isothermal: } \rho_{\text{Iso}}(r) &= \frac{\rho_s}{1 + (r/r_s)^2} \\ \text{Burkert: } \rho_{\text{Bur}}(r) &= \frac{\rho_s}{(1 + r/r_s)(1 + (r/r_s)^2)} \\ \text{Moore: } \rho_{\text{Moo}}(r) &= \rho_s \left(\frac{r_s}{r}\right)^{1.16} \left(1 + \frac{r}{r_s}\right)^{-1.84}, \end{aligned}$$

where we denote r as the distance from the galactic center, r_s as a ‘typical’ scale radius and ρ_s as a ‘typical’ scale density. The resulting DM density profiles are shown in figure 1.2.

Usually, r_s and ρ_s are fixed by imposing that the resulting profiles satisfy observational results. For example, we require the density of dark matter at the location of our Sun ($r_\odot \sim 8.5\text{kpc}$) to be $\rho_\odot \sim 0.3 \text{ GeV/cm}^3$. There are also constraints on the total dark matter mass contained within a certain distance. Furthermore, α parameterizes the steepness of the Einasto profile (smaller α leads to steeper profiles). Dark matter simulations that include the effects of baryons usually result in profiles that are steeper towards the Galactic Center with respect to simulations where these effects are ignored. All profiles assume spherical symmetry and do not consider the potential contribution of dark matter substructures. Throughout this thesis, we will assume this as well.

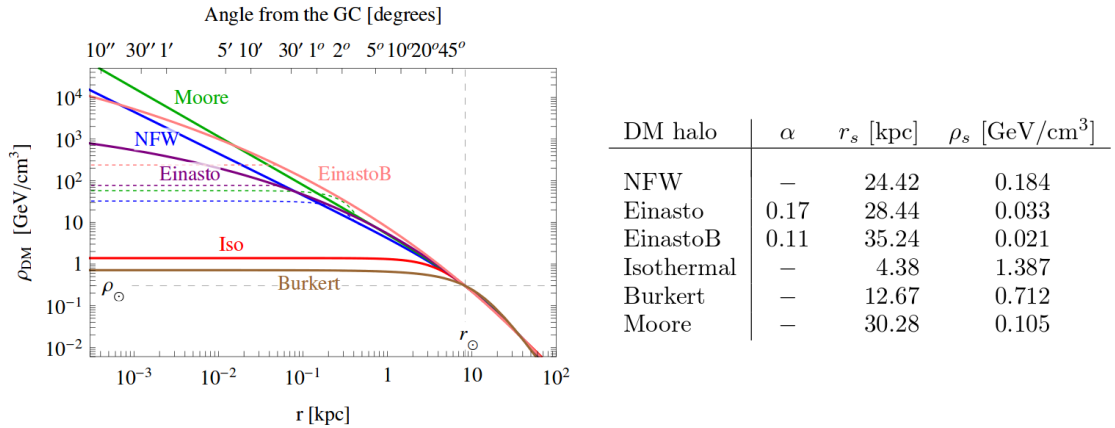


FIGURE 1.2: *Left*: different dark matter density profiles as a function of r , the distance from the Galactic Center. *Right*: Dark matter density profiles and the corresponding parameters. Extracted from ref. [10]

In simulations, a universal dark matter density profile is often used [4]:

$$\rho(r) = \frac{\rho_s}{(r/r_s)^\gamma (1 + (r/r_s)^\alpha)^{(\beta-\gamma)/\alpha}}, \quad (1.3)$$

where, for example, $(\alpha, \beta, \gamma) = (1.0, 3.0, 1.0)$ results in the classic NFW profile. Depending on the input parameters of the simulations, some show that the slope of the density profile increases when moving further away from the inner core. However, the value of the power-law index in the inner core lies heavily under debate. Other simulations suggest that density profiles do not converge to any specific power-law at small distances [11].

1.2 Dark Matter candidates

To be considered a candidate for dark matter, any proposed particle must satisfy the following criteria:

- Dark matter must be weakly interacting (limits on self-interaction are found in e.g. the Bullet cluster).
- Dark matter was probably non-relativistic (or cold) during the formation of large scale structures, as relativistic particles would cause the universe to be less clumpy than it is today.
- Dark matter must be mostly non-baryonic, as the total amount of baryonic matter is less than the total matter energy density Ω_M .
- Dark matter must be stable (on timescales comparable to the age of the universe), or its destruction and formation must be in equilibrium.

Since 1998, neutrinos have been considered as excellent dark matter candidates because they are known to have mass. However, the neutrino masses are too small to make up for all of the dark matter mass density. The upper bound on the total neutrino relic density is $\Omega_\nu h^2 \lesssim 0.07$ [4].

Other objects have been suggested to account for the dark matter density, but in a *hidden* form. Examples of these include MACHOs (*Massive Compact Halo Objects*). These are for example brown dwarf stars, big planets and black holes. Microlensing has been used to search for these objects, but there are not enough structures observed to account for all dark matter. However, these objects can make up a small fraction of the total amount of dark matter.

Other candidates that have been proposed have masses ranging between 10^{-5} eV to $10^4 M_\odot$. The most popular candidates will be discussed below. Note that these candidates do not exclude one another, every discussed candidate can contribute to the total amount of DM.

Sterile neutrinos: Sterile neutrinos are neutrinos that do not interact with any force except the gravitational force. Sterile neutrinos can act as the mass-generating mechanism for left-handed neutrinos. For a decade we know through the observation of neutrino oscillations that neutrinos have a small but finite mass. An explanation for this fact could be given by the *see-saw mechanism*.

The neutrino mass is in itself an intriguing subject. As soon as we allow for a right-handed neutrino, we can write down a Dirac mass term (indicated by M_D) just like for all the other standard model particles. However, the right-handed neutrino does not interact with any of the gauge fields, allowing us to write down a Majorana mass term (indicated by M_M) for the right-handed neutrinos as well:

$$\bar{\nu}_R M_D \nu_L + \bar{\nu}_L M_D \nu_R + \frac{1}{2} \bar{\nu}_R M_M \nu_R^c + \frac{1}{2} \bar{\nu}_R^c M_M \nu_R,$$

introducing a mass matrix of the form:

$$\frac{1}{2} \begin{pmatrix} 0 & M_D \\ M_D & M_M \end{pmatrix}.$$

This matrix can be diagonalized, which leads to mass eigenvalues $\frac{1}{4}(M_M \pm \sqrt{M_M^2 + 4M_D^2})$. Assuming that $M_D \ll M_M$, this results in two eigenvalues which are approximately $\frac{1}{2}M_M$ and $\frac{-M_D^2}{2M_M}$: one very massive and one very light neutrino. The very massive neutrino can be considered as a dark matter candidate. For this to work, the sterile neutrino cannot be too heavy, as it would completely decouple from the light neutrino. In that case, the heavy neutrino would not be able to annihilate.

Weakly-interacting massive particles (WIMPs): A WIMP is any particle that interacts with a strength of the order of the weak-force interaction and has a mass that is near the weak scale (between 10 GeV and a few TeV). This class of candidates is particularly interesting because of the *WIMP miracle* as explained in section 1.2.1. It is also probably the largest class of DM particles, as it consists of hundreds of suggested particles. In this thesis, we will consider the lightest supersymmetric particle (LSP) in the Minimal Supersymmetric extension of the Standard Model with exact R-parity (which guarantees that the LSP is stable) as the DM particle. More on this particular candidate can be found in chapter 2.

Axions: These particles are pseudo-scalars associated with the spontaneous breaking of the Peccei-Quinn U(1) symmetry. This symmetry is introduced to solve the strong-CP problem of quantum chromodynamics. Axions are less natural than WIMPs because it is hard to get their number density to match the observed dark matter density.

Other particles with only gravitational interactions: There is always the possibility that DM is very heavy and only interacts via the gravitational force with ordinary matter. This makes DM as a particle almost impossible to observe, a very boring scenario for particle physics indeed!

None of the above: We only have considered particle dark matter candidates here, but there are still other possibilities left. In one of such theories, modified Newtonian dynamics (MOND), the laws of gravity are changed. However, the observation of the Bullet Cluster, poses a challenge for MOND, as MOND would expect the missing mass to reside in the center of the two colliding clusters.

1.2.1 The WIMP miracle

The creation of particles in the early universe can be realized thermally or non-thermally (in a phase transition much like the Higgs mechanism). The resulting thermal and non-thermal relics have a different relationship between their relic density Ω and properties such as mass and couplings.

WIMPs are assumed to be a thermal relic. The early universe was a dense and hot place where all the particles were in thermal equilibrium. The annihilation rate (Γ) per particle in this universe is given by:

$$\Gamma = n\sigma v,$$

where n is the number density of particles, σ is the cross section and v is the relative velocity.

As the universe expands and cools down, the gas of particles becomes too dilute which means that DM particles cannot find each other to annihilate. Furthermore, insufficient kinetic (thermal) energy is available to produce new heavy particles. This process is called a *freeze out* and the number of particles will approach a constant: the thermal relic density Ωh^2 . We will define the freeze out to be the time when:

$$\Gamma = H \tag{1.4}$$

is satisfied [12].

From statistical mechanics we know that the number density of a particle of mass m in thermal equilibrium with a thermal bath of temperature T has two asymptotic regimes:

$$\begin{aligned} n_{rel} &\sim T^3 \text{ for } m \ll T, \\ n_{non-rel} &\sim (mT)^{\frac{3}{2}} e^{-\frac{m}{T}} \text{ for } m \gg T. \end{aligned}$$

Since we consider cold dark matter, we are in the non relativistic regime. If the expansion of the Universe were so slow that thermal equilibrium was always maintained, the number of WIMPs would be very small. Fortunately, the Universe is not static.

We can use a Boltzmann equation to give an expression for the number density of a particle over time. There are three processes that influence the WIMP number density: 1) the expansion of the universe (which causes dilution) and 2) annihilation from $\chi\chi \rightarrow SM$ or 3) creation from $SM \rightarrow \chi\chi$. These processes result in the following Boltzmann equation:

$$\frac{dn}{dt} = -3Hn - \langle\sigma v\rangle(n^2 - n_{eq}^2), \tag{1.5}$$

where n is the number density of the dark matter particle χ , H is the Hubble constant, $\langle\sigma v\rangle$ is the thermally averaged annihilation cross section weighted by the absolute value of the relative velocity and n_{eq} the dark matter number density in thermal equilibrium. Note that we do not include coannihilation processes ($\chi\chi' \rightarrow SM$ and vice versa, where χ' is another DM or SM particle).

Starting at an early time when all particles were in equilibrium, the number density we observe today can be calculated by integrating this equation. The relic abundance is then simply $\Omega_\chi = \frac{m_\chi n_\chi}{\rho_c}$.

To solve the equation numerically, equation 1.5 is usually reformulated in terms of $Y = n/s$, the ratio of particle and entropy density and $x = m_\chi/T$, the ratio of the mass of the DM particle and the temperature [12]. The time derivative of Y is:

$$\frac{dY}{dt} = \frac{d}{dt} \left(\frac{n}{s} \right) = \frac{dn}{dt} \frac{1}{s} - \frac{n}{s^2} \frac{ds}{dt}. \quad (1.6)$$

We assume the conservation of entropy per comoving volume ($sa^3 = \text{constant}$, where $a(t)$ is the scale factor) to determine the time derivative of s :

$$\begin{aligned} 0 = \frac{d}{dt}(sa^3) &= \frac{ds}{dt}a^3 + 3a^2 \frac{da}{dt}s \\ \rightarrow \frac{ds}{dt} &= -3Hs. \end{aligned}$$

Inserting equation 1.5 in equation 1.6, we obtain:

$$\frac{dY}{dt} = -s\langle\sigma v\rangle(Y^2 - Y_{eq}^2).$$

The right-hand side depends only on temperature, so we will use x as an independent variable instead of t :

$$\begin{aligned} \frac{dY}{dt} &= \frac{dx}{dt} \frac{dY}{dx} \\ &= -\frac{m_\chi}{T^2} \frac{dT}{dt} \frac{dY}{dx} \\ &= \frac{x^2}{m_\chi} \cdot 3Hs \frac{dT}{ds} \frac{dY}{dx}. \end{aligned}$$

This results in the equation:

$$\frac{dY}{dx} = -\frac{m_\chi}{x^2} \frac{1}{3H} \frac{ds}{dT} \langle\sigma v\rangle (Y^2 - Y_{eq}^2). \quad (1.7)$$

Now using the Friedmann equation in a radiation dominated universe for which $H^2 = \frac{8\pi G_N}{3}\rho$, $\rho \propto T^4$ and $s \propto T^3$, we obtain:

$$\frac{dY}{dx} \sim \frac{m_\chi}{x^2} \langle\sigma v\rangle (Y^2 - Y_{eq}^2). \quad (1.8)$$

Figure 1.3 shows an approximation. The y-axis is proportional to the relic density, the solid line is the thermal equilibrium value. The dashed line is the relic density at the moment of freeze out, derived by integrating equation 1.8 from $x = 0$ to $x_0 = m_\chi/T_0$, the present day ratio, to find Y_0 (which is directly related to the present day relic density). For a rigorous derivation, see ref. [2] or ref. [3]. If the velocity-weighted annihilation cross section $\langle\sigma v\rangle$ gets larger, the relic density will result in a lower value.

It is instructive to look at a more qualitative picture. Assuming a flat universe, we can use the Friedmann equation to relate the Hubble parameter to the energy density as:

$$H^2 = \frac{8\pi G_N}{3}\rho,$$

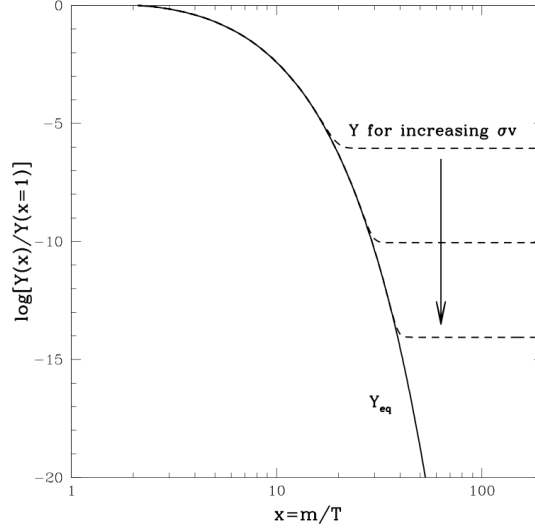


FIGURE 1.3: The evolution of the relic density as function of x as extracted from ref. [13].

where $\frac{1}{\sqrt{8\pi G_N}} = M_P$, the Planck mass. In the radiation dominated epoch, $\rho \sim T^4$, so thermal decoupling occurs when $H \sim \frac{T^2}{M_P}$. The condition $n\langle\sigma v\rangle \sim H$ (the freeze out condition as given in equation 1.4) then yields:

$$n_f \sim \frac{T_f^2}{M_P\langle\sigma v\rangle},$$

where the subscript f denotes freeze out. Now we substitute the number density for non-relativistic particles for n_f :

$$(m_\chi T_f)^{\frac{3}{2}} e^{-\frac{m_\chi}{T_f}} \sim \frac{T_f^2}{M_P\langle\sigma v\rangle}$$

$$x_f = \frac{m_\chi}{T_f} \rightarrow \sqrt{x_f} e^{-x_f} \sim \frac{1}{m_\chi M_P\langle\sigma v\rangle}.$$

If we substitute values for an electroweakly interacting relic particle where $\sigma \sim G_F^2 m_\chi^2$ and $m_\chi \sim 10^2$ GeV, we get $x_f \sim 20$. The dark matter relic density is given by:

$$\Omega_\chi = \frac{m_\chi n_\chi(T = T_0)}{\rho_c} = \frac{m_\chi T_0^3}{\rho_c} \frac{n_0}{T_0^3}$$

$$\sim \frac{m_\chi T_0^3}{\rho_c} \frac{n_f}{T_f^3} = \frac{T_0^3}{\rho_c M_P} \frac{x_f}{\langle\sigma v\rangle},$$

where the subscript 0 denotes present day quantities ($T_0 = 2.75$ K). We can use that $\frac{n_0}{T_0^3} \sim \frac{n_f}{T_f^3}$, since $n \propto T^3 x^{\frac{3}{2}} e^{-x}$ and $x \gg 1$, making $n \propto T^3$. Plugging in various constants (depending on the exact temperature at the moment of freeze out) we get [14]:

$$\Omega h^2 \simeq \frac{(1.8 - 4.5) \times 10^{-27} \text{ cm}^3/\text{s}}{\langle\sigma_{\text{ann}} v\rangle}. \quad (1.9)$$

The Planck satellite measures a DM relic density of $\Omega_{DM} h^2 = 0.118$, so we need $\langle\sigma v\rangle \simeq (2 - 5) \times 10^{-26} \text{ cm}^3 \text{ s}^{-1} \sim 1 \text{ pb}$ to get the correct relic density. A cross section of 1 pb

is a typical cross section for weak-scale interactions and with particle masses around $m_\chi \sim 100 - 1000$ GeV. This fact is called the *WIMP miracle*: weak-scale particles with weak-scale interactions make excellent dark matter candidates.

Chapter 2

Supersymmetry

This chapter describes our current understanding of the Standard Model (SM) of particle physics, a theory that describes electromagnetic, weak and strong interactions. A brief theoretical overview is presented, followed by a summary of its shortcomings. Subsequently, the theory of supersymmetry (SUSY), one of several beyond the SM postulated theories, will be presented. We will specifically address the minimal extended supersymmetric version of standard model (the MSSM).

We will describe the SM briefly here, for a more thorough explanation I gladly refer to the lectures of Bert Schellekens, or see e.g. [15] or [16].

2.1 The Standard Model - a brief overview

The Standard Model is a quantum field theory where each particle is described in terms of a field with specific transformation properties under the Lorentz group. Dynamics in field theories are described via a Lagrangian density (\mathcal{L}), or Lagrangian in short. Let us construct a field theory that is invariant under local transformations, starting from the free massless Dirac Lagrangian:

$$\mathcal{L} = i\bar{\psi}\not{\partial}\psi,$$

which describes a massless spin 1/2 particle ($\psi \equiv \psi(x)$) that transform as a spinor under the Lorentz transformations. We impose a global phase transformation (U(1)):

$$\psi \rightarrow e^{iq\alpha}\psi; \bar{\psi} \rightarrow e^{-iq\alpha}\bar{\psi},$$

where q is a quantity that indicates the strength of the transformation. The Lagrangian remains invariant if we impose this transformation. However, if we consider a local phase transformation:

$$\psi \rightarrow e^{iq\alpha(x)}\psi; \bar{\psi} \rightarrow e^{-iq\alpha(x)}\bar{\psi},$$

the Lagrangian is no longer invariant, as $\mathcal{L}' = \mathcal{L} - q\bar{\psi}\not{\partial}\alpha(x)\psi$. In order to make the Lagrangian invariant under local phase transformations, we want to add new terms that compensate for the extra term $-q\bar{\psi}\not{\partial}\alpha(x)\psi$. We therefore introduce a covariant

derivative, which replaces the ordinary derivative:

$$D_\mu \psi \equiv (\partial_\mu + iqA_\mu)\psi,$$

where $A_\mu \rightarrow A'_\mu = A_\mu - \partial_\mu \alpha(x)$.

This is called a *gauge transformation*, and the Lagrangian is made *gauge invariant*. The requirement of local gauge invariance has now led us to introduce the gauge field A_μ . The Lagrangian is now no longer free, but describes an interaction of a spin 1/2 particle with the gauge field A_μ . If we assume that A_μ describes a spin-1 particle, we should add the kinetic term for massless spin-1 particles to the interacting Dirac Lagrangian and obtain:

$$\mathcal{L}_{\text{QED}} = i\bar{\psi}\not{D}\psi - \frac{1}{4}F_{\mu\nu}F^{\mu\nu}.$$

This is the Lagrangian for quantum electrodynamics (QED), with the field strength tensor $F_{\mu\nu} = \partial_\mu A_\nu - \partial_\nu A_\mu$. We can identify A_μ as the electromagnetic potential and q as the electromagnetic charge. Adding a mass term for the spin-1 field ($m^2 A_\mu A^\mu$) would break gauge invariance. Hence, if a massive gauge field is observed, we need to introduce its mass in another way in order to preserve gauge invariance.

It is straightforward to extend this scheme for non-abelian groups, for which the generators of the Lie algebra do not commute. In that case, the fermionic fields must be constructed in a way that the gauge transformations can act on them, which means that these fields should transform according to representations of the imposed gauge group:

$$\psi = \begin{pmatrix} \psi_1 \\ \psi_2 \\ \vdots \\ \psi_n \end{pmatrix}, \quad \psi^f \rightarrow \psi'^f = U^{fg}\psi^g,$$

where U^{fg} are the components of a unitary matrix of the group $\text{SU}(N)$. Any unitary matrix can be written as the exponent of $N^2 - 1$ generators (T^a) of the Lie-algebra: $U = e^{i\alpha^a T^a}$. The covariant derivative that follows from postulating a $\text{SU}(N)$ gauge invariance is:

$$D_\mu = \partial_\mu + igT^a A_\mu^a,$$

where A_μ^a are the gauge fields and g the coupling constant. Note that for every generator, we get a gauge field. The field strength tensor for A_μ^a is given by:

$$F_{\mu\nu}^a = \partial_\mu A_\nu^a - \partial_\nu A_\mu^a - gf^{abc}A_\mu^b A_\nu^c,$$

where f^{abc} are the *structure constants*, originating from the commutation relations of two generators: $[T^a, T^b] = if^{abc}T^c$. Note that the generators in general do not commute, which implies self-interactions between the gauge fields due to their kinetic term in the Lagrangian.

The gauge group of the Standard Model is:

$$\text{SU}(3)_C \otimes \text{SU}(2)_L \otimes \text{U}(1)_Y,$$

where C denotes color charge, L left-handed fields and Y the hypercharge. The SM Lagrangian must be invariant under local transformations of this gauge group.

Particles that are described by the SM fall into two categories: particles that make up matter (*fermions*) and particles that serve as force carriers (*gauge bosons*). In addition, the SM incorporates the Higgs boson, a scalar particle which plays a role in understanding massive particles. All SM particles and the corresponding gauge fields are summarized in table 2.1. The representations under the gauge group for all fields is also presented in table 2.1.

The SM includes 12 elementary matter particles, which are spin-1/2 particles. Each of these particles has an antiparticle, which possesses opposite charge quantum numbers. Fermions come in two different categories: quarks and leptons, a distinction which is based on their interaction with different gauge bosons. There are six quark flavors: up (u), down (d), charm (c), strange (s), top (t) and bottom (b), and six leptons: electron (e), electron neutrino (ν_e), muon (μ), muon neutrino (ν_μ), tau (τ) and tau neutrino (ν_τ). Pairs of quarks and leptons are grouped together to form a generation, e.g. u , d , ν_e and e form the first generation.

Forces are mediated by the exchange of gauge bosons, which are spin-1 particles. The carrier of the electromagnetic interaction is the photon (γ). The carriers of the electroweak interaction are the W^\pm and Z bosons. The strong force is carried by the gluons (g).

Particles	Fields	Content	Charge	Spin	$\text{SU}(3) \otimes \text{SU}(2)_L \otimes \text{U}(1)_Y$
Quarks (3 generations)	Q_i	$(u, d)_L$	$(2/3, -1/3)$	1/2	$\mathbf{3} \otimes \mathbf{2} \otimes 1/6$
	u_{Ri}	u_R	2/3	1/2	$\mathbf{3} \otimes \mathbf{1} \otimes 2/3$
	d_{Ri}	d_R	-1/3	1/2	$\mathbf{3} \otimes \mathbf{1} \otimes -1/3$
Leptons (3 generations)	L_i	$(\nu_e, e)_L$	$(0, -1)$	1/2	$\mathbf{1} \otimes \mathbf{2} \otimes -1/2$
	e_{Ri}	e_R	-1	1/2	$\mathbf{1} \otimes \mathbf{1} \otimes -1$
Gluons	G_μ^a	g	0	1	$\mathbf{8} \otimes \mathbf{1} \otimes 0$
$W_{1,2,3}$ bosons	W_μ^j	$W^\pm, (Z^0, \gamma)$	$\pm 1, 0$	1	$\mathbf{1} \otimes \mathbf{3} \otimes 0$
B boson	B_μ	(Z^0, γ)	0	1	$\mathbf{1} \otimes \mathbf{1} \otimes 0$
Higgs boson	(ϕ^+, ϕ^0)	h	$(+, 0)$	0	$\mathbf{1} \otimes \mathbf{2} \otimes 1/2$

TABLE 2.1: Particle content of the Standard Model with the corresponding fields, charge, spin and the representation of the field in the $\text{SU}(3) \otimes \text{SU}(2)_L \otimes \text{U}(1)_Y$ gauge group. Note that the right-handed neutrino is not included. The fields W_μ^3 and B_μ are mixed into two electromagnetically neutral mass-eigenstates: the massive Z boson and the massless photon (γ).

Quantum Chromodynamics (QCD): The strong interaction arises from an SU(3) gauge group, which has 8 generators corresponding to the gauge bosons we call gluons. Gluons couple to six quark flavors, each in the triplet representation of SU(3) with quantum numbers *red*, *blue* and *green* called *colors*. The massless Lagrangian is written as:

$$\mathcal{L}_{\text{QCD}} = i\bar{\psi}^f \gamma^\mu (\partial_\mu + ig_s G_\mu^a T^a) \psi^f - \frac{1}{4} G_{\mu\nu}^a G^{a,\mu\nu}, \quad (2.1)$$

where f runs over all the quark flavors and a from 1 to 8. The 8 matrices T^a are the generators of the SU(3) group in the triplet representation and g_s is the strong coupling constant. The gluon and fermion-fields are represented by G^a and ψ^f respectively. As gluons themselves carry color charge they are also able to self interact. The field strength is given by:

$$G_{\mu\nu}^a = \partial_\mu G_\nu^a - \partial_\nu G_\mu^a - g_s f_{abc} G_\mu^b G_\nu^c,$$

where f_{abc} are the structure constants.

QCD has two special properties: *asymptotic freedom* and *confinement*. Asymptotic freedom arises from the fact that the strength of the coupling decreases with higher energy, causing quarks and gluons to interact very weakly at high energies, but very strongly at low energies. Confinement means that free particles are always color neutral, causing quarks to form bound states called *hadrons*. Such colorless states can be constructed from three quarks (*baryons*), or one quark and one anti-quark (*mesons*). Most hadrons are unstable and decay very quickly. One notable exception to this rule is the proton, containing two up quarks and one down quark, which has a lifetime that is larger than the age of the universe.

Electroweak theory: Electroweak interactions arise from the SU(2)_L ⊗ U(1)_Y gauge symmetry. These groups have a total of 4 generators, which correspond to the electroweak eigenstates $W_\mu^j \equiv W_\mu^{1,2,3}$ from SU(2)_L and B_μ from U(1)_Y. The subscript L indicates the left-handed nature of this interaction, as the SU(2)_L gauge bosons only couple to left handed fermions (ψ_L). These fermions appear as quark and lepton doublets in the electroweak theory, as shown in table 2.1. The right-handed fermion fields (ψ_R) appear as singlets under SU(2). The massless Lagrangian can be written as:

$$\mathcal{L}_{\text{EW}} = i\bar{\psi}_L \not{D}_L \psi_L + i\bar{\psi}_R \not{D}_R \psi_R - \frac{1}{4} W_{\mu\nu}^j W^{j,\mu\nu} - \frac{1}{4} B_{\mu\nu} B^{\mu\nu}. \quad (2.2)$$

The field strength tensors are given by:

$$\begin{aligned} W_{\mu\nu}^j &= \partial_\mu W_\nu^j - \partial_\nu W_\mu^j - g\epsilon_{jkl} W_\mu^k W_\nu^l \\ B_{\mu\nu} &= \partial_\mu B_\nu - \partial_\nu B_\mu, \end{aligned}$$

where ϵ_{jkl} is the Levi-Civita symbol. The covariant derivatives have the following form:

$$\begin{aligned} D_{\mu,L} &= \partial_\mu + \frac{i}{2} g \sigma^j W_\mu^j + ig' Y B_\mu \\ D_{\mu,R} &= \partial_\mu + ig' Y B_\mu. \end{aligned}$$

where g and g' are the bare coupling constants of SU(2)_L and U(1)_Y respectively. The Pauli matrices σ^j and the hypercharge Y are the generators of these symmetries.

Electroweak symmetry breaking: All gauge fields in equation 2.2 are massless, which is in contradiction with what we see in experiment. The Higgs mechanism solves this issue. In this procedure, we add an extra complex scalar boson to the SM, represented by the field ϕ , which we put in a color neutral doublet with hypercharge 1/2. This is added to the SM Lagrangian via:

$$\mathcal{L}_{\text{Higgs}} = (D_\mu \phi)^\dagger D^\mu \phi - \mu^2 (\phi^\dagger \phi) - \lambda (\phi^\dagger \phi)^2 \equiv (D_\mu \phi)^\dagger D^\mu \phi - V(\phi). \quad (2.3)$$

If we demand $\mu^2 < 0$ and $\lambda > 0$, two ground states for the potential $V(\phi)$ are found: $\langle |\phi| \rangle_0 = 0$ (unstable) and $\langle |\phi| \rangle_0 = \sqrt{\frac{-\mu^2}{2\lambda}} \equiv \frac{v}{\sqrt{2}}$ (stable), where $\langle |\phi| \rangle_0 \equiv \langle 0 | |\phi| | 0 \rangle$ is referred to as the vacuum expectation value (*v.e.v.*). Due to gauge freedom we can pick $\langle \phi \rangle_0 = (0, v/\sqrt{2})$ as the ground state. In the unitary gauge we expand $\phi = \frac{1}{\sqrt{2}}(0, v + h)$, with h a real scalar field, giving rise to mass terms for the gauge bosons. These gauge bosons can be rewritten in mass eigenstates:

$$\begin{aligned} W_\mu^\pm &= \frac{1}{\sqrt{2}}(W_\mu^1 \mp iW_\mu^2) \\ Z_\mu^0 &= \frac{1}{\sqrt{g'^2 + g^2}}(gW_\mu^3 - g'B_\mu) \\ A_\mu &= \frac{1}{\sqrt{g'^2 + g^2}}(g'W_\mu^3 + gB_\mu), \end{aligned}$$

which we recognize as the W bosons, Z boson and the photon.

We can understand what has happened here on a physical level. We started with a complex scalar boson with four real degrees of freedom (d.o.f.). Three of these have been absorbed in giving mass to the W and Z bosons, as a massive gauge boson has three d.o.f. while a massless gauge boson has only two. The remaining d.o.f. corresponds to a new scalar that we call the Higgs boson.

Fermionic mass terms: Due to gauge invariance, mass terms of the form $\bar{\psi}_L \psi_R$ were forbidden before electroweak symmetry breaking. With the Higgs field we can write down a coupling of the fermions to this scalar field without breaking the gauge symmetries:

$$\mathcal{L}_{\text{Yukawa}} = -\mathbf{y}_u \bar{Q} \phi^c u_R - \mathbf{y}_d \bar{Q} \phi d_R - \mathbf{y}_e \bar{L} \phi e_R + h.c.,$$

where \mathbf{y}_u , \mathbf{y}_d and \mathbf{y}_e denote the Yukawa couplings of the up-type quarks, down-type quarks and the charged leptons. Note that we choose not to introduce right-handed neutrinos. The Yukawa couplings are 3x3 complex matrices in flavor space. After symmetry breaking we get mass matrices $\frac{\mathbf{y}_u v}{\sqrt{2}}$, $\frac{\mathbf{y}_d v}{\sqrt{2}}$ and $\frac{\mathbf{y}_e v}{\sqrt{2}}$ for the up-type quarks, down-type quarks and charged leptons respectively. Since these matrices are not necessarily diagonal, we can diagonalize them using unitary matrices in $U(3)$, and obtain mass eigenstates. This process leaves its trace in the coupling of the W -boson to fermions:

$$\begin{aligned} & i\bar{\psi}_{L,u}^a \gamma^\mu W_\mu^+ \psi_{L,d}^a \\ \rightarrow & i\bar{\Psi}_{L,u}^a U_{\text{CKM}}^{ab} \gamma^\mu W_\mu^+ \Psi_{L,d}^b, \end{aligned}$$

where Ψ denotes the mass eigenstates and U_{CKM}^{ab} the *Cabibbo-Kobayashi-Maskawa* matrix. Experimentally it has been determined that this matrix is not diagonal, since, for example, a strange quark can decay into an up quark via the W boson. The unitary matrices needed to go from flavor to mass eigenstates disappear in the couplings to the Z boson and the photon, since these gauge bosons couple the upper components of the $SU(2)$ doublets to upper components. If this would not be the case, we would expect to observe flavor changing neutral currents (FCNC), where, for example, a top quark could decay directly to a charm quark. Experimentally FCNCs have been observed, however strongly suppressed, suggesting it is a next-to-leading order process. More on FCNCs can be found in chapter 3.

2.1.1 Renormalization

The *cross section* σ , defined as the probability of a specific process to happen, is proportional to the square of the scattering amplitude. This amplitude can be calculated using *Feynman diagrams* and the corresponding *Feynman rules*. Consider for example electron scattering. One of the diagrams contributing to this process at leading order (LO) is shown in figure 2.1 (left). At next-to-leading order (NLO), loop corrections to the photon propagator can be introduced (figure 2.1, right). These loop corrections can be quite problematic, as these introduce integrals over the momentum of the fermion in the loop (k), which are of the form $\int_0^\infty d^4k \frac{1}{k^2 - m_f^2}$ and thus diverge. We know however that the scattering amplitude is a finite number, as it can be measured in experiment. To solve this we need *renormalization*.

Renormalization consists of two steps. First we need a prescription to describe the infinities: *regularization*. Several regularization methods exist, one of which being the momentum cut-off. In this method, we define a cut-off energy Λ , which will act as an upper limit of the momentum in the integrals. A validation for this procedure on a physical level is that we do not assume that our theory is valid up to all energy scales. The SM does not allow for gravity for example, which sets a natural value for the cut-off

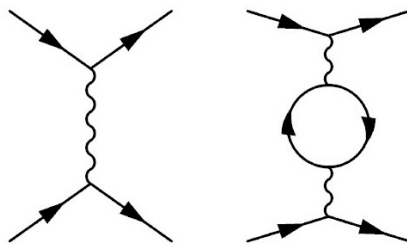


FIGURE 2.1: Electron scattering at leading order (*left*) and next-to-leading order (*right*).

scale to be $M_{\text{Planck}} \simeq 1.2 \cdot 10^{19}$ GeV. Regularization results in an amplitude that depends on Λ and diverges when $\Lambda \rightarrow \infty$.

In the second step of renormalization, we want to get rid of this energy scale. After all, we have chosen Λ arbitrarily so any physical observable quantity should not depend on it. This is done by absorbing Λ in the Lagrangian coupling constants by introducing a renormalization energy scale μ_R . The value of the coupling constant is measured at this scale, allowing us to make predictions for any other energy scale. The divergent part depending on Λ is removed by introducing counter terms. We are allowed to do this as this bare parameter is not an observable quantity, only squared amplitudes are observable. These amplitudes depend on a physical coupling constant, which incorporates all quantum corrections. This will mean that the physical coupling constant has now an ambiguous name, as it is no longer a constant but changes with energy (hence the name *running couplings*).

A theory is called renormalizable if all divergences can be absorbed in such manner into a finite number of parameters. This means that after the determination of a few physical parameters, we can make predictions of all cross sections at all loop orders¹.

2.2 Beyond the Standard Model

The Standard Model is an accurate model, but also incomplete. One of its greatest challenges is how to include the force of gravity. However, this problem arises only at the Planck scale, $M_{\text{P}} \sim 10^{19}$ GeV. This problem is out of reach of the LHC, or any other foreseeable human-based experiment. The question is however, should we also expect Beyond the SM (BSM) physics at scales lower than the Planck scale? There are many reasons to believe so:

- Observations of neutrino oscillations suggest that neutrinos have mass. A right-handed neutrino has never been observed directly through interactions, which does not exclude the possibility that maybe neutrino masses arise in the SM due to some other process than the Higgs mechanism.
- The existence of dark matter (chapter 1).
- Dark energy: a hypothetical form of energy responsible for the expansion of the universe.
- The hierarchy problem (section 2.2.1).
- Matter - antimatter asymmetry in the current universe. The amount of CP violation in the SM is not enough to explain matter being dominant over antimatter.
- Grand unification (section 2.2.2).

¹In principle, but this is not easy to do!

2.2.1 The hierarchy problem: The problem of a fat Higgs boson

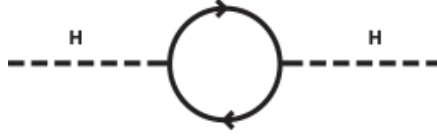


FIGURE 2.2: One-loop contribution to the Higgs self-energy.

In the electroweak sector of the Standard Model, the mass of the Higgs boson is given at tree level by $m_h = v\sqrt{\frac{\lambda}{2}}$, as can be seen in the Lagrangian. One of the one-loop self-energy correction terms, as shown in figure 2.2, is proportional to:

$$\delta m_h^2 \propto y_f^2 \int \frac{d^4k}{(2\pi)^2} \left(\frac{1}{k^2 - m_f^2} + \frac{2m_f^2}{(k^2 - m_f^2)^2} \right),$$

where y_f is the Yukawa coupling. The largest correction to the Higgs mass comes from the fermion with the largest Yukawa coupling to the Higgs boson, which is the top quark for the SM ($m_t \sim 173$ GeV). The first term of this integral is quadratically divergent. Using a cut-off to indicate the energy scale where new physics arises (Λ), one finds that $\delta m_H^2 \propto \Lambda^2$. This results in the following Higgs mass (assuming that the Higgs boson couples to particles which reside at the energy scale Λ):

$$m_h^2(\text{physical}) \sim m_h^2 + \mathcal{O}(y_f^2 \Lambda^2) + \mathcal{O}(\log \Lambda).$$

The SM is renormalizable, which means that such divergences can be solved by introducing counter terms to the Lagrangian. However, these counter terms should remove corrections to the bare Higgs mass squared up to 34 orders of magnitude, as we measure a Higgs mass squared of $m_h^2(\text{physical}) \sim (125\text{GeV})^2$ in experiment. Although this procedure is theoretically allowed, it is not a pleasing theory due to the enormous level of fine tuning that is required².

There is however a more elegant solution to the hierarchy problem. If we could introduce extra scalar particles with the same quantum numbers and masses as the fermions, their contribution to the Higgs mass would be equal to the fermionic loops from the SM, except for the minus sign that the fermionic loops introduce. We would therefore be able to cancel the divergent terms completely.

2.2.2 Unification of gauge couplings

This issue is not so much a problem of the SM, but can be seen as a quest for a more fundamental theory. We saw that two fundamental forces, the electromagnetic and the weak force, can be combined into the electroweak force. This gives rise to the question: could all forces be unified? Using the evolution of gauge couplings, we see that at an energy of $\Lambda_{\text{GUT}} \sim 10^{15}$ GeV the strengths of the three forces become almost identical (see figure 2.3), but not exactly. Additional particles can influence the running of the

²Although it is debatable whether every theory needs to be elegant...

couplings, creating an opportunity for gauge coupling unification. This is illustrated on the right-hand side of figure 2.3.

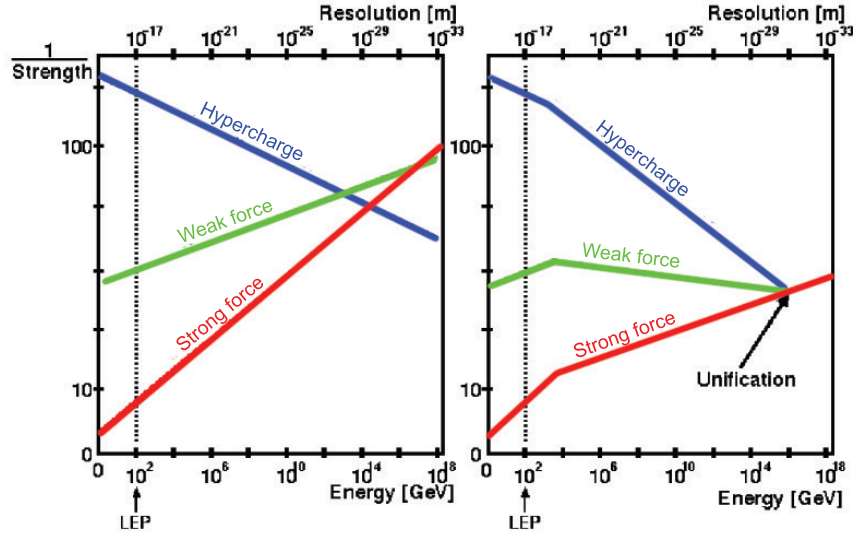


FIGURE 2.3: Evolution of the inverse coupling constants as a function of the energy for the SM (*left*) and a grand unification theory (*right*). Extracted from ref. [17].

2.3 SUSY to the rescue!

Particles and interactions in the SM are understood by imposing symmetry constraints on the Lagrangian. This raises a question: can't we impose further symmetries, like a space-time symmetry between bosons and fermions? This is done by invoking supersymmetry (SUSY). The SUSY transformation is described by (two-dimensional) spinor operators Q_a that modify the spin of some state by 1/2:

$$\begin{aligned} Q |\text{Boson}\rangle &= |\text{Fermion}\rangle, \\ Q |\text{Fermion}\rangle &= |\text{Boson}\rangle. \end{aligned}$$

These operators generate a new Lie algebra and satisfy the following anti-commutation relations:

$$\begin{aligned} \{Q_a, Q_b\} &= \{Q_a^\dagger, Q_b^\dagger\} = 0 \\ \{Q_a, Q_b^\dagger\} &= 2(\sigma^\mu)_{ab} P_\mu \end{aligned}$$

where σ^μ are the Pauli Spin matrices and P_μ the momentum generator of translations. This implies the supersymmetric algebra:

- The action of Q on a state will modify its spin by 1/2.
- The operator P^μ commutes with Q and Q^\dagger , which leads to eigenstates that are in a *supermultiplet* consisting of bosonic or fermionic states and their superpartners with opposite spin.

- Superpartners in a supermultiplet must have equal mass and quantum numbers.
- The number of bosonic and fermionic degrees of freedom must be equal to each other, as two subsequently applied SUSY transformations maps the bosonic subspace onto itself.

In supersymmetry it is convenient to split the Dirac spinor into two Weyl spinors χ_L (left-handed) and χ_R (right-handed):

$$\psi = \begin{pmatrix} \chi_L \\ \chi_R \end{pmatrix}.$$

The right-handed Weyl spinors are often brought into a left-handed form via:

$$\psi_R^c = i\sigma^2 \psi_R^*. \quad (2.4)$$

These spinors describe fermionic particles, so they must be anti-commuting. The indices are raised and lowered by the symbol $\epsilon_{\alpha\beta}$, with non-zero components $\epsilon_{12} = -\epsilon_{21} = -1$. This symbol will be used to make a singlet out of two Weyl spinors.

The simplest possibility for a supermultiplet is to group a left-handed Weyl fermion (with two physical degrees of freedom, $n_f = 2$) and a complex scalar (with $n_b = 2$). The names of these scalar superpartners are constructed by preceding an ‘s’ (so we get *sfermions*). This combination is called a *chiral* or *scalar* supermultiplet.

Another possibility is to combine a gauge boson (massless spin 1 boson with 2 degrees of freedom) with a (Majorana) Weyl fermion. These fermions are called *gauginos*, and as superpartners of the gauge bosons they must transform as the adjoint representation of the gauge group. This is its own conjugate, so the gauginos must have the same gauge-transformation properties for left-handed and right-handed components, hence we use a Majorana Weyl fermion. The supermultiplet is called a *gauge* or *vector* supermultiplet.

The *Minimal Supersymmetric Standard Model* (MSSM) represents the simplest possible supersymmetric extension to the SM. The particle content of the MSSM is summarized in table 2.2. There are two Higgs chiral supermultiplets (containing a complex scalar Higgs boson and two Higgsinos). This is because of the structure of supersymmetric theories: only a $Y = 1/2$ Higgs supermultiplet can have a Yukawa coupling to up-type quarks, and only a $Y = -1/2$ supermultiplet can couple to down-type quarks and charged leptons. We will refer to these supermultiplets by H_u for $Y = 1/2$ and H_d for $Y = -1/2$. The weak isospin components of H_u with $T_3 = (1/2, -1/2)$ have electromagnetic charges 1 and 0 and are denoted by H_u^+ and H_u^0 . In contrast, H_d has $T_3 = (1/2, -1/2)$ components denoted as H_d^0 and H_d^- . In total there are 8 real d.o.f. in these Higgs doublets. After electroweak symmetry breaking, 5 d.o.f. are left: two neutral scalars h^0 and H^0 , two charged scalars h^+ and h^- and one neutral pseudoscalar A^0 . The lightest neutral scalar h^0 can act like the SM Higgs boson.

The masses of these Higgs bosons can be determined from the Higgs scalar potential V , which should have a local minimum and v.e.v. unequal to 0. Furthermore, this minimum must break electroweak symmetry down to electromagnetism: $SU(2)_L \otimes U(1)_Y \rightarrow U(1)_{EM}$. Due to gauge freedom, we can pick $H_u^+ = H_d^- = 0$ at the minimum of the potential and set the vacuum expectation value of H_u^0 to $v_u/\sqrt{2}$ and H_d^0 to $v_d/\sqrt{2}$. The ratio between the two v.e.v.’s is denoted by $\tan\beta = \frac{v_u}{v_d}$. These values are related to the

v.e.v. of the SM Higgs boson via $v^2 = v_u^2 + v_d^2 = \frac{4M_Z^2}{g^2 + g'^2}$.

A compact version of the MSSM Lagrangian is given by:

$$\begin{aligned}
\mathcal{L}_{SUSY} = & \underbrace{(D_\mu \phi_f)^\dagger (D^\mu \phi_f)}_{\text{scalars}} + \underbrace{i(\psi_f)^\dagger \bar{\sigma}^\mu D_\mu \psi_f}_{\text{fermions}} - \underbrace{\frac{1}{4} F_{v,\mu\nu}^a F_v^{a,\mu\nu}}_{\text{gauge bosons}} + \\
& \underbrace{i(\lambda_v^a)^\dagger \bar{\sigma}^\mu D_\mu \lambda_v^a}_{\text{gauginos}} - \underbrace{\left| \frac{\partial W}{\partial \phi_f} \right|^2}_{\text{scalar potential}} - \\
& \underbrace{\frac{1}{2} \left[\frac{\partial^2 W}{\partial \phi_f \partial \phi_g} \psi_f \cdot \psi_g + h.c. \right]}_{\text{fermion mass term and Yukawa coupling}} - \\
& \underbrace{\sqrt{2} g_v \left[(\phi_f^\dagger T_v^a \psi_f) \cdot \lambda_v^a + \lambda_v^{\dagger a} \cdot (\psi_f^\dagger T_v^a \phi_f) \right]}_{\text{additional couplings}} - \frac{1}{2} g_v^2 (\phi_f^\dagger T_v^a \phi_f)^2,
\end{aligned}$$

where ϕ_f , ψ_f denote scalar and fermionic fields respectively with f and g running over all gauge and flavor d.o.f. and λ_a denotes a gaugino with the index a running over the adjoint representation of the gauge group ($a = 1 \dots 8$ for SU(3), $a = 1, 2, 3$ for SU(2) and $a = 1$ for U(1)). The index v is used to run over the three gauge groups. The dot indicates the spinor product, defined as $\psi \cdot \psi \equiv \psi^\alpha \epsilon_{\alpha\beta} \psi^\beta$.

All interactions and masses (before symmetry breaking) of all particles are determined by their gauge transformation properties and the *superpotential* W , occurring in the second and third line of the MSSM Lagrangian. This superpotential is a function of chiral superfields. The form of the superpotential is restricted by the requirement of

		spin 0	spin 1/2
Squarks, quarks (3 generations)	Q	$(\tilde{u}, \tilde{d})_L$	$(u, d)_L$
	\bar{u}	\tilde{u}_R^*	u_R^c
	\bar{d}	\tilde{d}_R^*	d_R^c
Sleptons, leptons (3 generations)	L	$(\tilde{\nu}_e, \tilde{e})_L$	$(\nu_e, e)_L$
	\bar{e}	\tilde{e}_R^*	e_R^c
Higgs, higgsinos	H^u	(H_u^+, H_u^0)	$(\tilde{H}_u^+, \tilde{H}_u^0)$
	H^d	(H_d^0, H_d^-)	$(\tilde{H}_d^0, \tilde{H}_d^-)$
		spin 1/2	spin 1
Gluinos, gluons		\tilde{g}^a	g^a
Winos, W bosons		$\tilde{W}^{1,2,3}$	$W^{1,2,3}$
Bino, B boson		\tilde{B}^0	B^0

TABLE 2.2: Particle content of the MSSM. Whenever we want to denote only the SUSY content of the superfields, we will indicate this by a tilde.

gauge invariance. For the MSSM it has the following form:

$$W_{\text{MSSM}} = \bar{u}\mathbf{y}_u Q \cdot H_u - \bar{d}\mathbf{y}_d Q \cdot H_d - \bar{e}\mathbf{y}_e L \cdot H_d + \mu H_u \cdot H_d. \quad (2.5)$$

The Yukawa coupling parameters \mathbf{y}_u , \mathbf{y}_d and \mathbf{y}_e are 3x3 matrices and μ is the supersymmetric version of the Higgs boson mass. There are also other terms that we in principle can add to the superpotential without breaking gauge symmetry:

$$L \cdot L\bar{e}; \quad Q \cdot L\bar{d}; \quad L \cdot H_u; \quad \bar{u}\bar{d}\bar{d}.$$

These terms violate baryon and lepton number, leading to unwanted proton decay. To prevent this process from happening, a new symmetry called *R-parity* is postulated. This is a new quantum number defined as:

$$P_R = (-1)^R \equiv (-1)^{3(B-L)+2S},$$

where S denotes the spin, B denotes baryon number and L lepton number. Since $(-1)^{2S}$ is conserved, *R-parity* is conserved if B-L is conserved. All SM particles, including the Higgs bosons, have *R-parity* +1 and all SUSY particles have *R-parity* -1. Conservation of *R-parity* also leads to a stable lightest supersymmetric particle (LSP), which is, if it is also neutral and weakly interacting, a perfect WIMP candidate. Other consequences are:

- Each SUSY particle must eventually decay into an odd number of LSPs.
- In collider experiments SUSY particles can only be produced in pairs.

2.3.1 Soft SUSY breaking terms

Clearly, because none of the superpartners have been observed, supersymmetry needs to be a broken symmetry. The exact breaking mechanism is unknown. There are two possible ways to break a symmetry in field theory: explicit (introduce symmetry breaking terms by hand into the Lagrangian) or spontaneous (like the SM Higgs mechanism) symmetry breaking. In the MSSM, SUSY-breaking is explicitly introduced. This results in a soft-breaking term in the Lagrangian:

$$\begin{aligned} \mathcal{L}_{\text{soft}}^{\text{MSSM}} = & - \frac{1}{2} \left(M_3(\tilde{g}^a)^T \tilde{g}^a + M_2(\tilde{W}^j)^T \tilde{W}^j + M_1\tilde{B}^T \tilde{B} + c.c. \right) \\ & - \left(\tilde{u}\mathbf{a}_u \tilde{Q} H_u - \tilde{d}\mathbf{a}_d \tilde{Q} H_d - \tilde{e}\mathbf{a}_e \tilde{L} H_d + c.c. \right) \\ & - \tilde{Q}^\dagger \mathbf{m}_Q^2 \tilde{Q} - \tilde{L}^\dagger \mathbf{m}_L^2 \tilde{L} - \tilde{u}\mathbf{m}_u^2 \tilde{u}^\dagger - \tilde{d}\mathbf{m}_d^2 \tilde{d}^\dagger - \tilde{e}\mathbf{m}_e^2 \tilde{e}^\dagger \\ & - m_{H_u}^2 H_u^* H_u - m_{H_d}^2 H_d^* H_d - (bH_u \cdot H_d + c.c.). \end{aligned}$$

The first line represents the mass terms of the gauginos where M_3 , M_2 and M_1 are the gluino, wino and bino mass terms. With the tilde we indicate the only content of the chiral supermultiplets that are indicated by a tilde (as given in table 2.2). The bar does not denote any kind of conjugation, but is part of the particle name. All of the \mathbf{a}_i -terms are complex 3x3 matrices with the dimension of mass. In the third line we include mass

terms for squarks and sleptons with hermitian 3x3 matrices. In the last line, the soft breaking contribution from the Higgs mass terms are given.

The soft SUSY breaking Lagrangian introduces a lot of new free parameters, which we only can determine by observing them directly or indirectly. A careful count of free parameters results in:

- Five 3x3 hermitian sfermion mass matrices: 45
- Two masses for the Higgses: 2
- Majorana mass terms for the gauginos: 3
- 3 unrestricted 3x3 matrices \mathbf{a}_i : 54
- Mixing Higgs mass term: 1

Total: 105 free parameters [18]

Note that not SUSY itself, but the unknown nature of the SUSY breaking mechanism introduces a tremendous amount of arbitrariness in the Lagrangian. Due to broken supersymmetry, the hierarchy problem is no longer solved exactly. However, when the masses of the particles are not too different from SM particle masses, there exists an approximate cancellation, thus we need considerably less fine-tuning.

2.3.2 Neutralinos and charginos

Due to the effects of electroweak symmetry breaking, the higgsinos and electroweak gauginos mix with each other. We combine the neutral higgsinos ($\tilde{H}_u^0, \tilde{H}_d^0$) and gauginos (\tilde{B}, \tilde{W}^0) into four mass eigenstates called *neutralinos*, labeled with $\tilde{\chi}_i^0$. The charged gauge-eigenstates $\tilde{H}_u^+, \tilde{H}_d^-$ and \tilde{W}^\pm are combined into two mass eigenstates called *charginos* (with charge ± 1), labeled with $\tilde{\chi}_i^\pm$. These mass eigenstates are labeled according to their mass, with $i = 1$ being the lightest. In many models, $\tilde{\chi}_1^0$ is also the lightest supersymmetric particle (LSP). This means that we have a electromagnetically neutral, weakly interacting and, if R -parity is conserved, stable particle, making it a perfect WIMP dark matter candidate.

In gauge-eigenstate basis $\psi^0 = (\tilde{B}, \tilde{W}^0, \tilde{H}_d^0, \tilde{H}_u^0)$, the mass part of the Lagrangian is given by:

$$\mathcal{L}_{\text{neutralino mass}} = -\frac{1}{2} (\psi^0)^T \mathbf{M}_{\tilde{\chi}^0} \psi^0 + c.c., \quad (2.6)$$

where

$$\mathbf{M}_{\tilde{\chi}^0} = \begin{pmatrix} M_1 & 0 & -c_\beta s_{\theta_W} M_Z & s_\beta s_{\theta_W} M_Z \\ 0 & M_2 & c_\beta c_{\theta_W} M_Z & -s_\beta c_{\theta_W} M_Z \\ -c_\beta s_{\theta_W} M_Z & c_\beta c_{\theta_W} M_Z & 0 & -\mu \\ s_\beta s_{\theta_W} M_Z & -s_\beta c_{\theta_W} M_Z & -\mu & 0 \end{pmatrix}.$$

Here, M_1 and M_2 denote the gaugino masses, M_Z the Z boson mass, and $-\mu$ is the supersymmetric version of the Higgs mass as introduced in equation 2.5. We use $\tan\beta$ to denote the ratio of the two Higgs vacuum expectation values. The weak mixing angle is indicated by θ_W , with $\tan\theta_W = \frac{g'}{g}$ and $M_W = M_Z \cos\theta_W$. We introduced the abbreviations $s_\beta = \sin\beta$, $c_\beta = \cos\beta$, $s_{\theta_W} = \sin\theta_W$ and $c_{\theta_W} = \cos\theta_W$. The neutralino mass matrix $\mathbf{M}_{\tilde{\chi}^0}$ can be diagonalized to find the mass eigenstates $\tilde{\chi}_i^0$. The same can be done for the chargino mass spectrum. In gauge-eigenstate basis $\psi^\pm = (\tilde{W}^+, \tilde{H}_u^+, \tilde{W}^-, \tilde{H}_d^-)$ the mass part of the Lagrangian is given by:

$$\mathcal{L}_{\text{chargino mass}} = -\frac{1}{2} (\psi^\pm)^T \mathbf{M}_{\tilde{\chi}^\pm} \psi^\pm + c.c., \quad (2.7)$$

where

$$\mathbf{M}_{\tilde{\chi}^\pm} = \begin{pmatrix} 0 & 0 & M_2 & \sqrt{2}c_\beta M_W \\ 0 & 0 & \sqrt{2}s_\beta M_W & \mu \\ M_2 & \sqrt{2}s_\beta M_W & 0 & 0 \\ \sqrt{2}c_\beta M_W & \mu & 0 & 0 \end{pmatrix}$$

The eigenvalues are double degenerate, so diagonalization results in two same valued mass eigenstates $\tilde{\chi}_i^\pm$.

Each neutralino and chargino contains at least a small component of the electroweak gauginos. Depending on the exact values of the unknown parameters β , M_1 , M_2 and μ , neutralinos have a dominant bino, wino or higgsino component. We will refer to such eigenstates as bino-like, wino-like or higgsino-like respectively. In table 2.3 we show for each scenario the dominant component of the neutralinos and charginos.

Scenario	Composition neutralinos	Composition charginos
$M_1 < M_2 < \mu $	$(\tilde{B}, \tilde{W}, \tilde{H}, \tilde{H})$	(\tilde{W}, \tilde{H})
$M_1 < \mu < M_2$	$(\tilde{B}, \tilde{H}, \tilde{H}, \tilde{W})$	(\tilde{H}, \tilde{W})
$ \mu < M_1 < M_2$	$(\tilde{H}, \tilde{H}, \tilde{B}, \tilde{W})$	(\tilde{H}, \tilde{W})
$ \mu < M_2 < M_1$	$(\tilde{H}, \tilde{H}, \tilde{W}, \tilde{B})$	(\tilde{H}, \tilde{W})
$M_2 < \mu < M_1$	$(\tilde{W}, \tilde{H}, \tilde{H}, \tilde{B})$	(\tilde{W}, \tilde{H})
$M_2 < M_1 < \mu $	$(\tilde{W}, \tilde{B}, \tilde{H}, \tilde{H})$	(\tilde{W}, \tilde{H})

TABLE 2.3: Dominant component of the neutralinos (denoted as $(\tilde{\chi}_1^0, \tilde{\chi}_2^0, \tilde{\chi}_3^0, \tilde{\chi}_4^0)$) and charginos ($(\tilde{\chi}_1^\pm, \tilde{\chi}_2^\pm)$), extracted from ref. [19].

Chapter 3

Experimental constraints

One of the main motivations for supersymmetry is the prediction of a stable (in the case of R-parity conserving supersymmetry) particle, which may be identified as a candidate dark matter particle if it is both colorless and electromagnetically neutral. Often, this role is taken by the lightest neutralino, $\tilde{\chi}_1^0$, and we will assume this as well. If we choose this framework to search for a dark matter particle, it is unwise to completely separate the DM searches from searches for SUSY. However, even in the MSSM this search can be quite complicated, as we have to deal with a large number (typically ~ 100) of free parameters. To this end, one sets up simplified models. Such an approach is valuable, but too constraining scenarios (like mSUGRA [20]) are phenomenologically limiting and some models are even excluded by experimental data.

In this discussion we will use the 19-parameter phenomenological MSSM (pMSSM [21]). In this scheme one assumes that:

- The soft SUSY-breaking parameters $\mathbf{m}_{\tilde{Q},\tilde{L},\tilde{u},\tilde{d},\tilde{e}}^2$ and $\mathbf{a}_{u,d,e}$ are real, which assures that the only source for CP violation is the CKM matrix in the Standard Model.
- To further limit the CP violating effects and the possibility of large meson mixing contributions (e.g. for D^0, \bar{D}^0), the masses of the first and second generation sfermions are equal, separately in the lepton and quark sectors, e.g. $m_{\tilde{Q}_1} = m_{\tilde{Q}_2}$, where the subscript denotes the generation.
- To minimize the effects of mixing in the sfermion sector (such as FCNCs), we assume that all sfermion mass matrices are diagonal.
- All first and second generation trilinear couplings (A_f) will be put to 0, as the \mathbf{a}_f -matrices are assumed to scale with the Yukawa couplings ($\mathbf{a}_f = A_f \mathbf{y}_f$). Hence only A_t, A_b and A_τ have a non-zero value.

In particular we will assume nothing about the nature of SUSY symmetry breaking. The remaining parameters are 10 sfermion masses ($m_{\tilde{Q}_1}, m_{\tilde{Q}_3}, m_{\tilde{L}_1}, m_{\tilde{L}_3}, m_{\tilde{u}_1}, m_{\tilde{u}_3}, m_{\tilde{d}_1}, m_{\tilde{d}_3}, m_{\tilde{e}_1}$ and $m_{\tilde{e}_3}$), 3 gaugino masses ($M_{1,2,3}$), the ratio of the Higgs vacuum expectation values $\tan \beta$, the Higgsino mixing parameter μ , the mass m_A of the CP-odd Higgs boson A^0 and 3 trilinear scalar couplings ($A_{b,t,\tau}$). In the notation for the sfermion masses, we use the subscript 1 and 3 to indicate the generation, e.g. $m_{\tilde{u}_3} \equiv m_{\tilde{t}_R}$ indicates the mass of the superpartner of the right-handed top quark. Any scalars with the same electric

charge, R -parity and color quantum numbers can in principle mix with each other. For the first and second generation, these effects are ignored since the trilinear couplings have been put to 0 and the Yukawa induced mixing is quite small. However, the third generation squarks and sleptons can mix. This happens for the pairs $(\tilde{t}_L, \tilde{t}_R)$, $(\tilde{b}_L, \tilde{b}_R)$ and $(\tilde{\tau}_L, \tilde{\tau}_R)$, resulting in mass eigenstates denoted by $(\tilde{t}_1, \tilde{t}_2)$, $(\tilde{b}_1, \tilde{b}_2)$ and $(\tilde{\tau}_1, \tilde{\tau}_2)$ respectively. The subscripts 1 and 2 denote the mass hierarchy: $m_{\tilde{t}_1} < m_{\tilde{t}_2}$.

Within the 19 parameters of the pMSSM, there still is a lot of freedom. We can further constrain our parameter space by demanding that the resulting pMSSM model satisfies experimental constraints. We will separate these constraints in three categories: direct DM searches, indirect DM searches and particle accelerator constraints (figure 3.1). Each of these three categories will be discussed below.

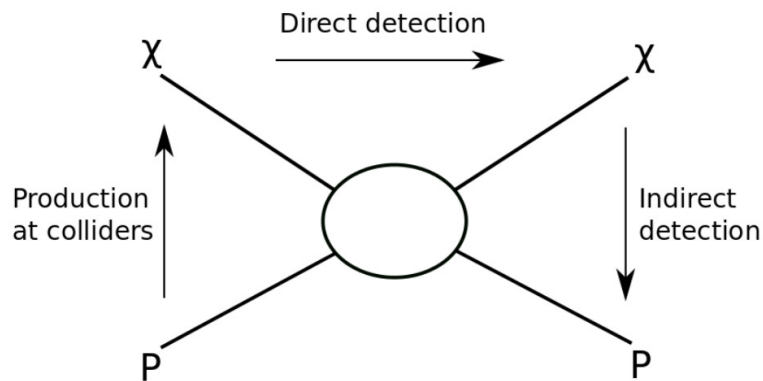


FIGURE 3.1: Graphical representation of the possible dark matter detection channels. P is a SM particle, χ is a DM particle.

3.1 Direct detection

The basic idea is very simple: set up a large and sensitive device, which can detect small perturbations of the atoms within it. WIMPs can interact with nuclei of baryonic matter and deposit some energy via the weak force. How often would this happen in an earth-based experiment? To answer this question, experiments like the *Large Underground Xenon* experiment (LUX) and the *Xenon dark matter project* experiment (XENON) were set up [22–24].

Due to the low velocity of DM, most WIMPs scatter elastically from a baryonic nucleus. In this scattering, the nucleus recoils and causes ionization (an electron escapes from the atom) or scintillation (an electron is excited, which after a short period of time falls back to the ground state and emits a photon) in the detection material. The rate of nuclear recoils can be converted into a cross section for WIMP-nucleon interactions. This interaction can happen spin-independently (SI) or spin-dependently (SD). SD interactions occur through an axial vector coupling to the spin content of the nucleus and are usually divided into proton and neutron couplings. Typically, these limits are weaker than the SI ones. It is important to have many experiments with different targets to study the interaction type of possible signals.

Detectors should be able to distinguish signal from background very efficiently. To reduce background as much as possible, direct detection experiments are often placed in deep underground laboratories. This is to reduce the amount of cosmic ray particles and particles originating from radioactive materials as much as possible. The detector

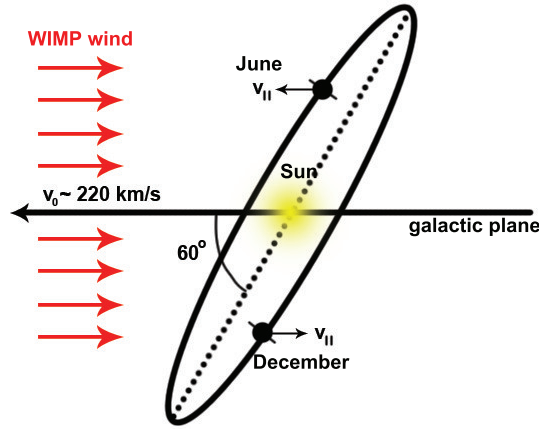


FIGURE 3.2: Illustration of the annual modulation in a WIMP signal.

response can differ for WIMP interaction or background processes, as the majority of the backgrounds interacts electromagnetically with the detection material. A recoiling nucleus travels a smaller distance than a recoiling electron for the same recoil energy, so an interacting WIMP results in a higher energy density. A second method to distinguish signal from background is to exploit the fact that WIMP interaction rates should vary at different times of the year. This is due to the movement of the Earth around the Sun (illustrated in figure 3.2), which has an effect on the WIMP velocity that we observe. This effect should create an annual modulation in the WIMP detection rates.

When the expected rate (depending on a certain WIMP model) and the expected background are calculated, data can be compared to the expected WIMP signal. Many experiments searching for nuclear recoils with WIMPs have been conducted in the past several years. So far no signal has been found. Negative results are however not a waste of time, as they put constraints on the parameter space for a given WIMP theory. In figure 3.3, different detectors and their imposed constraints are shown. The closed contours in this figure are regions where an indication for DM signal has been claimed, for example by DAMA [25]. These regions are in conflict with the results of other searches, so it is not probable that these detections actually originated from WIMPs [23, 26]. In our analysis we will use the LUX limits on the spin-independent WIMP-nucleon scattering cross section.

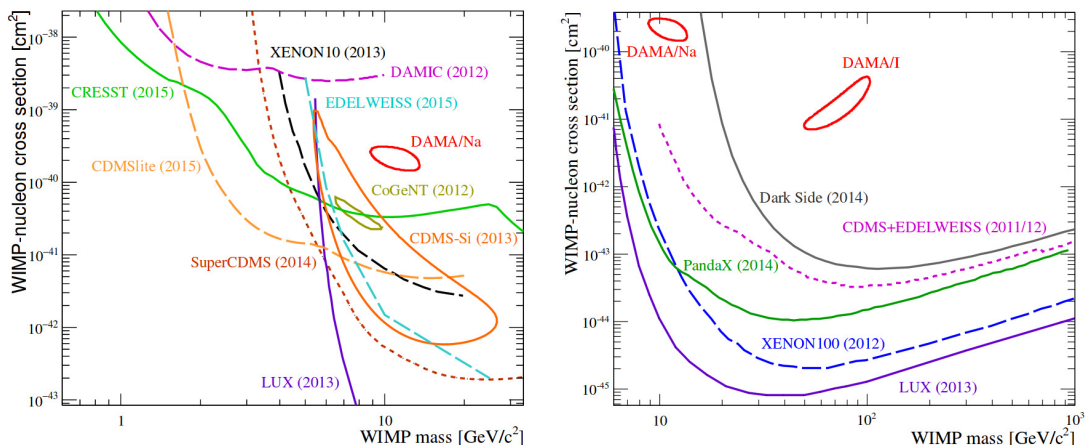


FIGURE 3.3: Result on the spin-independent WIMP-nucleon scattering cross section as a function of WIMP mass (left for masses between 0.5 GeV and 12 GeV, right for masses between 5 GeV and 1 TeV), extracted from ref. [26]. Currently LUX provides the most stringent limit.

3.2 Indirect detection

If we assume that WIMPs are their own anti-particle, they can annihilate with each other. This means that a potential signal could originate from this annihilation. Annihilation products include anti-matter, photons and neutrinos. Two of these annihilation products, photons and neutrinos, are described below. Viable places to look for these products are the Galactic Center, the Milky Way halo, dark matter substructures, satellite galaxies, the Earth and the Sun.

Dwarf galaxies: [27–29] DM annihilation is most common where DM is dense. These regions can be found where there is a lot of baryonic matter, for example at the center of our galaxy, but also in its orbiting satellites: dwarf spheroidal galaxies (dSphs). Observations of the movement of dwarf galaxy’s member stars indicate that these objects contain a vast amount of dark matter. The Fermi Large Area Telescope (LAT [30]) is designed to observe γ -rays (photons with an energy above 100 keV) originating from DM annihilation. This telescope is aboard the Fermi satellite and sensitive to photon energies ranging from 20 MeV to over 300 GeV.

Using relativistic kinematics, one can find that *direct* photon production ($\chi\chi \rightarrow \gamma X$ where X is any of the particles γ , Z or h) leads to monochromatic photons. The two DM particles are assumed to have four-momentum $p_{\chi_1}^\mu = (E_\chi, \vec{p})$ and $p_{\chi_2}^\mu = (E_\chi, -\vec{p})$ and mass m_χ (in the center of mass frame). Momentum conservation leads to:

$$p_{\chi_1}^\mu + p_{\chi_2}^\mu - p_\gamma^\mu = p_X^\mu.$$

Squaring this equation gives:

$$4E_\chi^2 - 4E_\chi E_\gamma = m_X^2.$$

Now assume that $E_\chi \sim m_\chi$:

$$\begin{aligned} 4m_\chi^2 - 4m_\chi E_\gamma &= m_X^2 \\ \rightarrow E_\gamma &= m_\chi \left(1 - \frac{m_X^2}{4m_\chi^2} \right). \end{aligned}$$

Ignoring the effect of potential boosts, this would lead to a peak in the photon spectrum. These photon peaks are however hard to observe. The indicated processes are suppressed, because the dark matter particle is a neutral particle. Another complication is the limited angular resolution of detectors.

Secondary photon production can take place through a DM annihilation into pairs of quarks and heavy gauge bosons (which can decay into quarks). These quarks group to form neutral pions and other hadrons. These pions decay primarily into photon pairs. This *hadronization* process has been studied at accelerators¹. The spectrum of photons produced per DM annihilation depends on the mass of the WIMP particle and the types of particles produced. In figure 3.4 the spectrum of photons produced per DM annihilation for a 30 GeV DM particle and for a variety of annihilation channels is shown. Obviously, the shape, width and the peak energy differs for different annihilation channels, although photons often show a soft cut-off at the kinematical limit $E_\gamma \simeq m_{\text{DM}}$. The lightest neutralino is a WIMP candidate, but there are many other possible forms of

¹More on hadronization can be found in chapter 5

WIMP dark matter. To avoid all the cumbersome details of SUSY, model-independent studies of dark matter phenomenology with different combinations of spins and types of interactions with SM particles have been conducted. These interactions are only limited by the requirement of Lorentz invariance. Furthermore, the WIMP abundance must match cosmological observations. These interactions are not required to be invariant under the SM gauge symmetry. For example, if we consider the interaction between two fermionic WIMPs (χ) and two SM fermions (f), the interaction Lagrangians could look like:

$$\begin{aligned} \text{Scalar(S)} : \mathcal{L} &= \frac{G_S}{\sqrt{2}} \bar{\chi} \chi \bar{f} f \\ \text{Pseudoscalar(P)} : \mathcal{L} &= \frac{G_P}{\sqrt{2}} \bar{\chi} \gamma^5 \chi \bar{f} \gamma_5 f \\ \text{Vector(V)} : \mathcal{L} &= \frac{G_V}{\sqrt{2}} \bar{\chi} \gamma^\mu \chi \bar{f} \gamma_\mu f \\ \text{Axialvector(A)} : \mathcal{L} &= \frac{G_A}{\sqrt{2}} \bar{\chi} \gamma^\mu \gamma^5 \chi \bar{f} \gamma_\mu \gamma_5 f. \end{aligned}$$

With these effective Lagrangians, it is possible to derive the velocity-weighted annihilation cross section and resulting photon spectrum. The photon spectrum depends on the WIMP mass, interaction Lagrangian, the dark matter density distribution and the hadronization and decay channel.

In addition to these highly energetic γ -rays, DM annihilation into e^+e^- can also generate photons via inverse Compton ($e\gamma \rightarrow e\gamma$, where the electron loses energy and the photons gain energy) and bremsstrahlung processes. These photons usually have an energy in the radio regime.

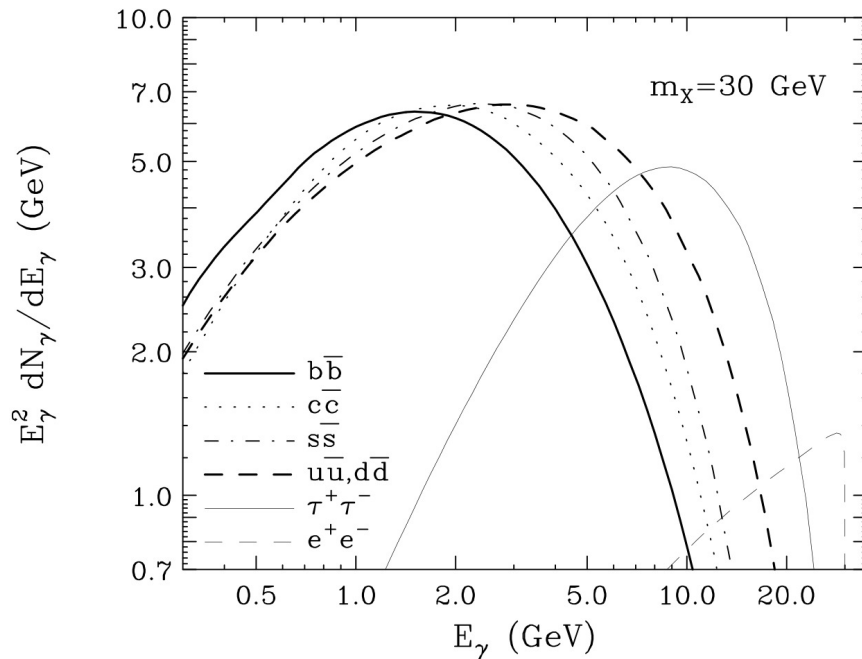


FIGURE 3.4: The spectrum of photons produced per DM annihilation with a mass of 30 GeV. A higher DM mass shifts all the spectra to the right. Extracted from ref. [28].

We can derive the photon flux we would expect from an annihilating WIMP pair in the DM halo of a massive object (like the Milky Way or a dwarf galaxy). The WIMP annihilation rate Γ_{ann} (per second and per unit volume) at a distance r from the center of the DM halo is proportional to the WIMP self-annihilation cross section $\langle\sigma v\rangle$ and the WIMP number density $n_{\text{DM}}(r)$ squared:

$$\Gamma_{\text{ann}} \propto \frac{1}{2} \langle\sigma v\rangle n_{\text{DM}}^2(r) = \langle\sigma v\rangle \frac{\rho_{\text{DM}}^2(r)}{2m_{\text{DM}}^2},$$

where $\rho_{\text{DM}}(r)$ is the WIMP density at a distance r from the center of the dark matter halo and m_{DM} the WIMP mass. A factor of $\frac{1}{2}$ is included to avoid double counting. The quantity r is related to the distance l from the telescope to the annihilating WIMP pair via $r = \sqrt{D^2 + l^2 - 2Dl \cos \theta}$, where D is the distance from the telescope to the center of the dark matter halo and θ is the opening angle of the detection instrument (figure 3.5).

The intensity of WIMP annihilation (flux per solid angle, indicated by $\frac{d\Phi}{d\Omega}$) observed at the telescope with an opening angle θ with respect to the center of the DM halo direction is proportional to the line of sight (l) integration of the DM annihilation rate:

$$\frac{d\Phi}{d\Omega} \propto \int_{\text{l.o.s.}} \Gamma_{\text{ann}}(l) dl = \frac{\langle\sigma v\rangle}{2m_{\text{DM}}^2} \int_{\text{l.o.s.}} \rho_{\text{DM}}^2(l) dl.$$

It is useful to define the average value of this intensity in a cone with half-angle θ that spans a field of view of $\Delta\Omega = 2\pi(1 - \cos\theta)$. This factor is commonly referred to as the J -factor:

$$J \equiv \int d\Omega \int_{\text{l.o.s.}} \rho_{\text{DM}}^2(l) dl. \quad (3.1)$$

Let dN_γ/dE_γ be the photon spectrum per DM annihilation product (as shown in figure 3.4). The total differential photon flux originating from annihilating DM in a solid angle $\Delta\Omega$ at a photon energy E_γ is then given by:

$$\frac{d\Phi_\gamma(E_\gamma)}{dE_\gamma} = \frac{\langle\sigma v\rangle}{2} \frac{1}{4\pi m_{\text{DM}}^2} \frac{dN_\gamma}{dE_\gamma} \int d\Omega \int_{\text{l.o.s.}} \rho_{\text{DM}}^2(l) dl, \quad (3.2)$$

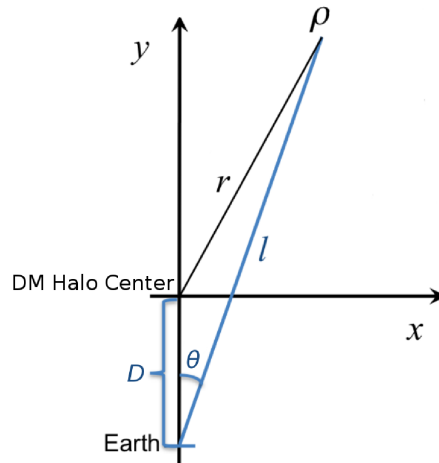


FIGURE 3.5: Illustration of the line of sight l and the azimuth angle θ in the coordinate system related to the DM halo.

where a factor of $\frac{1}{4\pi}$ is included to account for isotropic emission. Different photon production channels could contribute to the photon spectrum per annihilation, so an implicit sum over all photon production channels is assumed. The DM density is determined by density formulas as given in chapter 1. The optimal value for the integration region $\Delta\Omega$ depends on the dark matter density profile of the target and the angular resolution of the detection instrument.

Searches for γ -rays produced via DM annihilation in dwarf galaxies yield constraints on $\langle\sigma v\rangle$, given the dark matter density profile and annihilation process. For any dwarf galaxy for that no γ -ray signal is found (after subtraction of background processes), we can derive an upper limit for the velocity-weighted annihilation cross section. Fermi-LAT derived an upper limit on $\langle\sigma v\rangle$ at 95% confidence level for $m_{DM} = 2$ GeV - 10 TeV annihilating into six different channels ($b\bar{b}$, $\tau\bar{\tau}$, $\mu\bar{\mu}$, $e\bar{e}$, W^+W^- and $u\bar{u}$). Figure 3.6 shows a comparison for the limits for $b\bar{b}$ and $\tau\bar{\tau}$ annihilation channels.

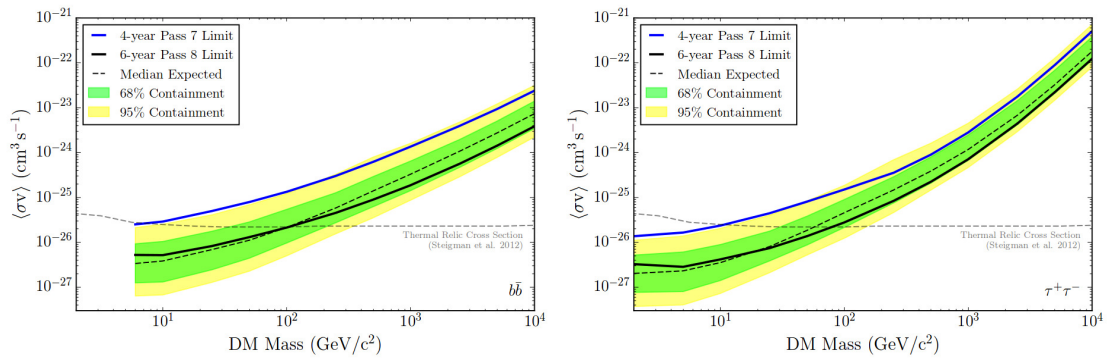


FIGURE 3.6: Limits for the DM velocity-weighted annihilation cross section for $b\bar{b}$ (left) and $\tau^+\tau^-$ (right) channels from Pass 8 data (solid black line). The NFW density profile is used to create these limits. Extracted from ref. [31]

IceCube [32]: The IceCube detector tries to detect neutrinos originating from DM annihilation. The IceCube detector is situated in an ice sheet at the South Pole. It measures Cherenkov light that is emitted by relativistic charged particles, which are created by neutrino interactions in the detector. The background for this search consists mostly of neutrinos created in cosmic ray interactions in the Earth's atmosphere. The detector is sensitive to neutrinos from WIMPs with $m_{DM} \gtrsim 20$ GeV. IceCube estimates how many signal events could be measured, which can be translated into a limit on the signal flux and annihilation rate of dark matter in the Sun. These limits depend on the assumed DM density profile and annihilation channel. Assuming a NFW density profile with a local density of $0.3 \text{ GeV}/\text{cm}^3$ and a DM velocity of 270 km/s, these limits can be converted into limits on the WIMP-proton scattering cross sections for spin-dependent (σ_{SD}) and spin-independent (σ_{SI}) interactions. The limits on these cross sections will be used in our parameter scans.

3.2.1 Dark Matter relic density

From the WMAP and Planck data, we know what the dark matter relic density should be. If we assume the LSP is the only DM particle, this data places severe constraints on the range of pMSSM models we can pick, as can be seen in figure 3.7.

The LSP relic density is higher when DM annihilates less efficiently, which is the case for a bino-dominant LSP. If the LSP annihilates very efficiently, its relic density will turn out to be smaller, which is the case for wino-like and higgsino-like LSPs. In models where the LSP is assumed to be DM, we need to require a relic density that is not too high. Whenever the bino-component of the LSP is large, we need a mechanism to bring down the relic density to the correct value. This mechanism can for example be annihilation via the t-channel exchange of light sfermions or chargino/slepton coannihilation.

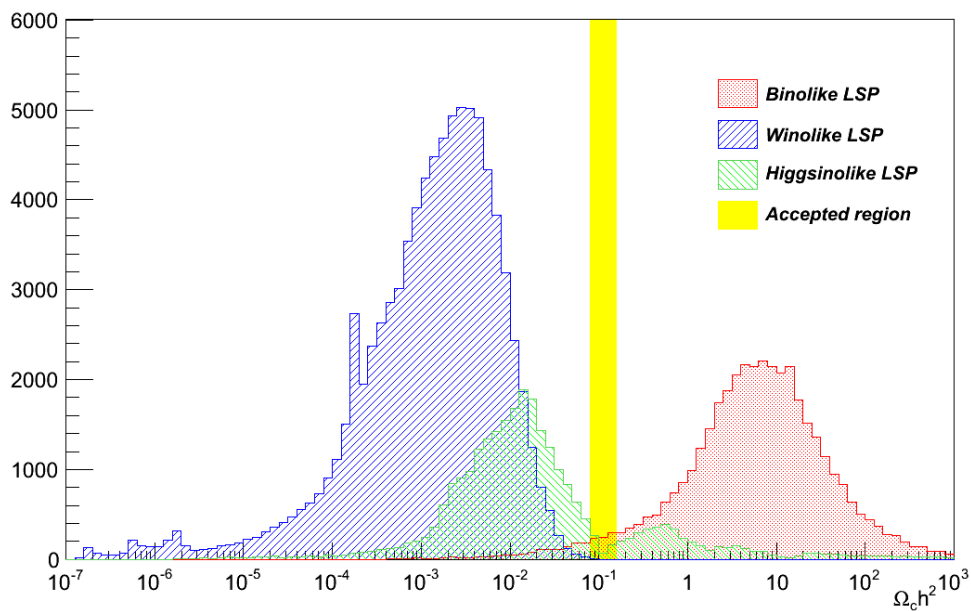


FIGURE 3.7: Dark matter relic density as obtained from the pMSSM models compared with the accepted region (yellow), extracted from ref. [19]. The vertical axis indicates the number of pMSSM models.

3.3 Particle accelerator searches

One of the goals of the currently operating particle accelerators is to find new physics. Although the production of a new weakly interacting, electromagnetically neutral and stable particle would not verify that this object is in fact the particle responsible for the dark matter that we detect in our universe, it would surely be very exciting. Such a WIMP would not leave a signal in our detector, because it leaves the detector without interaction (like neutrinos). This means that a considerable amount of energy and momentum could be carried away, resulting in *missing transverse energy*. Several accelerator experiments have searched for SUSY or DM, but no new particles have been found, resulting in constraints placed on supersymmetric particle masses and interactions. Many searches have concentrated on specific SUSY realizations, such as mSUGRA or the CMSSM. These limits are not easily translated to the pMSSM and these searches will therefore not be discussed here.

LHCb [33]: The Large Hadron Collider (LHC [34]), situated at CERN, is a circular proton-proton accelerator. It is designed to run collisions with a center-of-mass energy of $\sqrt{s} = 14$ TeV and with a luminosity of $10^{34} \text{ cm}^{-2} \text{ s}^{-1}$. The Large Hadron Collider beauty (LHCb) is one of the four main detectors of the LHC. This detector is specialized in measuring B mesons, composed of a bottom anti-quark with either an up, down, strange or charm quark. The B_s^0 (strange B meson) is an unstable particle that decays via the weak interaction. The direct decay resulting in the process $B_s^0 \rightarrow \mu^+ \mu^-$ is suppressed because the Z boson cannot couple directly to quarks of different flavors. However, higher order decays are allowed in the SM as shown in figure 3.8. The corresponding decay of a B^0 meson ($\bar{b}d$) is even more suppressed as it requires two jumps across generations rather than just one. The branching ratios of these two decays are calculated in the SM to be: $\text{BR}(B_s^0 \rightarrow \mu^+ \mu^-)_{\text{SM}} = (3.6 \pm 0.2) \cdot 10^{-9}$ and $\text{BR}(B_d^0 \rightarrow \mu^+ \mu^-)_{\text{SM}} = (1.1 \pm 0.1) \cdot 10^{-10}$. The MSSM includes new particles that can modify these branching ratios through new processes, as can be seen in figure 3.8. Measurements of the branching ratio of the B meson revealed that $\text{BR}(B_s^0 \rightarrow \mu^+ \mu^-) = (2.8_{-0.6}^{+0.7}) \cdot 10^{-9}$ and $\text{BR}(B_d^0 \rightarrow \mu^+ \mu^-) = (3.9_{-1.4}^{+1.6}) \cdot 10^{-10}$.

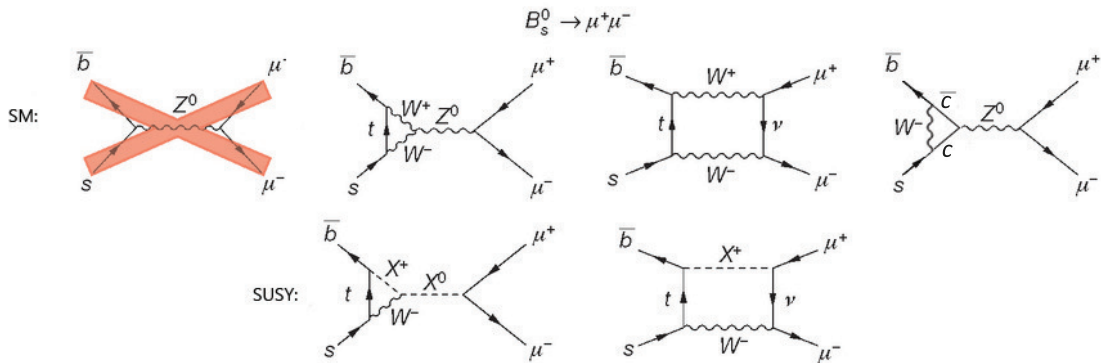


FIGURE 3.8: Examples of B_s^0 meson decays relevant for the muon decay channel. Top: SM processes, where annihilation into a Z boson is not allowed. Bottom: SUSY processes, X is any SUSY particle that can couple. Extracted from ref. [33]

ATLAS and CMS [35, 36]: ATLAS and CMS are two other detectors of the four main detectors of the LHC. The Higgs mass has been measured by ATLAS and CMS to be 125.4 GeV (ATLAS [35]) and 125.0 GeV (CMS [36]) with uncertainties of 0.3-0.4 GeV. The Higgs mass in the SM is a free parameter, but this is not true in the MSSM. The MSSM has an extended Higgs sector with two complex Higgs doublets (amounting to 8 degrees of freedom), which gives rise to five physical Higgs bosons (the other three d.o.f. are absorbed in the massive gauge bosons of the SM). At tree level, the MSSM Higgs sector is governed by M_A and $\tan\beta$ only. If $M_A \gg M_Z$, the Higgs mass is bounded from above by $m_{h^0}^2 < M_Z^2 \cos^2\beta$. If we include loop corrections, the approximate one-loop equation for the Higgs mass is given by [37]:

$$m_{h^0}^2 = M_Z^2 \cos^2(2\beta) + \frac{3m_t^4}{2\pi^2 v^2} \left(\log\left(\frac{M_S^2}{m_t^2}\right) + \frac{X_t^2}{M_S^2} \left(1 - \frac{X_t^2}{12M_S^2}\right) \right),$$

where $M_S = \sqrt{m_{\tilde{t}_1} \cdot m_{\tilde{t}_2}}$ and $X_t = A_t - \mu \cot\beta$. Accounting for an additional theoretical error of 3 GeV, we select only models with a lightest Higgs boson (h^0) mass within the range of $122 \text{ GeV} \leq m_{h^0} \leq 128 \text{ GeV}$, which sets relations between $\tan\beta$, X_t and M_S , as shown in figure 3.9. Only scenarios with large X_t/M_S values survive the Higgs mass constraint. In particular, $X_t = 0$ (which indicates that there is no mixing in the stop sector) is mostly ruled out for small values of $\tan\beta$.

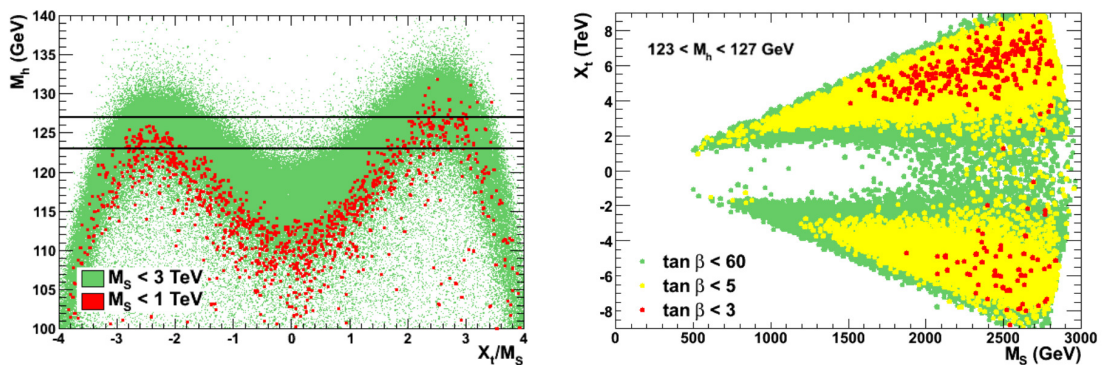


FIGURE 3.9: *Left:* The one loop Higgs mass versus the X_t/M_S , with $1 < \tan\beta < 60$, $50 \text{ GeV} \leq |\mu| \leq 1.5 \text{ TeV}$. The black lines indicate the $123 \text{ GeV} \leq m_{h^0} \leq 127 \text{ GeV}$ limits (note that we allow for 1 GeV extra uncertainty of the Higgs mass). *Right:* Contours for $123 \text{ GeV} \leq m_{h^0} \leq 127 \text{ GeV}$ for some ranges of values for $\tan\beta$. Extracted from ref. [37]

LEP [38, 39]: The four LEP collider experiments have performed several high precision measurements. In LEP, electrons and positrons were accelerated up to $\sqrt{s} = 209 \text{ GeV}$. The production of gauginos in the e^+e^- collision was an expected signal of the MSSM. The signal could consist of chargino production, which decay into two neutralinos and two fermion-pairs ($l\nu l\nu$, $qq l\nu$ or $qqqq$). The signal depends mainly on the mass difference of the chargino and LSP. None of the SUSY searches in LEP has however revealed an excess of signal events over the expected SM background events. This conclusion puts a constraint on the mass of the lightest chargino of $m_{\tilde{\chi}_1^\pm} > 103.5 \text{ GeV}$, or, if $m_{\tilde{\chi}_1^0} - m_{\tilde{\chi}_1^\pm} < 4 \text{ GeV}$, $m_{\tilde{\chi}_1^\pm} > 92 \text{ GeV}$.

Furthermore, the LEP experiments set an upper bound for the invisible width of the Z boson ($Z \rightarrow XX$ where X is any particle that is not detected) at $\Gamma_{\text{inv}} < 3.2 \text{ MeV}$.

Chapter 4

Annihilating Dark Matter

The center of the Milky Way galaxy is a natural place to look for dark matter signals. First of all, as explained in chapters 1 and 3, the inner area of our galaxy is believed to host a high density of dark matter. A high dark matter density could lead to a high rate of dark matter annihilation. Dark matter annihilation can lead to the production of photons in the energy range of a GeV up to several TeV (depending on the mass of the WIMP). These photons are referred to as γ -rays due to their high energies. Secondly, the photon flux scales with the distance r as r^{-2} , so due to the proximity of the center of our galaxy this makes up for an ideal source.

However, the Galactic Center (GC) suffers from foreground and background contamination. At the center, a compact γ -ray source is situated, which is believed to be the supermassive black hole Sgr A* [40]. Furthermore, it is uncertain what the DM density profile looks like in the GC [41].

Dwarf spheroidal galaxies, satellites of our Milky Way, make up for another perfect indirect DM detection search channel. These objects, although having a lower DM density and thus lower DM annihilation rates, suffer from less background contamination than the GC.

This chapter is organized as follows. First we will look at the observations leading to the photon excess spectra observed in the GC and in the dwarf galaxy Reticulum II. Then we will present an explanation for these excesses, considering the pMSSM model.

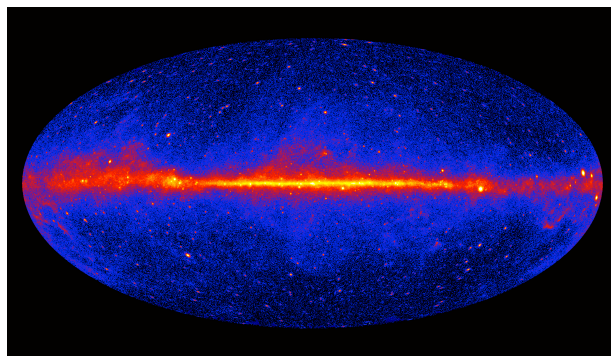


FIGURE 4.1: The sky at photon energies above 1 GeV observed by the Fermi Gamma-ray Space Telescope [30].

4.1 Astrophysical observations

4.1.1 Galactic Center

The Fermi Large Area Telescope (LAT [30]) observes the Galactic Center and is sensitive to high-energy photons (or γ -rays). There are many individual point sources of γ -rays, but there is also a significant amount of γ -ray emission from gas in our galaxy. This emission stretches out in a band across the sky (see figure 4.1).

Cosmic rays consisting of hadrons and electrons are the main source of γ -rays. These γ -rays originate primarily through the decay of π^0 . The electrons can produce γ -rays through bremsstrahlung, but with a different spectral shape than the π^0 decay spectrum. The same electrons also produce inverse Compton emission. By knowing the density of the interstellar gas and the cosmic rays, an estimate can be made on how many γ -rays originate from these interactions. A density estimation on the interstellar gas can be made using atomic hydrogen and its ‘21 cm line’, which is produced by the hyperfine transition of the atom. The amount of cosmic rays can be estimated by observing synchrotron radiation (with radio frequencies) that is produced when electrons pass through a magnetic field [42].

Other sources of γ -rays include point sources, for example the point source associated with Sgr A*, which is one of the brightest sources of γ -rays in the Galactic Center. Most searches that are focused on the GC therefore exclude the central region of galactic latitude $b < 0.2^\circ$. Due to the limited angular resolution of γ -ray telescopes, many of the point sources that reside in the inner regions of our Galaxy are unknown. Recently, the Fermi collaboration published an extensive background study on the Galactic Center [43]. After subtraction of all known background sources and accounting for an additional unknown component, their conclusion is that an extended residual is still present. This excess signal may be explained by annihilating WIMPs.

Annihilating WIMPs is an attractive explanation, but not the only one. An alternative astrophysical explanation to account for some of the γ -ray excess emission are millisecond pulsars [44]. These objects have a spectrum that has a similar power law (PL) index as the GC residual.

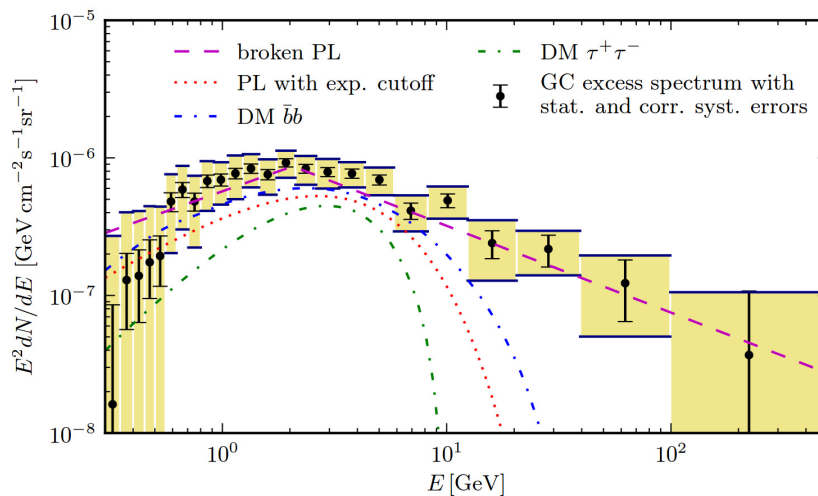


FIGURE 4.2: Spectrum of the Galactic Center excess emission (black dots) together with the statistical and systematic errors. Fits for this excess spectrum using various models are shown as well. Extracted from ref. [45].

4.1.2 Reticulum II

Reticulum II is a dwarf galaxy, located at 49.7° below the Galactic plane at a distance of 30 kpc. It is far from any known γ -ray emitting source. Previous studies on dwarf galaxies found no excess, setting strong limits on the velocity-weighted cross section for dark matter annihilation (chapter 3). Reticulum II, however, is the first dwarf galaxy to show a small γ -ray excess.

Using the Fermi science tools and including events within 0.5° of this dwarf galaxy and energies between 0.2 GeV and 300 GeV, ref. [46] finds an excess between 2 and 10 GeV with a local significance of $\sim 2.3\sigma$ (figure 4.3). Two background models are shown, the difference will briefly be explained below. The error bars are Poisson distributed errors on the number of counts, given by:

$$P(n|\lambda) = \frac{\lambda^n e^{-\lambda}}{n!}, \quad (4.1)$$

where P is the probability to observe n events when λ are expected (the latter one is equal to the number of photon counts recorded with the detector and indicated by the numbers in figure 4.3). Shown are the 1σ error bars.

The *diffuse background model* accounts for an estimate of all γ -rays originating from our galaxy, while the *isotropic background model* accounts for everything else. The intensity of the latter one is usually attributed to the γ -ray emission from unresolved extragalactic sources, like blazars, pulsars and star forming galaxies. Remaining residual or misclassified cosmic ray emission is also included in the isotropic background model [47].

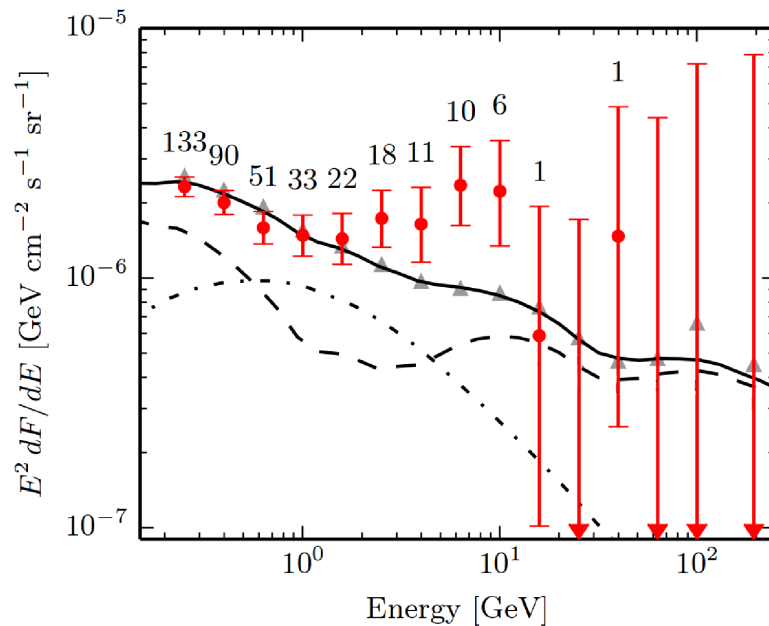


FIGURE 4.3: Energy spectrum of events detected with 1σ Poisson error bars. The solid black line is the sum of the Fermi Collaboration's models for isotropic (dashed) and galactic diffuse (dot dashed) emission. The number of photons counted in each energy bin is shown above the error bar. We see that between 2 GeV and 10 GeV, the signal rises above the background estimate. This figure is extracted from ref. [46].

4.2 Explanation in terms of WIMP dark matter

In 2009, Dan Hooper and Lisa Goodenough proposed a possible explanation for annihilating DM for the Galactic Center excess [48]. The proposed DM particle, by popular media often referred to as the *hooperon*, is a WIMP effective field theory fermion with scalar coupling to SM particles, which annihilates to $b\bar{b}$ with a DM mass around 25-30 GeV and has a velocity-weighted annihilation cross section of $\langle\sigma v\rangle \simeq 9 \times 10^{-26} \text{ cm}^3\text{s}^{-1}$. This analysis used 1 year of Fermi data (so less stringent limits were set on e.g. $\langle\sigma v\rangle$). To present day, Hooper has suggested many more DM particle models with different dominant annihilation channels and masses.

It is important to realize, that although the general shape is fixed by demanding a certain annihilation channel (as this is due to known particle physics), one can play around with the normalization and the photon spectrum peak (as this is only dependent on the WIMP mass) [49]. It would be interesting to have a neutralino responsible for this behavior, described by a parameter range in the pMSSM, instead of a toy model WIMP. It is difficult to allow for a ~ 30 GeV neutralino in the pMSSM. First of all, the LSP cannot be pure wino or higgsino, as these will necessarily be accompanied by a chargino that is too light and therefore excluded by LEP. Pure bino particles on the other hand will have a relic density that is often way too high (chapter 3). This can be fixed by having small sfermion masses or a light chargino, but these are in tension with LEP bounds on light charged sparticles. A mostly-bino plus small-higgsino component LSP can annihilate through a Higgs or a Z boson. However, the coupling to the Z boson is constrained by the invisible width of the Z boson and by spin-dependent direct detection limits. It has been shown that it is very difficult, if not impossible, to incorporate the hooperon within the framework of the pMSSM, while satisfying all constraints [50]. Our quest becomes one of finding a parameter space in the pMSSM that can explain the GC excess, while satisfying all experimental constraints as outlined in chapter 3.

4.2.1 Simulation

It is in fact possible to explain the GC excess using the pMSSM (ref. [51]). In the following section, we show how this analysis is done. To generate a photon spectrum from DM annihilation, the following code was used:

SUSY-HIT [52] : This program computes the decay of supersymmetric particles in SUSY models. As input it uses the spectrum generated by SuSpect [53], which calculates the SUSY and Higgs particle spectrum (particle masses) in the MSSM after electroweak symmetry breaking. This calculation can be performed for several SUSY models. For the pMSSM SuSpect uses 19 parameters as input. The SUSY-HIT code is based on two existing programs: HDecay [54] and SDecay [55], which calculate the decay widths and branching ratios of the MSSM Higgs bosons and SUSY particles respectively. The results are presented in the SLHA format [56].

DarkSUSY [57] : This program computes the γ -ray flux originating from annihilating dark matter. As input we will use the output from SUSY-HIT. Besides determining the γ -ray flux, we use this program to calculate the J -factor (if necessary), the dark matter relic density and the dominant annihilation channel.

micrOMEGAs [58] : This code computes the dark matter relic density, velocity-weighted annihilation cross section, WIMP-nucleon scattering cross section (both spin dependent and spin independent) and the branching ratio of the strange B meson decaying into two muons. As input this program uses the output from SUSY-HIT.

To find scenarios in the pMSSM that satisfy all the constraints, we essentially throw darts in a 19-dimensional parameter space while hoping that our bull's-eye is large enough. It is impossible to scan the full parameter space, so we have to think of a throw strategy. To this end a particle filter is used, which assumes that ‘valid’ points lie in each other’s neighborhoods. The simulation is started by the generation of random points, which are all compared with the Galactic Center photon flux excess. The ‘best points’ (defined as the points with the lowest χ^2 -value (equation 4.4)) within this set are used to set up an iterative procedure, using these points as seeds to sample new parameters centered around these points and with Gaussian distributions as widths. Only 8 parameters are found to influence relevant parameters for the analysis, like the masses of the neutralinos and charginos, the Higgs mass and the spin independent cross section. These 8 parameters are:

$$M_1; M_2; \mu; \tan\beta; M_A; m_{\tilde{u}_3}; m_{\tilde{Q}_3}; A_t. \quad (4.2)$$

For all ‘good fit’ scenarios we demand they satisfy the experimental constraints as outlined in chapter 3, summarized by:

- The lightest neutralino is the LSP.
- LEP limits on the chargino mass.
- $122 \text{ GeV} < m_{h_0} < 128 \text{ GeV}$.
- Upper limits from the LUX experiment on the spin-independent cross section.
- Upper limits from IceCube on the spin-dependent cross section.

In particular, no demands on the DM relic density were made. With these scenarios the particle filter is trained using χ^2 , which compares the GC excess spectrum with the generated spectrum:

$$\chi^2 = \sum_{i,j} (d_i - m_i) \Sigma_{ij}^{-1} (d_j - m_j), \quad (4.3)$$

where i, j are energy bin numbers, Σ_{ij} is the covariance matrix containing statistical and systematic uncertainties, d_i is the observed photon flux and m_i the computed photon flux. Usually the χ^2 -value is translated into a p -value. This value indicates the probability of having a certain outcome, assuming that a certain hypothesis is true. When the p -value is less than a chosen significance level (typically 0.01 or 0.05), this suggests that the outcome is inconsistent with the hypothesis. We will choose a significance level of 0.05.

The main sources of uncertainties that enter the analysis are:

- **J -factor:** This is a normalizing factor on the photon flux, as can be seen in equation 3.2. The J -factor depends on the DM density, which is very uncertain in the inner regions of the GC. For the GC it is estimated to be in the range of $\log_{10}(J) = 22.5 - 24.0 \text{ GeV}^2 \text{cm}^{-5}$ [59].
- **Systematic uncertainties originating from high energy physics:** The excess photon spectrum is described by DM annihilation to various SM products, which decay further in quarks or leptons. Quarks result in a parton shower that can radiate photons almost continuously. At the energies at which the Fermi instrument measures, the hadronization has not been measured accurately. This

means that uncertainties stemming from different parton shower models are introduced (see ref. [60] for details). For the GC fit an uncertainty of 10% is accounted for. The definition of χ^2 then changes into:

$$\chi^2 = \sum_{i,j} (d_i - m_i)(\Sigma_{ij} + \delta_{ij}\sigma_s^2)^{-1}(d_j - m_j), \quad (4.4)$$

where σ_s^2 equals 10%. The energy bin numbers i and j run from 1 to 24, as can be seen in figure 4.2. We will refer to this χ^2 as χ_{10}^2 , and the χ^2 without this 10% uncertainty will be denoted as χ_0^2 .

4.2.2 Galactic Center

Fitting the resulting photon fluxes, generated by DarkSUSY, to the Galactic Center excess resulted in three pMSSM parameter ranges [51]. We will refer to these three regions as $t\bar{t}$, WW(1) and WW(2).

The LSPs of the scenarios in the $t\bar{t}$ region annihilate mainly to pairs of top quarks. The best fit scenarios have a p -value, using the photon spectrum obtained from pMSSM SUSY models as hypothesis, of 0.1 (using 24 d.o.f.). This value indicates that the GC photon spectrum is probably consistent with a photon spectrum obtained from these pMSSM SUSY models, as it is higher than 0.05. The LSP in this region of parameter space is almost exclusively bino, which means that it couples very little to SM bosons. WW(1) describes a region in the pMSSM parameter space where the lightest neutralinos annihilate primarily to pairs of W bosons. This region provides the best fit to the Galactic Center excess, with a lowest χ_{10}^2 of 27. This corresponds to a p -value of 0.3. The composition of the lightest neutralino is in this case $\sim 50\%$ bino and $\sim 50\%$ higgsino. In the WW(2) region, the LSP will mainly annihilate to W bosons. The difference with the WW(1) region, is that the LSP composition is different: 90% bino, 4% higgsino and 6% wino. The best scenario in this region has a p -value of 0.15.

Values for the relevant parameters are given in table 4.1. The composition of the neutralinos and charginos in terms of interaction eigenstates of these three parameter spaces can be seen in figure 4.5. Their masses are given in table 4.1. Figure 4.4(a) shows the dark matter relic density for the three parameter spaces. Remarkable is that the dark matter density for these regions, which can vary from 10^{-7} to 10^3 (figure 3.7), comes out about right, although this constraint was not imposed.

	$t\bar{t}$	WW(1)	WW(2)		$t\bar{t}$	WW(1)	WW(2)
M_1 (GeV)	170-179	106-110	91-95	$M_{\tilde{\chi}_1^0}$ (GeV)	173-180	84-86	86-91
M_2 (GeV)	197-1550	374-475	102-111	$M_{\tilde{\chi}_2^0}$ (GeV)	220-980	106-110	105-113
μ (GeV)	397-3850	108-110	311-484	$M_{\tilde{\chi}_3^0}$ (GeV)	410-3855	145-147	325-500
$\tan\beta$	5.0-50	25-43	5.0-11	$M_{\tilde{\chi}_4^0}$ (GeV)	430-3855	420-523	339-507
M_A (GeV)	598-3982	617-1358	1018-3843	$M_{\tilde{\chi}_1^\pm}$ (GeV)	220-980	107-109	103-110
$m_{\tilde{u}_3}$ (GeV)	531-911	1686-2957	677-2713	$M_{\tilde{\chi}_2^\pm}$ (GeV)	430-3855	520-523	340-506
$m_{\tilde{Q}_3}$ (TeV)	1.5-3.7	0.8-2.8	1.3-3.3				
A_t (TeV)	3.0-4.0	3.0-4.0	3.0-4.0				

TABLE 4.1: Values for the pMSSM input parameters that define the $t\bar{t}$, WW(1) and WW(2) region.

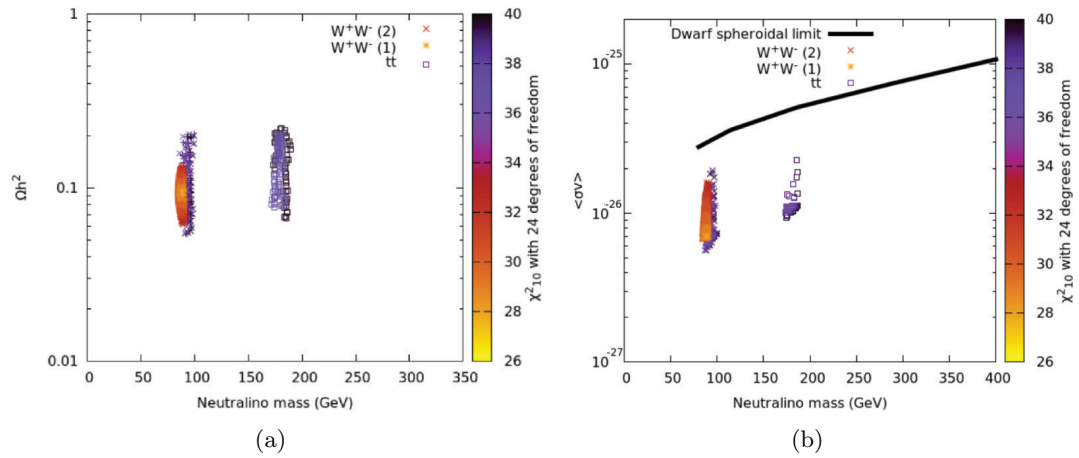


FIGURE 4.4: *Left*: LSP relic density (Ωh^2) as a function of the lightest neutralino mass. χ^2_{10} is shown as a color code. The WW(1) region is indicated by a star, the WW(2) region by a cross and the $t\bar{t}$ region by a box. *Right*: LSP velocity-weighted annihilation cross section $\langle\sigma v\rangle$ as a function of the lightest neutralino mass. χ^2_{10} is shown as a color code. The black solid line indicates the 95% upper limit derived from dwarf galaxy observations. Figures are extracted from ref. [51].

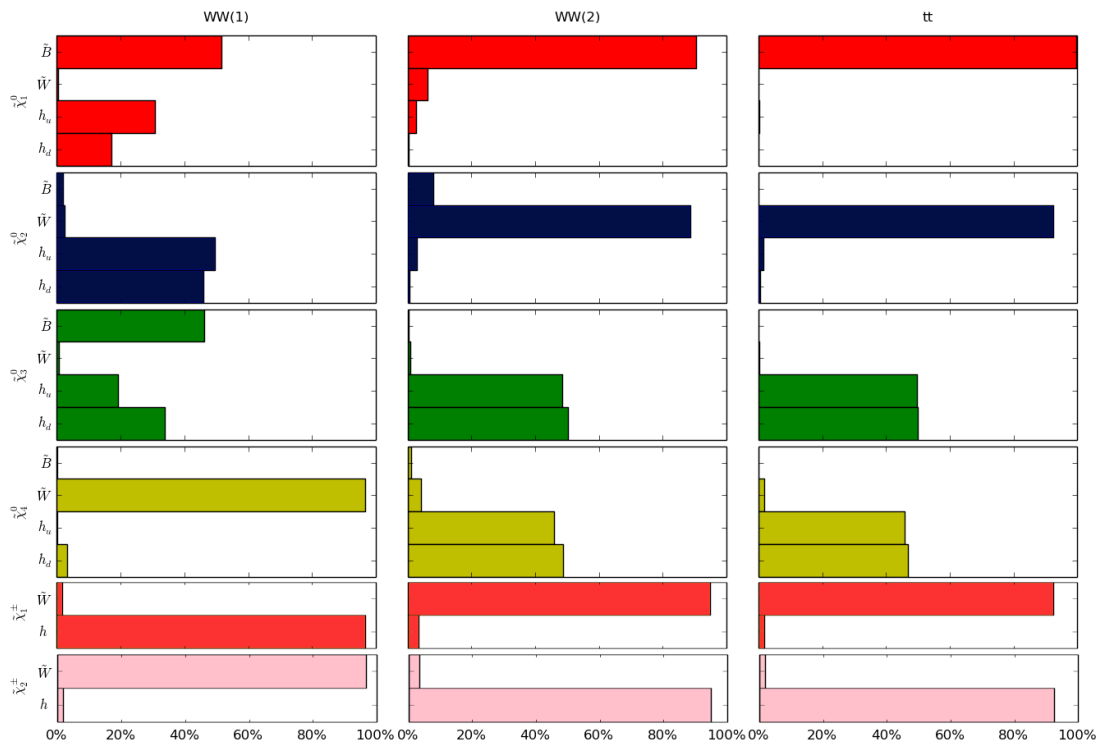


FIGURE 4.5: Average composition of neutralinos and charginos for all three pMSSM parameter spaces.

4.2.3 Reticulum II

We adopt the 50 best GC fit scenarios for each pMSSM parameter range to fit their photon spectrum to the Reticulum II excess spectrum. We leave the J -factor as a free fitting parameter. In addition to these three parameter spaces, we consider an additional 50 GeV neutralino and consider only its $b\bar{b}$ annihilation channel¹. Note that this particle cannot be made in the pMSSM whilst also having the right relic density and velocity-weighted annihilation cross section. We therefore artificially put $\langle\sigma v\rangle \simeq 1.3 \times 10^{-26} \text{ cm}^3\text{s}^{-1}$, which is the upper limit for the velocity-weighted annihilation cross section that ref. [61] also used to explain the Reticulum II excess. The error bars of Reticulum II are uncorrelated, so we use the following χ^2 definition:

$$\chi^2 = \sum_i \frac{(d_i - m_i)^2}{\sigma_i^2}, \quad (4.5)$$

where i is the energy bin number (which runs from 1 to 15), d_i is the observed photon flux, m_i the computed photon flux and σ_i the Poisson errors (equation 4.1). The Poisson errors are not symmetric, so we will use σ_{up} if m_i lies above d_i and σ_{down} if m_i lies below d_i . In figure 4.6 we show the best fit scenarios for the Reticulum II excess for each of the four parameter ranges. We have a few options for defining our fit region.

First of all we could use the total signal. The number of degrees of freedom (d.o.f.) in this case is counted as follows: there are 15 bins in total, we lose 1 d.o.f. because the background is used in the fit and we lose another one because we use the J -factor as a free fitting parameter. This means we will end up with 13 d.o.f. for the total signal. We will use the corresponding best p -value to determine the J -factor. The total signal is however dominated by the background, and since we add up the expected background to the DarkSUSY photon flux, we get p -values that are artificially very high.

To this end we define two other regions for which we evaluate the p -value after we determined the J -factor using the total signal: the *observed excess region* and the *expected excess region*. The observed excess region is defined as the region between 2 GeV and 10 GeV where the excess was reported by ref. [46].

We define the expected excess region as the range of consecutive bins for which the p -value:

$$p_i(\text{signal} + \text{background} | \text{background}) \quad (4.6)$$

is minimized. Here, i denotes a continuous bin range, which we require to be at least 4, as the observed excess region also consists of 4 bins. In equation 4.6, signal refers to the photon flux as given by DarkSUSY. For this p -value we test the outcome of DarkSUSY, assuming that the background model is true (given by the solid black line in figure 4.3). Note that this definition differs from the one we use to present our results, in which case we assume the outcome of DarkSUSY as a hypotheses. If the minimized p -value is small, it indicates that the outcome of DarkSUSY rises above the background, which is where we would expect an excess. The χ^2 -value is calculated in the usual way and we use (number of bins) - 1 as the number of degrees of freedom. Note that since we now fixed the J -factor, this is no longer a free parameter, so we gain 1 degree of freedom. The expected excess region corresponds to the region where the best discrepancy between signal and background can be made. In this calculation we need an estimate of the error on the background, which was not given by the authors of ref. [46]. We therefore make

¹This is inspired by the hooperon and is for comparison only.

	Reticulum II data	Observed excess region	Expected excess region
$t\bar{t}$	0.85	0.36	0.53
WW(1)	0.79	0.27	0.36
WW(2)	0.81	0.31	0.40
bb	0.63	0.09	0.24
background	0.37	0.01	0.03

TABLE 4.2: The p -values for the three GC regions and the $b\bar{b}$ scenario corresponding to the Reticulum II measured data, the observed excess region from 2 to 10 GeV (as indicated in figure 4.6 by the blue box) and the expected excess region (as indicated in figure 4.6 by the red box). In the last row we include p -values for a background only model to explain the Reticulum II measured data, the observed excess region and the expected excess region. A high p -value suggests that the proposed model is consistent with the measured photon flux.

our own estimate, and adopt the relative Poisson distributed errors on the Reticulum II measured data:

$$\sigma_{\text{background},i} = \frac{\sigma_{\text{signal}_i} \cdot \text{background}_i}{\text{signal}_i}. \quad (4.7)$$

We find that the expected excess region is the same for all four regions, namely between 1 GeV and 7 GeV, and consists of 5 bins. After we found the expected excess region, we calculated the p -value for the outcome of DarkSUSY to be consistent with the Reticulum II measured photon spectrum in this region.

The results of our analysis are shown in table 4.2 and are discussed below. In table 4.2 we also include p -values for the background to explain the Reticulum II measured data in each of the three defined fit regions. In figure 4.6 the resulting photon spectra are shown, as well as the observed and expected excess regions indicated by a blue and a red box respectively.

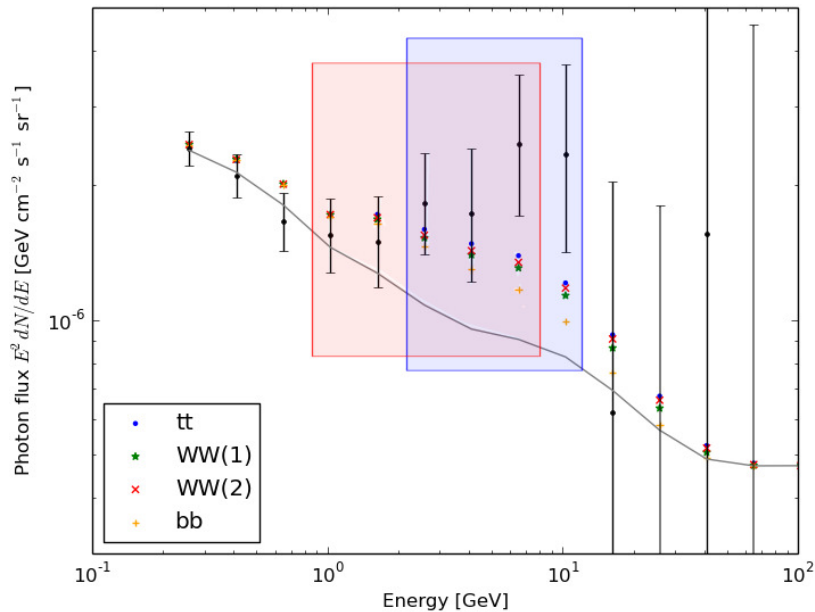


FIGURE 4.6: Photon spectrum for Reticulum II. Between 2 GeV and 10 GeV, the photon spectrum rises above the background. This observed excess region is indicated by the blue box. The colored points are fluxes generated by DarkSUSY of the best fits for three GC regions: $t\bar{t}$ (blue), WW(1) (green) and WW(2) (red), and bb (orange), added to the background of Reticulum II. The red box indicates the expected excess region, as determined by equation 4.6.

$t\bar{t}$: This region yields the best results with a χ^2 ranging between 7.75 and 7.93 (corresponding to a p -value of ~ 0.85 if we use 13 degrees of freedom). The resulting J -factor is $\log_{10}(J(\alpha_{int})) = (20.33 - 20.56)_{-0.23}^{+0.15} \text{ GeV}^2\text{cm}^{-5}$. The mean of the J -factor corresponding to a χ^2 value of $(\text{minimal } \chi^2) + 1$ indicates the 1σ range. The numbers between brackets show the range of best-fit J -factors for the 50 different scenarios within the $t\bar{t}$ parameter space.

WW(1): This region gives a slightly worse fit with a mean χ^2 value of 8.75, which corresponds to a p -value of 0.79 using 13 degrees of freedom. The resulting J -factor is $\log_{10}(J(\alpha_{int})) = (20.31 - 20.35)_{-0.25}^{+0.16} \text{ GeV}^2\text{cm}^{-5}$.

WW(2): This region gives a J -factor of $\log_{10}(J(\alpha_{int})) = (20.25 - 20.55)_{-0.25}^{+0.15} \text{ GeV}^2\text{cm}^{-5}$. These have χ^2 between 8.35 and 8.66, corresponding to a p -value of 0.81.

$b\bar{b}$: This scenario results in a J -factor of $\log_{10}(J(\alpha_{int})) = 19.57_{-0.35}^{+0.19} \text{ GeV}^2\text{cm}^{-5}$, which is lower than the reported J -factors for the $t\bar{t}$, WW(1) and WW(2) regions. The fit is worse, $\chi^2 = 10.7$ with a p -value of 0.63.

We can now compare the resulting J -factors with J -factors for Reticulum II found in the literature. The J -factors are determined by first measuring the line of sight velocities of member stars. Then, with the assumption of a dwarf galaxy being a collisionless spherical symmetric system, one can derive from the collisionless Boltzmann equation a *Jeans equation* [62]:

$$\frac{GM(r)}{r} = \langle v_r^2 \rangle \left(-\frac{d \log \rho_s}{d \log r} - \frac{d \log \langle v_r^2 \rangle}{d \log r} - 2\beta \right), \quad (4.8)$$

where $\langle v_r^2 \rangle$ is the average squared radial velocity, ρ_s the stellar density and $\beta = 1 - (\langle v_\theta^2 \rangle + \langle v_\phi^2 \rangle) / (2\langle v_r^2 \rangle)$ is the velocity anisotropy. This velocity anisotropy can usually only be estimated, because, due to the large distances between dwarf galaxies and us, only the line of sight component of the velocity can be measured. The first two terms on the right-hand side describe the internal gas pressure that prevents the dwarf galaxy from collapsing due to the effects of gravity. The number density ρ_s is deduced from the brightness of a dwarf galaxy. If all these quantities are measured and estimated, we can derive the mass distribution of the system.

The procedure seems straightforward, but it is subject to many sources of uncertainties. For example, it can be unclear whether a star is actually a member star of a galaxy, or some background or foreground object. These make J -factor estimations subject to large uncertainties. For Reticulum II, J -factors by two separate groups are reported: $\log_{10}(J(\alpha_{int})) = 19.5_{-0.6}^{+1.0} \text{ GeV}^2\text{cm}^{-5}$ (ref. [63]) and $\log_{10}(J(\alpha_{int} = 0.5^\circ)) = 18.9 \pm 0.6 \text{ GeV}^2\text{cm}^{-5}$ (ref. [64]). The GC regions predict a J -factor for Reticulum II between $\log_{10}(J(\alpha_{int})) = 20.0 \text{ GeV}^2\text{cm}^{-5}$ and $\log_{10}(J(\alpha_{int})) = 20.7 \text{ GeV}^2\text{cm}^{-5}$, which is within 1σ consistency with the first J -factor.

There are dwarf galaxies that are reported to have a higher J -factor, but no excess was reported in these galaxies [65]. Ref. [66] investigated such dwarf galaxies, and found that their J -factors might have been overestimated by an order of magnitude due to misclassified member stars. The J -factors can therefore vary between $\log_{10}(J) \sim 16 - 21$ from one analysis to another. Ref. [66] also reported that Reticulum II was not subject to such misidentifications. Their J -factor estimate resulted in $\log_{10}(J(\alpha_{int} = 0.5^\circ)) = 19.7_{-1.3}^{+1.0} \text{ GeV}^2\text{cm}^{-5}$.

4.3 Concluding remarks

We have found pMSSM regions that explain the Galactic Center photon excess and the smaller Reticulum II photon excess simultaneously. These regions have not been excluded by any astrophysical or particle physics experiment. Furthermore, the regions fit the Reticulum II spectrum with a J -factor that is comparable with what can be expected by the observation of spherical velocities of member stars.

At the time of writing, eight ultra-faint dwarf galaxies were discovered by ref. [67]. In the direction of Tuc III, which is at a distance of ~ 25 kpc, a weak γ -ray excess signal is reported [68]. The J -factor has been estimated, by adopting an empirical relation between the J -factor and the distance to the GC, to be $\log_{10}(J) \sim 19.5 \text{ GeV}^2 \text{cm}^{-5}$. This J -factor estimate is far from reliable and data of individual member stars is needed to get a better estimate. However, the signals originating from Tuc III and Reticulum II show some similarities and they both resemble the GC excess spectrum. This makes it an exciting observation. The origin of the excess from the GC is still under debate, but additional support for a dark matter interpretation could come from dwarf galaxies, as these are not sensitive to pollution caused by poorly known backgrounds. Preparations are being made to perform a combined analysis.

Furthermore, IceCube updated their limits on the spin-dependent WIMP-proton cross section σ_{SD} [69]. The models in the WW(1) region result in a σ_{SD} that is just below the IceCube 2012 limit, which is shown in figure 4.7(a). The new limits are presented in figure 4.7(b). The limits are not improved for WIMPs annihilating to W bosons for WIMP masses below ~ 100 GeV, because a small excess (819 observed events vs 770 predicted events) is observed in the ‘summer’ data set (recorded between September and March). This means that models in the WW(1) region are not excluded by the updated IceCube limits. The excess is not observed in the ‘winter’ data set.

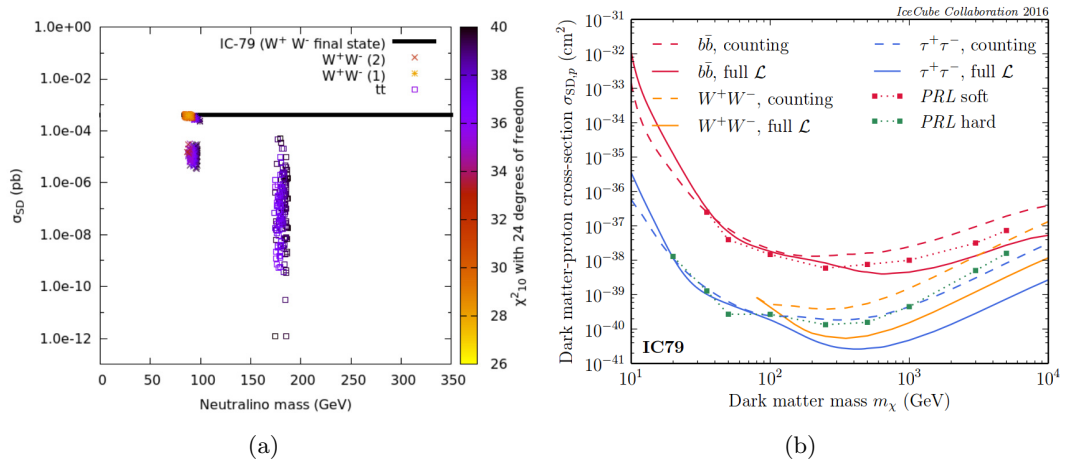


FIGURE 4.7: *Left*: Spin-dependent WIMP-proton cross section as a function of the WIMP mass. The models in the WW(1), WW(2) and $t\bar{t}$ regions are indicated by a star, a cross and a square respectively. The IceCube 2012 limit is indicated by the solid black line. χ^2_{10} is shown as a color code. *Right*: Updated IceCube limits on the spin-dependent WIMP-proton cross section as a function of WIMP mass. The original limits are indicated by PRL. The PRL hard limit resembles the W^+W^- annihilation channel for WIMP masses above the W boson mass (the solid black line in the left figure). The dashed and solid lines indicate two different forms of likelihoods that have been used. Extracted from ref. [69].

Chapter 5

LHC signature

One of the main goals of the LHC at 14 TeV is to search for BSM physics signals. One of these BSM candidates is SUSY. Searches for direct experimental evidence for SUSY include signatures from multi-jet and multi-lepton plus missing transverse energy final states. The former typically has a higher cross section, but suffers from cluttered signals and high systematic uncertainties compared to the latter.

To test the three regions as proposed in chapter 4, we ultimately want to find evidence of them in the LHC. The WW(1) and WW(2) regions have significantly lower neutralino and chargino masses than the $t\bar{t}$ region. The neutralinos and charginos will be produced in the LHC with a higher cross section if they have a lower mass, as can be seen in figure 5.1. We will therefore focus on these two regions in this chapter.

The rest of this chapter is structured as follows. First we will look at characteristics of proton proton collisions. Then we will set up a search strategy for the GC regions WW(1) and WW(2). Finally, we will present our results.

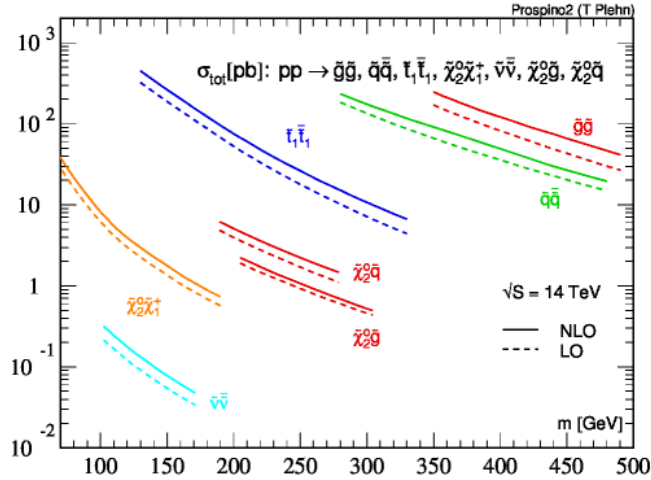


FIGURE 5.1: Cross sections in pb for proton-proton collisions to supersymmetric particles for a center of mass energy of $\sqrt{s} = 14$ TeV. All cross sections are shown as a function of the average final-state mass. Extracted from ref. [70].

5.1 Characteristics of proton-proton collisions

Protons consist of three valence quarks (u, u and d) and an indefinite number of virtual quarks, gluons and anti-quarks, collectively known as *partons*. The longitudinal component (parallel to the beam pipe) of the momentum that a parton carries is unknown in proton-proton collisions. This means that the colliding partons will take a fraction of the total momentum of the protons, so the effective $\sqrt{\hat{s}}$ will be smaller than 14 TeV. This complicates the collision picture at the LHC: two unknown partons with unknown momentum interact. The transverse component (perpendicular to the beam pipe) is 0. The total transverse momentum is conserved, so the resulting collision products can best be described by the transverse momentum (p_T) and the transverse energy (\cancel{E}_T). Proton-proton interactions will generate a large amount of events where the transferred momentum between two partons is small (*soft collisions*), but the most interesting physics will take place in events with high momentum transfer.

The substructure of protons is described by the parton distribution functions (PDF). This is a measure of the probability to find a parton in a proton carrying a fraction x of the total proton momentum. PDF are not calculated, but are determined by performing fits to data from deep inelastic scattering experiments. This makes them universal and thus applicable to any process involving the collision of hadrons after the PDF have been measured accurately in another, well-understood, process. The total production cross section of the proton-proton interaction is separated into a partonic (*hard-scattering*) part, which is a short distance effect, and a long-distance (soft collision) part. This process is called *factorization*. The energy scale at which the separation is made (factorization scale) is indicated by Q^2 . Figure 5.2 shows that the number of partons in a proton depends on the energy scale Q^2 . At low Q^2 , the valence quarks are more dominant than the virtual quarks, gluons and anti-quarks.

Other mechanisms that can complicate calculations that concern proton-proton collisions are summarized below and shown in figure 5.3.

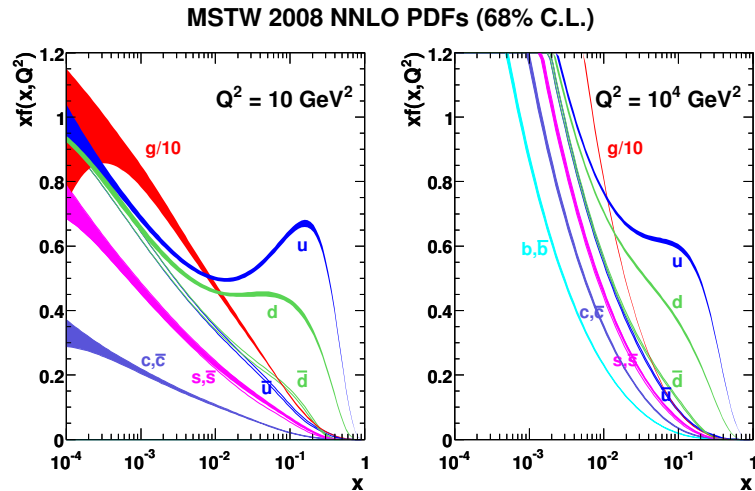


FIGURE 5.2: Product of the parton momentum fraction x and the parton distribution function $f(x, Q)$ for the scale $Q^2 = 10 \text{ GeV}^2$ (*left*) and $Q^2 = 10^4 \text{ GeV}^2$ (*right*) [71].

The band denotes the uncertainty.

- **Parton shower:** Partons lose energy by radiating off soft quarks and gluons during the hard-scattering process.
- **Initial and final state radiation:** Before or after the hard-scattering process takes place, an energetic gluon can be radiated off the incoming partons (in which case it is called *initial state radiation*, ISR) or the final state objects (*final state radiation*, FSR). Charged particles can also radiate off photons. ISR and FSR can affect the cross section (because it modifies the collision energy) and/or increase the number of final state objects.
- **Hadronization:** So far we have talked about quarks and gluons as being final state objects. However, quarks and gluons are not experimentally observable as free particles, as they group to form color-neutral hadrons. This process of grouping together is called *hadronization*. These hadrons can decay into other particles, like photons or electrons. An algorithm is used to group these decay products and hadrons into a *jet*.
- **Underlying event:** The proton remnants that were not included in the hard-scattering are colored states. Often these will result in additional soft jets in the direction of the beamline.
- **Pile up:** Due to the large proton density in the LHC, it is possible that more than one proton per beam interacts inelastically. These events can be overlaid with previous proton proton collisions if the readout system is not fast enough. We will not consider pile up in this analysis.

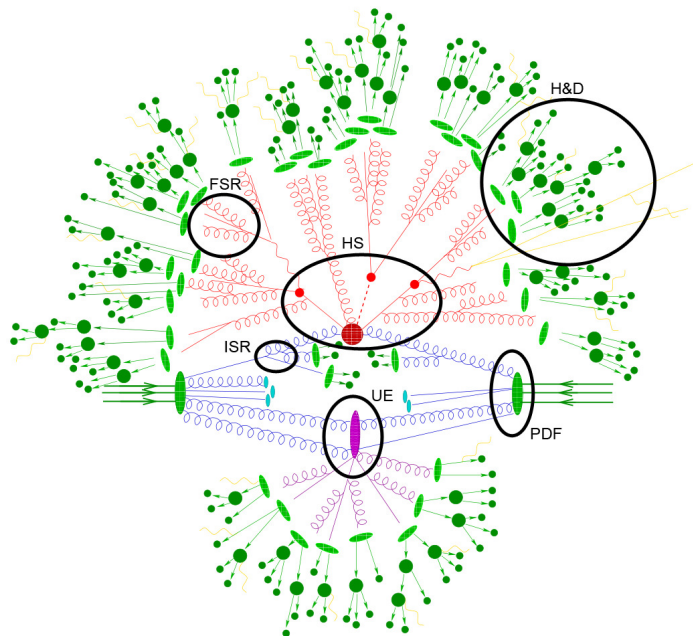


FIGURE 5.3: Illustration of a proton-proton event with all possible stages: the incoming partons as a result of the PDF, the hard-scattering event (HS), the initial and final state radiation (ISR, FSR) resulting in additional gluons (blue and red) and photons (yellow), the parton showers with hadronization and decays (H&D), and finally the underlying event (UE). The (modified) figure is extracted from ref. [72]

5.2 Tri-lepton final state search channel

In the Galactic Center fit regions, all squark and slepton masses were set at high (~ 4 TeV) energy scales, such that only the charginos and neutralinos have a small mass ($\sim M_W$). Therefore we want to focus on electroweak mediated production processes at the LHC to probe these regions. A standard search channel for this process is the multi-lepton plus missing transverse energy (\cancel{E}_T) search channel. The LHC experiments have been able to constrain electroweakino masses in this channel using *simplified* SUSY models [73]. The result obtained in the ATLAS collaboration can be seen in figure 5.4. Similar results are obtained in CMS [74]. Simplified models assume that the masses and decay modes of the relevant particles (being $\tilde{\chi}_1^\pm, \tilde{\chi}_2^0, \tilde{\chi}_1^0, \tilde{l}, \tilde{\nu}$ for the multi-lepton plus \cancel{E}_T search) are the only free parameters.

In table 4.1 we can see that the masses of the LSP and the NLSPs (next-to-lightest particles, being $\tilde{\chi}_1^\pm$ or $\tilde{\chi}_2^0$) of the WW(1) and WW(2) regions lie close together, with mass splittings of the order of 20–30 GeV. Such a *compressed* SUSY spectrum is experimentally challenging to observe. In the rest frame of the decaying $\tilde{\chi}_2^0$, the lepton energy is roughly bounded by $(m_{\tilde{\chi}_{\text{NLSP}}} - m_{\tilde{\chi}_{\text{LSP}}})/2$, as a minimum of two leptons are produced to ensure lepton number conservation. Potential multi-lepton+ \cancel{E}_T signals rely on lepton triggers that require $p_T(l) \gtrsim (15 - 20)$ GeV (with $p_T(l)$ we indicate the transverse momentum of the leptons). Furthermore, it is experimentally challenging to reconstruct and identify leptons with a low transverse momentum. Therefore, searches start to lose sensitivity when the mass differences drop below $\sim 40 - 50$ GeV.

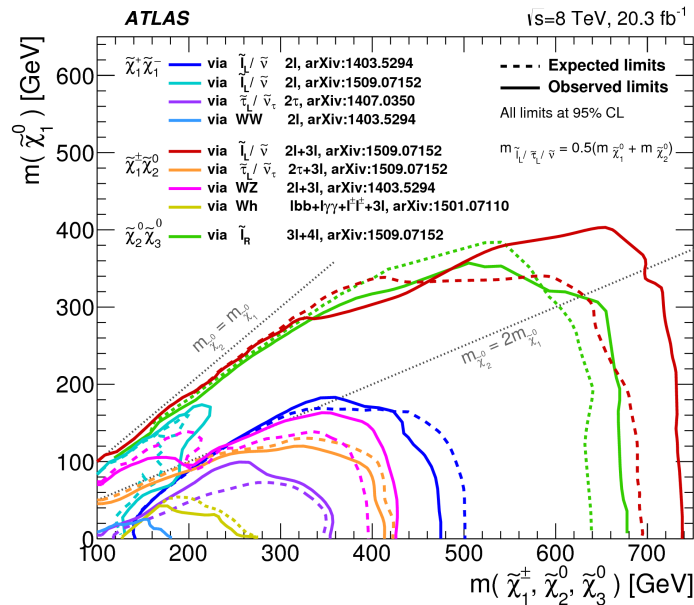


FIGURE 5.4: The 95% confidence level exclusion limits on direct production of $\tilde{\chi}_1^+ \tilde{\chi}_1^-$, $\tilde{\chi}_1^\pm \tilde{\chi}_2^0$ and $\tilde{\chi}_2^0 \tilde{\chi}_3^0$ with either W , Z , h or slepton-mediated decays. These limits are made using simplified models. This figure is extracted from ref. [75].

In scenarios where squarks and sleptons are very heavy, the direct production of charginos and neutralinos may be the dominant SUSY production channel at the LHC [76–81]. Charginos and neutralinos can be produced via the exchange of a squark or via an s-channel W boson. Due to the high squark masses, only the latter will make a contribution. Charginos can decay to leptonic final states via sneutrinos, charged sleptons or W bosons. The first two are suppressed and only the latter ($\tilde{\chi}_{1,2}^\pm \rightarrow W^\pm \tilde{\chi}_1^0 \rightarrow l^\pm \nu_l \tilde{\chi}_1^0$) makes a contribution in the WW(1) and WW(2) regions. Heavy neutralinos can decay via Z bosons ($\tilde{\chi}_{2,3}^0 \rightarrow Z \tilde{\chi}_1^0 \rightarrow l^+ l^- \tilde{\chi}_1^0$) or the Higgs boson ($\tilde{\chi}_{2,3}^0 \rightarrow h \tilde{\chi}_1^0 \rightarrow l^+ l^- \tilde{\chi}_1^0 + X$)¹, where X represents any additional decay product from the Higgs boson. However, since the mass splitting between the LSP and the NLSPs is much smaller than the Higgs mass and the Higgs boson decay width is small, the latter production channel will not make a contribution. In figure 5.5 the production process and the described dominant decay chains are illustrated. This will result in a detector signature of three leptons and missing transverse energy. Two of the three leptons will have the same flavor, because they originate from Z -mediated $\tilde{\chi}_2^0$ decay. We will refer to this lepton pair as the *opposite sign same flavor (OSSF) lepton pair*.

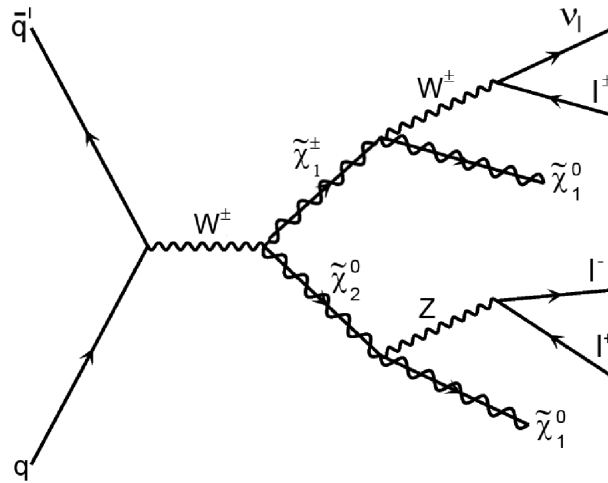


FIGURE 5.5: Chargino-neutralino production and decay to three lepton final states via gauge bosons in the LHC.

ATLAS (and CMS) have reported no excess for the $\sqrt{s} = 8$ TeV LHC, implying that all observations in the $3l + \cancel{E}_T$ channel were consistent with the SM expectations. This allowed ATLAS to set limits on pMSSM models and simplified SUSY models. In these models, only the direct production of $\tilde{\chi}_1^\pm$ and $\tilde{\chi}_2^0$ is considered. In these models, $\tilde{\chi}_1^\pm$ and $\tilde{\chi}_2^0$ are pure wino eigenstates and mass degenerate, whereas $\tilde{\chi}_1^0$ is a pure bino eigenstate. Figure 5.6 shows the limit that has been set for the tri-lepton final state for a simplified model where the decay is mediated by WZ . In this particular simplified model, all

¹And via sleptons, but this decay channel will not make a contribution under the assumption of heavy sleptons.

squarks, charged sleptons and sneutrinos are assumed to be heavy. In that case, $\tilde{\chi}_1^\pm$ and $\tilde{\chi}_2^0$ decay via W and Z bosons with 100 % branching ratio. Two limits are given: the *observed* limit and the *expected* limit. These limits are computed for the observed and expected number of beyond the SM events. If we assume a massless LSP, chargino masses up to 415 GeV for these simplified models are excluded. We can observe a reduced sensitivity for $m_{\tilde{\chi}_1^0} - m_{\tilde{\chi}_1^\pm} = M_Z$, which is due to the WZ background that resonates in this region of parameter space. We can also see that the ATLAS $3l + \cancel{E}_T$ search has not been sensitive to mass gaps smaller than ~ 30 GeV. ATLAS analyses targeting compressed spectra did not significantly improve these limits [82].

A lot of work has already been done to gain sensitivity in compressed scenarios using the tri-lepton WZ mediated production channel. To improve the search sensitivity for small mass gap regions, the production of a hard initial state object, for example a jet (ref. [84–86]) or photons (ref. [87–89]) has been studied. The use of soft leptons in combination with a jet has been suggested as well (ref. [78,90,91]). Other suggested methods include the search for two, three or four soft leptons together with large (> 50 GeV) missing energy [92,93]. Apart from selecting a smart final state topology, cuts on, for example, the allowed lepton or jet energy can be done to enhance the signal sensitivity. In table 5.1 a short summary of the *cuts* that are used in some of the existing searches is given.

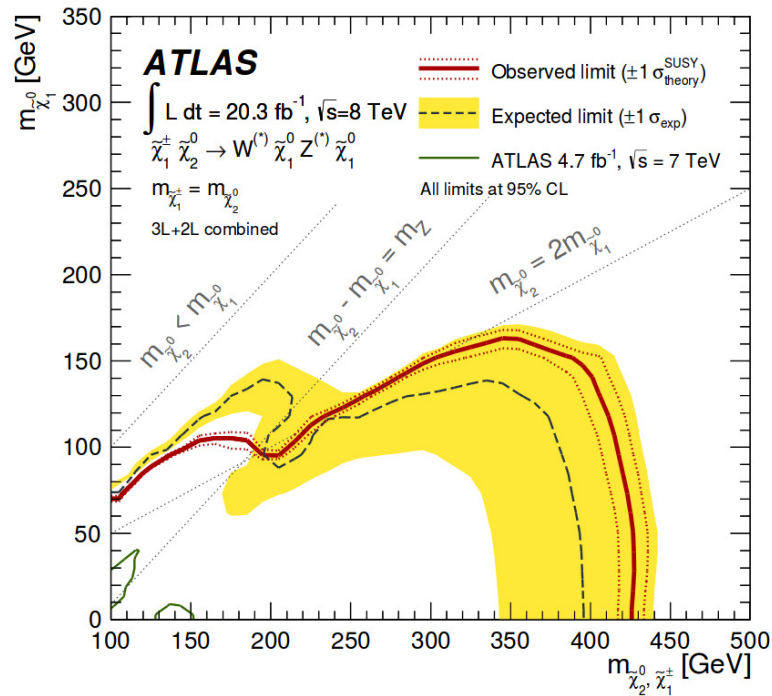


FIGURE 5.6: Observed and expected limits for chargino and neutralino production in a simplified model scenario. The band around the expected limit (indicated by a dashed black line) shows the $\pm 1\sigma$ variation. The red line indicates the current limit for 20.7 fb^{-1} , the dotted red lines indicate the sensitivity to $\pm 1\sigma$ variations on this limit. The green line indicates the old limit using 4.7 fb^{-1} of $\sqrt{s} = 7$ TeV data. Extracted from ref. [83].

search	signal selection
	ATLAS and CMS tri-lepton searches
ATLAS [82, 83, 94–97]	single e and μ trigger: $p_T(l_1) > 25$ GeV symmetric di-muon: $p_T(\mu_1)$ and $p_T(\mu_2) > 14$ GeV asymmetric di-muon trigger: $p_T(\mu_1) > 18$ GeV and $p_T(\mu_2) > 10$ GeV symmetric di-electron: $p_T(e_1)$ and $p_T(e_2) > 14$ GeV asymmetric di-electron trigger: $p_T(e_1) > 25$ GeV and $p_T(e_2) > 10$ GeV electron-muon (muon-electron) combi trigger: $p_T(e_1) > 14(10)$ GeV and $p_T(\mu_1) > 10(18)$ GeV At least one OSSF lepton pair with $12 < M_{l+l^-} < 60$ GeV $\cancel{E}_T > 50$ GeV $p_T(l_3) > 10$ GeV
CMS [98–100]	single e and μ trigger: $p_T(e) > 27$ GeV or $p_T(\mu) > 24$ GeV di-muon or di-electron or combination: $p_T(l_1) > 20$ and $p_T(l_2) > 10$ GeV At least one OSSF lepton pair with $12 < M_{l+l^-} < 75$ GeV $\cancel{E}_T > 50$ GeV $p_T(l_3) > 8$ GeV
	Soft tri-lepton searches
1312.7350 [78]	only allow for soft leptons $5 < p_T(\mu) < 20$ GeV and $10 < p_T(e) < 20$ GeV (veto on higher p_T leptons) $\cancel{E}_T > 300 - 1000$ GeV and $p_T(j_1) > 300 - 1000$ GeV (50 GeV steps) $\Delta\phi(j_1, j_2) < 2.5$ $p_T(j_3) < 30$ GeV
1307.5952 [91]	Exactly 3 leptons with $7 < p_T(l) < 50$ GeV At least one OSSF lepton pair with $12 < M_{l+l^-} < 30$ GeV Initial state radiation jet with $p_T(j) > 30$ GeV, $ \eta(j) < 2.5$ $\cancel{E}_T > 20$ GeV
1511.05386 [93]	Exactly 3 leptons recorded with any of the ATLAS lepton triggers At least one OSSF lepton pair with $12 < M_{l+l^-} < 40$ GeV $\cancel{E}_T > 50$ GeV

TABLE 5.1: Overview of cuts used in various proposed $3l + \cancel{E}_T$ searches at the LHC. For the ATLAS and CMS cuts, the leptons need to satisfy any of the lepton p_T requirements.

5.3 Backgrounds to the tri-lepton final state

Backgrounds to the $3l + \cancel{E}_T$ final state as discussed above can be classified into two categories: irreducible and reducible background. Irreducible backgrounds mimic the signal signature because they have the exact same final state, whereas reducible backgrounds only appear to have the same final state due to mismeasurements. The backgrounds that we will consider are described below. In all cases, only leptonic decays of the gauge bosons are considered.

WZ*/ γ *: This will be the main irreducible background that we will consider. This background will have a resonance at M_{l+l-} close to the Z boson mass, and at low M_{l+l-} originating from J/ψ mesons, Υ mesons and low-mass Drell-Yan processes (figure 5.7).

WW: This process contains two leptons and missing transverse energy due to two escaping neutrinos. A third lepton may be faked by initial state radiation.

ZZ: This process has two or four final leptons. Missing transverse energy can originate from neutrinos (in the case of two final state leptons) or it can be provided by decays of τ leptons to neutrinos and lighter leptons.

Zb: Two leptons arise from Z decay and a third lepton may originate from a semi-leptonic b decay.

Wt: One lepton and one neutrino originate from a leptonic W decay, other leptons may originate from t decay or initial state radiation.

Z γ : Two leptons arise from a leptonic Z decay, a third may be faked by a photon. There would be a minimal amount of missing energy in these events.

$t\bar{t}$: Two leptons come from semi-leptonic decays of the top quarks. An additional lepton can enter from various processes like initial state radiation, b decay or it can be faked by a jet.

WWW: Three leptons and three neutrinos will arise from leptonic W boson decays.

Background processes that we do not consider include other tri-boson processes and $t\bar{t}$ production in association with a Z or W boson. These processes will generally have small cross sections ([97]) and must be accompanied by ISR or fake identified leptons to match the signal topology. Therefore, these background processes are not included in this analysis.

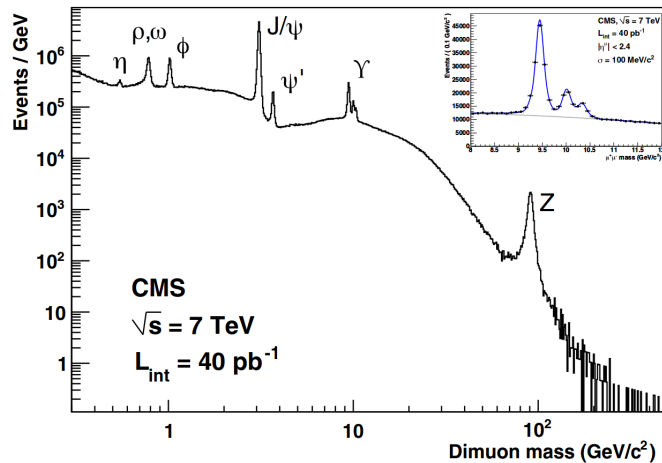


FIGURE 5.7: Invariant mass of $\mu^+\mu^-$ pair showing various resonances, with an inset of the 8 – 12 GeV region, showing three Υ peaks. To exclude the resonances, $12 \text{ GeV} < M_{l+l-} < 60 \text{ GeV}$ will be demanded. Extracted from ref. [101]

5.4 Monte Carlo generation

Since the 14 TeV data set of the LHC is non-existing, this analysis is based on generated Monte Carlo events with detector simulation. Monte Carlo generators simulate processes using theoretically calculated matrix elements. To test the Monte Carlo generator, the resulting events must eventually be compared with experimental results. Event simulation is not done in one step, but split into a number of components. The simulation starts with the hard-scattering process, which then will be showered and hadronized. After this step, the events are passed to a detector simulator to simulate the detector response. The following code is used:

- **MadGraph5 and MadEvent [102,103]:** Given any process, MadGraph identifies subprocesses and generates amplitudes, which are passed to MadEvent. MadEvent produces the hard-scattering events of the given process and produces an output in .lhe extension. The .slha file generated by SUSY-HIT can be used as an input for the particle spectrum.
- **Pythia 8.1 [104]:** The hard-scattering event produced by MadGraph is passed on to Pythia for parton showering. This process makes sure ISR and FSR is added and final state particles decay and/or hadronize.
- **Prospino 2.1 [70]:** Prospino is used to check the LO and NLO cross section of the generated signal events.
- **FastJet 3.1.3 [105]:** Jet clustering is handled by FastJet. We will use the anti- k_T algorithm with a minimal jet p_T of 20 GeV and a radius of $R = 0.4$. This algorithm introduces a distance measure between two particles (d_{ij}) and one between a particle and the beam (d_{iB}). These distances depend on $\Delta R = \sqrt{\Delta\phi^2 + \Delta\eta^2}$ and the transverse momentum. In ΔR , we use $\Delta\eta = -\Delta \log(\tan \frac{\theta}{2})$ to indicate the difference in pseudorapidity and $\Delta\phi$ to indicate the difference in the azimuth angle. For all particle pairs the distances d_{ij} and d_{iB} are calculated. Then the algorithm proceeds by finding the smallest of the distances. If this smallest distance is d_{ij} , the particles i and j are combined into a new object. If the smallest distance is d_{iB} , we call i a jet and remove it from the object list. This procedure is repeated until no objects are left in the list. If there are jets with $p_T < 20$ GeV after this procedure, these will be combined with the closest jet with $p_T > 20$ GeV.
- **Delphes 3 [106]:** The final events need to be passed on to a detector simulation. To this end, DELPHES is used. DELPHES mimics the detector response to events, taking into account measurement resolutions, efficiencies and fake particle identification rates.

Once the hard event has been generated, everything that could radiate extra particles should be modeled as well. This is all based on QCD and is process independent. QCD emission can be described via either matrix element generators or parton showers. These two mechanisms must eventually be combined without double counting. To this end we use *matching schemes*. The basic idea is that a phase-space cutoff is used to separate the regions between matrix elements and parton showers. Various schemes exist, in this analysis the MLM scheme is used [107].

The hard-scattering events generated with MadGraph5 only contain leading order (LO) contributions. The associated cross section often differs by some factor from the cross section that are calculated at next-to-leading order (NLO) in perturbation theory. This ratio is referred to as the *K-factor*. For the signal events we have chosen to calculate the *K-factor*. For the WW(1) region, the cross section given by Prospino is 4.60 pb (LO) or 6.02 pb (NLO). For WW(2) these cross sections are 13.40 pb (LO) and 17.4 pb (NLO). The branching ratio of $\text{BR}(\tilde{\chi}_{2,3}^0 \rightarrow l^+l^-\tilde{\chi}_1^0) \simeq 0.22$ and $\text{BR}(\tilde{\chi}_1^\pm \rightarrow l\nu\tilde{\chi}_1^0) \simeq 0.07$, so the expected LO cross sections for the total process are 0.07 pb for WW(1) and 0.2 pb for WW(2). With a luminosity of 300 fb^{-1} , we would expect 21252 and 61908 events respectively (before applying selection cuts). The resulting *K-factor* for the signal is ~ 1.3 . Previous studies on $3l + \cancel{E}_T$ search channels reported *K-factors* for the background processes to be of order unity [78]. We have not checked this explicitly. We choose not to include NLO effects. This will probably lead to pessimistic results, as the significance (defined in section 5.7) scales as S/\sqrt{B} . In a follow up study the effect of this choice could be investigated.

5.4.1 Expanding the signal set

So far, we only have considered the 50 best fit scenarios of the WW(1) and WW(2) regions. We want to expand these sets to contain spectra with smaller and larger mass gaps. The parameter ranges for which events are generated are given below. The main difference between WW(1) and WW(2), is that WW(1) has higgsino-like NLSPs, while WW(2) has wino-like NLSPs. These new regions are not required to fit the GC excess photon spectrum, so it is misleading to still refer to these regions as WW(1) and WW(2). Due to the NLSP's composition, we will instead refer to these regions as higgsino NLSP and wino NLSP respectively.

	wino NLSP	higgsino NLSP
M_1	50 - 200 GeV	60 - 130 GeV
M_2	50 - 200 GeV	200, 250, 300, 1000 GeV
μ	fixed	60 - 130 GeV
Additional requirements	$M_1 < M_2 < \mu$ $\Delta(M_{\tilde{\chi}_1^\pm}, M_{\tilde{\chi}_1^0}) < 60 \text{ GeV}$	$M_1 < \mu < M_2$ $\Delta(M_{\tilde{\chi}_1^\pm}, M_{\tilde{\chi}_1^0}) < 60 \text{ GeV}$

TABLE 5.2: Parameter ranges that define the wino NLSP and higgsino NLSP regions. All other parameters remain unchanged from the WW(1) and WW(2) parameter ranges. In the higgsino NLSP region, varying M_2 was done to allow for smaller mass splittings.

We want to consider all regions of parameter space that might be interesting for compressed SUSY scenarios from a particle collider point of view. Therefore, the scenarios are not required to fulfill any experimental constraints, except the LEP chargino and neutralino mass requirement. We do not expect that the results will change using these limits and it saves us a considerable amount of computing time. In appendix A, the composition of each generated scenario is shown. The higgsino NLSP region will have a $\tilde{\chi}_3^0$ that is of similar composition and mass as $\tilde{\chi}_2^0$. For this region we therefore generate $pp \rightarrow \tilde{\chi}_1^\pm \tilde{\chi}_2^0 \rightarrow l'^\pm l^+ l^- \cancel{E}_T$ and $pp \rightarrow \tilde{\chi}_1^\pm \tilde{\chi}_3^0 \rightarrow l'^\pm l^+ l^- \cancel{E}_T$.

5.5 Distinct features of signal

The considered pMSSM regions have a small mass gap between the NLSP and LSP. This means we in general expect low lepton energies. The smaller the gap, the softer the leptons will be. We show in figure 5.8(b) the transverse momentum distributions for the hardest lepton for three event sets: the irreducible WZ background, higgsino NLSP and wino NLSP. The mass gap for the higgsino NLSP and wino NLSP is set at $\Delta m = m_{\tilde{\chi}_{\text{NLSP}}} - m_{\tilde{\chi}_{\text{LSP}}} \sim 20$ GeV and the figure is normalized such that all processes have a cross section of 1 pb. This mass gap is clearly visible in the M_{l+l-} distribution (figure 5.9(a)), as M_{l+l-} is kinematically limited to exceed Δm .

We consider the same plot for higher mass gaps (figure 5.10(a)). We have chosen three benchmark mass gaps of 20 GeV, 50 GeV and 100 GeV, all within the wino NLSP region and for $m_{\tilde{\chi}_1^0} \sim 90$ GeV. We observe that the peak of the M_{l+l-} distribution shifts to higher energies when the mass gap increases. From figure 5.9(a) it is clear that for compressed scenarios, we can veto events with large M_{l+l-} (> 60 GeV). As long as $\Delta m < M_Z$, a large signal acceptance remains, while rejecting a large fraction of the background arising from on shell Z decays. We also need to introduce a lower cut on the invariant mass distribution, as the background has an accumulation of events at low invariant masses (figure 5.7). Usually this cut is set at $M_{l+l-} > 12$ GeV, and we will do the same in this analysis.

Although the LSP carries most of the energy of the NLSP, this does not necessarily mean that there is large missing transverse energy. In figure 5.9(b) we see that \cancel{E}_T is, counter-intuitively, lower than \cancel{E}_T originating from the WZ SM background process. This is due to the fact that the two LSPs are often produced back-to-back. For higher mass gaps, the average \cancel{E}_T gets higher, as can be seen in figure 5.10(b). In this case the resulting final state leptons get more energy, causing them to recoil against the LSP. This causes the LSPs to be produced less back-to-back, which results in a higher missing transverse energy.

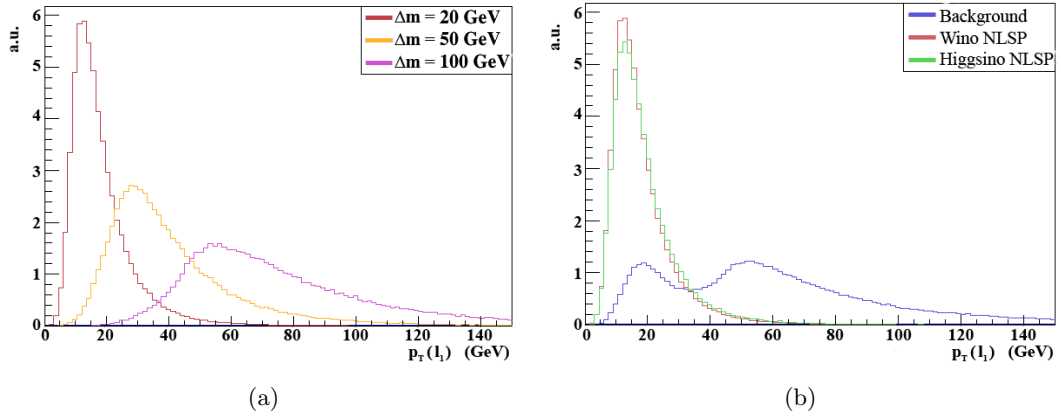


FIGURE 5.8: Transverse momentum distributions for the highest p_T lepton for *left*: $\Delta m \simeq 20$ GeV (red), $\Delta m \simeq 50$ GeV (yellow), $\Delta m \simeq 100$ GeV (purple) and *right*: WZ irreducible background (blue), wino NLSP (red), higgsino NLSP (green). Figures were made after using FastJet. The events are normalized to a cross section of 1 pb.

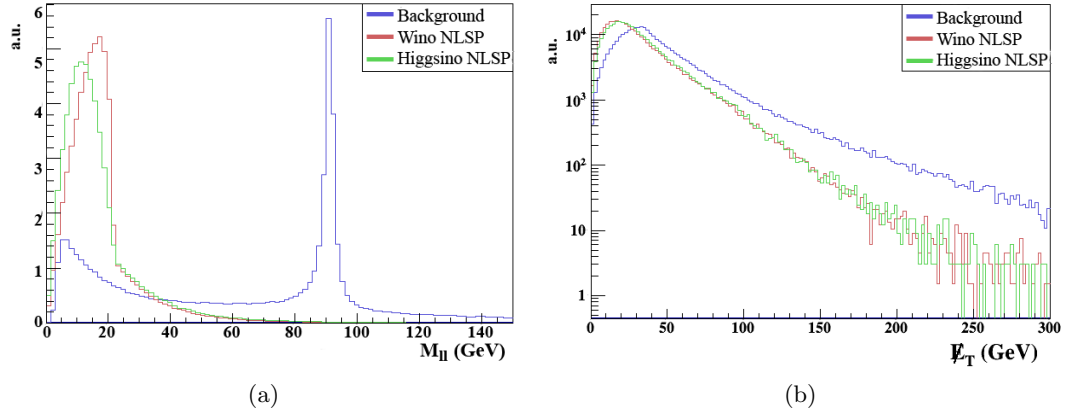


FIGURE 5.9: Distribution for M_{l+l-} (left) and E_T (right) after using FastJet. The blue curve represents the irreducible diboson (WZ) background, the red curve represents the wino NLSP scenario and the green curve the higgsino NLSP scenario. In both scenarios, $m_{\tilde{\chi}_2^0} \simeq m_{\tilde{\chi}_1^\pm} \simeq 110$ GeV, $m_{\tilde{\chi}_1^0} \simeq 90$ GeV such that $\Delta m \simeq 20$ GeV. All events are normalized to a cross section of 1 pb.

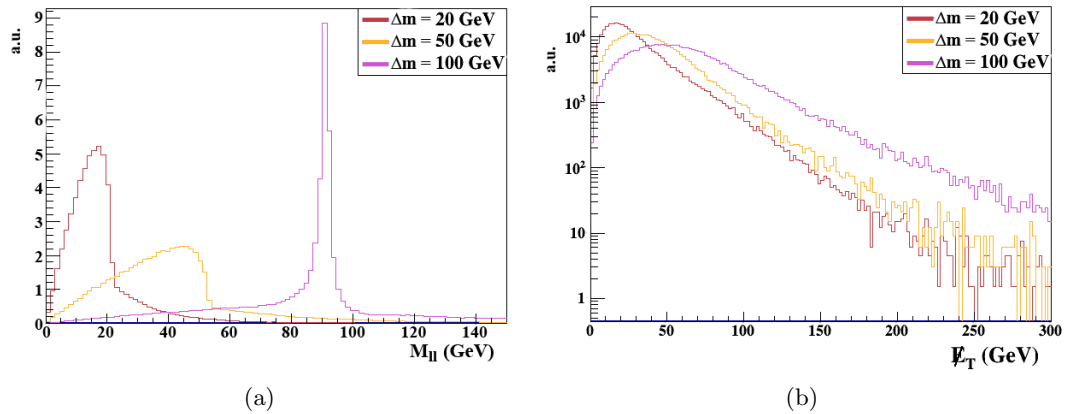


FIGURE 5.10: Distribution for M_{l+l-} (left) and E_T (right) after using FastJet. All three curves represent a wino NLSP, the red curve represents $\Delta m \simeq 20$ GeV, the yellow curve represents $\Delta m \simeq 50$ GeV and the purple curve represents $\Delta m \simeq 100$ GeV. The curves are normalized to a cross section of 1 pb.

5.5.1 Reducible backgrounds

The cross section of the reducible backgrounds will in general be higher than those from irreducible backgrounds. However, as they in general will not have the same distributions as the signal, these can be efficiently (without losing too much signal) rejected by choosing the right cuts.

To reduce the fraction of $t\bar{t}$ background, a jet veto for $p_T(j) > 50$ GeV or $p_T(j) > 30$ GeV can be introduced. The remaining significant background Zb can be efficiently rejected by a requirement on $M_{l+l^-} < 60$ GeV, as shown in figure 5.11(a).

The transverse momentum of the highest p_T lepton ($p_T(l_1)$) will be smaller for the signal than for the background, as shown in figure 5.12(a). We therefore can also reject events with high $p_T(l)$ to significantly reduce the number of background events.

As can be seen in figure 5.11(b), the missing transverse energy of the reducible backgrounds will, for most backgrounds, be larger than the missing transverse energy of the signal. After demanding exactly three final state leptons and at least one OSSF lepton pair, we observed that \cancel{E}_T and $p_T(l_W)$ (transverse momentum from the lepton originating from W -decay) are correlated in a funnel-like shape (figure 5.13(a)). The signal events are at low $p_T(l_W)$ and \cancel{E}_T , while background events have higher \cancel{E}_T or $p_T(l_W)$ (or both). We will use this feature to discriminate signal from background.

In the rest frame of a particle decaying in two other particles, the decay particles will be produced back-to-back. We therefore expect that the background distribution for $\Delta\phi(\cancel{E}_T, l_W)$ is peaked towards $\Delta\phi = \pi$ for any events containing \cancel{E}_T and l_W originating from a W boson decay. If we then allow for a boost of the W bosons, the distribution will get smeared out to other values as well, although a small peak at $\Delta\phi = \pi$ remains. We do not expect the same topology for the signal events. This is because the \cancel{E}_T will now be the sum of three components: two LSPs and a neutrino. We expect that $\Delta\phi(\cancel{E}_T, l_W)$ is uniformly distributed for the signal events. This is also observed in the generated events, as shown in figure 5.13(b). This means we can also use this variable to distinguish signal and background events.

To conclude, we now have 5 observables that we can use to discriminate signal from background:

$$M(l^+l^-), \quad p_T(l), \quad p_T(j), \quad \cancel{E}_T \text{ vs } p_T(l_W), \quad \Delta\phi(\cancel{E}_T, l_W).$$

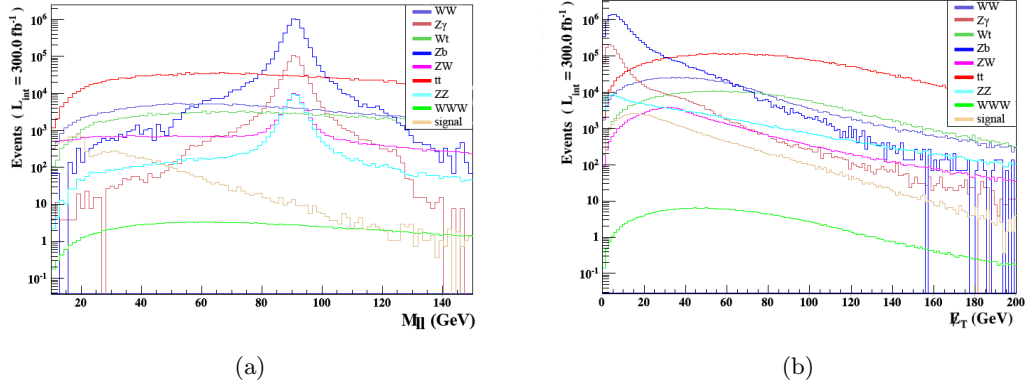


FIGURE 5.11: Distribution for M_{l+l-} (left) and \cancel{E}_T (right) after DELPHES detector simulation and before imposing any cuts. Shown are all reducible and irreducible background distributions, as well as the distributions we would expect for a $\Delta m = 20$ GeV wino NLSP with $m_{\tilde{\chi}_1^0} \sim 100$ GeV.

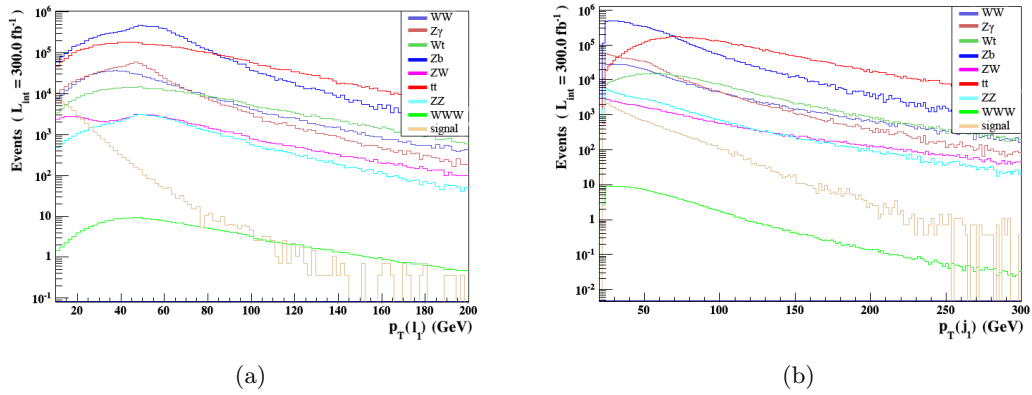


FIGURE 5.12: Distribution for $p_T(l_1)$ (left) and $p_T(j_1)$ (right) after DELPHES detector simulation and before imposing any cuts. Shown are all reducible and irreducible background distributions, as well as the distributions we would expect for a $\Delta m = 20$ GeV wino NLSP with $m_{\tilde{\chi}_1^0} \sim 100$ GeV.

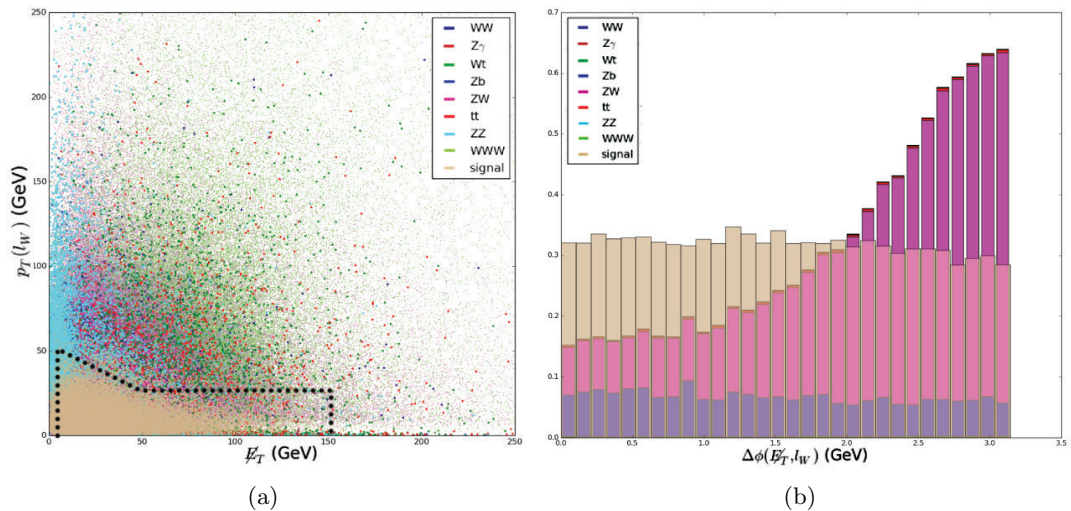


FIGURE 5.13: Left: Scatter plot of \cancel{E}_T against $p_T(l_W)$. The dotted black line indicates the *funnel cut* (defined in section 5.6.3). Right: Distribution for $\Delta\phi(\cancel{E}_T, l_W)$. Both figures are made after demanding exactly 3 leptons and at least one OSSF lepton pair. In the histogram, the number of events are weighted by their cross section and the histogram is normalized to 1 (for background and signal separately). We show the distributions we would expect for a $\Delta m = 20$ GeV wino NLSP with $m_{\tilde{\chi}_1^0} \sim 100$ GeV.

5.6 Signal selection criteria

5.6.1 Lepton efficiencies

As discussed in the previous section, we want to use as low- p_T leptons as possible. Eventually, we will run into problems, as the lepton identification gets more difficult at lower energies. We will use the p_T -dependent identification efficiencies implemented in DELPHES. For clarity, these are given in table 5.3.

	e	μ
$p_T(l) < 0.1$ GeV	0	0
$ \eta(l) \leq 1.5$, $0.1 < p_T(l) < 1$ GeV	0.73	0.75
$ \eta(l) \leq 1.5$, $1 < p_T(l) < 10$ GeV	0.95	0.99
$ \eta(l) \leq 1.5$, $p_T(l) > 10$ GeV	0.99	0.99
$1.5 < \eta(l) \leq 2.5$, $0.1 < p_T(l) < 1$ GeV	0.50	0.70
$1.5 < \eta(l) \leq 2.5$, $1 < p_T(l) < 10$ GeV	0.83	0.98
$1.5 < \eta(l) \leq 2.5$, $p_T(l) > 10$ GeV	0.90	0.98
$ \eta(l) > 2.5$	0	0

TABLE 5.3: Lepton identification efficiencies.

Taking into account these reduced efficiencies at low lepton p_T , we will select leptons only if the two highest p_T leptons have $p_T(l_1, l_2) > 10$ GeV (electrons) or $p_T(l_1, l_2) > 5$ GeV (muons) and $|\eta(l)| < 2.5$. Being able to use even lower p_T leptons will most likely enhance the sensitivity, but this is probably difficult to realize. The rate at which the LHC produces events is much higher than the rate that ATLAS is able to save events. To cope with this, a rejection of mostly uninteresting events is needed, while keeping a high efficiency for events that have a high chance of being interesting. At ATLAS, this is realized in the form of a *trigger* system. In the first stage of this procedure (L1), the trigger uses a limited amount of detector information to make a decision in less than 2.5 μ s (bunch-spacing). ATLAS can trigger on lepton p_T , photon p_T , jets, τ leptons that decay hadronically, and large \cancel{E}_T . ATLAS selects events with higher p_T leptons and \cancel{E}_T than we think are interesting for our analysis. For comparison, we will use the ATLAS di-lepton and tri-lepton L1 trigger requirements as a lepton p_T cut as well. These cuts are:

- μ : $p_T(\mu_1) > 10$ GeV and $p_T(\mu_2) > 10$ GeV, or $p_T(\mu_1) > 18$ GeV and $p_T(\mu_2) > 4$ GeV
- e : $p_T(e_1) > 10$ GeV and $p_T(e_2) > 10$ GeV, or $p_T(e_1) > 18$ GeV and $p_T(e_2) > 7$ GeV
- mixed: $p_T(e) > 7$ GeV and $p_T(\mu) > 6$ GeV (exactly 3 leptons required)

We will refer to this set of cuts as *ATLAS trigger cuts* from now on.

5.6.2 Selection of the OSSF lepton pair

First we will demand at least three leptons in the final state. After this, we will require an OSSF lepton pair. The identification of this pair is complicated if there are 3 leptons of the same flavor, as more than one OSSF lepton pair can be formed in that case. To select the *right* (the one originating from on- or off-shell Z boson decay) lepton pair, different approaches can be adopted:

- The lepton pair with M_{l+l-} closest to M_Z is taken.
- The lepton pair with minimal distance in $\Delta R = \sqrt{\Delta\phi^2 + \Delta\eta^2}$ is taken.
- The lepton pair with the highest p_T (per lepton) is taken.
- The lepton pair with the smallest M_{l+l-} is taken.

ATLAS selects the OSSF lepton pair as the pair with M_{l+l-} closest to M_Z . This means that the M_{l+l-} mass distribution will be biased towards the Z mass, which may be less useful if we are trying to extract mass information. In table 5.4 we evaluate the error made if we adopt each of the four different approaches. We can observe that no algorithm is perfect. We will pick the lepton pair with minimal distance in ΔR , as this algorithm has the best overall performance for the events we are most interested in ($\Delta m = 20$ GeV and WZ background).

Algorithm	$\Delta m = 20$ GeV	$\Delta m = 50$ GeV	$\Delta m = 100$ GeV	WZ background
$\min_{i,j} M_{l_i,l_j} - M_Z $	0.62	0.53	0.04	0.15
$\min_{i,j} \Delta R(l_i, l_j)$	0.34	0.40	0.47	0.35
$\max_{i,j} (P_T(l_i), P_T(l_j))$	0.46	0.49	0.49	0.39
$\min_{i,j} M_{l_i,l_j}$	0.38	0.42	0.48	0.35

TABLE 5.4: Fraction of events in which the OSSF lepton pair was selected incorrectly for each of the four algorithms and in four data sets.

5.6.3 Final selection cuts

Based on the features as discussed in the previous two paragraphs, we will use the following cuts to optimize the analysis:

- $N(l) = 3$
- $N(l^+l^-) > 0$ (at least one OSSF lepton pair)
- $5 \text{ GeV} < p_T(\mu) < 50 \text{ GeV}$ and $10 \text{ GeV} < p_T(e) < 50 \text{ GeV}$ *or* ATLAS trigger cuts.
- $12 \text{ GeV} < M(l^+l^-) < 60 \text{ GeV}$
- $p_T(j_1) < 50 \text{ GeV}$
- *Funnel cut*: $5 \text{ GeV} < \cancel{E}_T < 150 \text{ GeV}$ **and**
 - * if $\cancel{E}_T < 50 \text{ GeV}$: $p_T(l_W) + \frac{3}{5}\cancel{E}_T < 50 \text{ GeV}$
 - * else: $p_T(l_W) < 20 \text{ GeV}$
- $\Delta\phi(\cancel{E}_T, l_W) < 2$
- Optional: $p_T(j_1) < 30 \text{ GeV}$

These cuts are optimal for small mass gap scenarios ($\Delta(m_{\tilde{\chi}_1^\pm}, m_{\tilde{\chi}_1^0}) \sim (10 - 50) \text{ GeV}$). However, when one looks at larger mass gaps, it may be better to use other cuts. In table 5.5 we show the resulting *cut-flow diagram*. This diagram shows how many events are left after each consecutive cut. We include the cut-flow diagram for all the background processes and for three wino NLSP processes (with $\Delta m = 20 \text{ GeV}$, 50 GeV and 100 GeV) and for one higgsino NLSP process with $\Delta m = 20 \text{ GeV}$. We assume a luminosity of 300 fb^{-1} to calculate the expected number of events.

	WZ	WW	ZZ	Zb	Wt	Z γ	t \bar{t}	WWW
Generated events	132705	1244002	248389	13606295	716358	1453092	8736325	402
$N(l) = 3$	60357	3450	5099	415519	16970	4442	83556	120
$N(l^+l^-) > 0$	60300	3439	5095	413974	16933	4431	83118	120
5 GeV < $p_T(\mu) < 50$ GeV and 10 GeV < $p_T(e) < 50$ GeV	19323	1470	863	139715	4349	1987	22816	23
12 GeV < $M(l^+l^-) < 60$ GeV	8573	711	195	25592	2528	233	12218	13
$p_T(j) < 50$ GeV	7638	599	136	23039	974	218	2496	12
Funnel cut	5067	426	35	10881	572	61	1269	4
$\Delta\phi(\cancel{E}_T, l_W) < 2$	3327	354	8	2955	467	7	1051	1
Optional $p_T(j_1) < 30$ GeV	2979	278	5	1343	176	7	306	1
Total background after cuts:								8170 (5095)

TABLE 5.5: Expected number of background events after each consecutive cut at 300 fb⁻¹ for background processes. Statistical uncertainties are not included here, but is usually of the order of 10%. The total expected number of background events is indicated in the last row, the total expected number of background events including the optional jet p_T cut is in parentheses.

	Wino $\Delta m=20$ GeV	Wino $\Delta m=50$ GeV	Wino $\Delta m=100$ GeV	Higgsino $\Delta m=20$ GeV
Generated events	71700	87600	22380	23790
$N(l) = 3$	17819	24613	7826	5407
$N(l^+l^-) > 0$	17792	24576	7818	5399
5 GeV < $p_T(\mu) < 50$ GeV and 10 GeV < $p_T(e) < 50$ GeV	12365	17228	971	3889
12 GeV < $M(l^+l^-) < 60$ GeV	10018	16597	219	2661
$p_T(j) < 50$ GeV	8626	14725	187	2310
Funnel cut	7983	10964	41	2128
$\Delta\phi(\cancel{E}_T, l_W) < 2$	5424	6624	26	1397
Optional $p_T(j_1) < 30$ GeV	4516	5650	19	1166

TABLE 5.6: Expected number of signal events after each consecutive cut at 300 fb⁻¹ for four scenarios: wino-like NLSP with different mass gaps (20, 50 and 100 GeV), and higgsino-like NLSP with a 20 GeV mass gap.

5.7 Results

To evaluate the sensitivity, we will use as a measure the number of standard deviations of the normal distributions (that is referred to as the Z_N -value). We will first calculate the p -value, using a Poisson probability convoluted with a normal distribution and a systematic background error of $\sigma = 10\%$. Let μ denote the expected number of Standard Model (background) events, σ the systematic error on this number and λ the expected number of events including the SUSY prediction. The p -value for observing λ events is then proportional to:

$$p = p(\lambda|\mu, \sigma) \propto \int_{\mu-7\sigma}^{\mu+7\sigma} \left(\int_{-10}^{\frac{x-\lambda}{\sqrt{x}}} \exp^{-2t^2} dt \right) \frac{1}{\sqrt{\sigma}} e^{-\frac{1}{2} \left(\frac{x-\mu}{\sigma} \right)^2} dx. \quad (5.1)$$

After the p -value is calculated, this value is translated into a Z_N -value via the inverse complementary error function:

$$Z_N \equiv \sqrt{2}\Phi^{-1}(1 - 2p) \quad ; \quad \Phi(1 - 2p) \equiv \frac{2}{\sqrt{\pi}} \int_{1-2p}^{\infty} e^{-t^2} dt. \quad (5.2)$$

We will refer to the Z_N -value as the significance. More details can be found in ref. [108]. In our case, this value indicates the number of standard deviations a pMSSM model differs from the Standard Model. A high value for Z_N means that the considered pMSSM model is probably not consistent with the SM. Usually, discovery is claimed when the significance exceeds 5σ , while a pMSSM model can be excluded if it is not found in a region where you would have expected to see a 2σ deviation from the SM.

In figure 5.14 we present the significance as a color code for the wino NLSP and higgsino NLSP case. This figure is made for the LHC 14 TeV with 300 fb^{-1} . The stars indicate the GC regions WW(2) and WW(1). The dotted red line indicates the ATLAS limit obtained for simplified SUSY models, where the NLSPs are 100% wino and the relevant branching ratios are set to 100%. We observe that the significance falls off with higher chargino and neutralino masses. This is due to the reduced cross section for higher chargino and neutralino masses (figure ??). The significance also falls off at higher mass gaps. This is due to the invariant mass cut we imposed. It suggests that another search strategy if one wants to be sensitive to less compressed scenarios. Since the higgsino NLSP production cross section is smaller than the wino NLSP production cross section, the significance does not exceed 6σ even in the most optimistic cases. The inclusion of NLO effects might enhance the significance. We find that the 14 TeV LHC can probe LSP masses up to 140 GeV for mass gaps between $\sim 9 - 50$ GeV if the NLSPs are wino-like (figure 5.14(a)).

We find that even with 30 fb^{-1} we can be sensitive to compressed SUSY scenarios, as LSP masses up to 140 GeV can be probed for mass gaps between $\sim 10 - 50$ GeV (appendix B, figure B.1). We observe that the significance does not improve much if we collect more data. This is due to the fact that the systematic error remains the same. If we are able to reduce the systematic background error to 5% (appendix B, figure B.2), the significance would be greatly enhanced. In this case, exclusion limits for LSP masses > 170 GeV with mass gaps $\gtrsim 6$ GeV can be realized for the wino NLSP models. The higgsino NLSP region can also be probed successfully if we are able to reduce the

systematic error, and could result in exclusion limits for LSP masses up to 110 GeV and mass gaps of $\gtrsim 15$ GeV.

The lepton p_T requirements we imposed are lower than the current ATLAS triggers on lepton p_T . The significance using the ATLAS trigger cuts as a lepton p_T cut and assuming a 10% background systematic error at 300 fb^{-1} is shown in figure B.3 (appendix B). The significance is somewhat reduced compared to the significance using our own lepton p_T cuts. Using the ATLAS trigger cuts, we can exclude LSP masses up to 135 GeV and $\Delta m > 10$ GeV. If we reduce the lepton p_T requirement to > 1 GeV (appendix B, figure B.4) the significance is marginally increased: LSP masses up to 145 GeV and $\Delta m > 7$ GeV can be excluded. Being able to trigger on softer leptons will therefore enhance the sensitivity somewhat for small mass gaps.

Using the proposed search strategy with 10% background uncertainty, the sensitivity would be greatly enhanced compared to the standard LHC searches. A comparison is given in figure 5.15 for the ATLAS and CMS reach for wino and higgsino NLSP regions using their current tri-lepton searches (as indicated in table 5.1). We observe that the sensitivity for ATLAS and CMS increases for bigger mass gaps. For ATLAS the sensitivity reaches $> 2\sigma$ for mass gaps > 30 GeV and LSP masses < 100 GeV. Note that this does not exactly resemble the ATLAS limit indicated by the dotted red line in figure 5.6. This is because, in contrast with ATLAS, we do not use simplified models, which reduces the chargino-neutralino production cross section by a factor of ~ 1.15 .

5.7.1 Discussion

Two global fit studies performed in the pMSSM (see ref. [109–111]) and the Galactic Center photon excess pMSSM explanation independently suggest that compressed supersymmetric spectra with a ~ 100 GeV bino-like dark matter particle might be realized in nature. These massive slepton and squark compressed SUSY scenarios have implications on the LHC SUSY search strategy. We cannot rely on high jet p_T or \cancel{E}_T triggers for the discovery of the compressed SUSY scenarios, while these triggers are often invoked in SUSY searches. A new search strategy is needed in order to probe compressed SUSY scenarios successfully. In figure 5.16 we show the 2σ exclusion reach obtained for several proposed cuts for the wino NLSP (a) and the higgsino NLSP (b) models. These limits are made for the LHC operating at $\sqrt{s} = 14$ TeV and using 300 fb^{-1} of data. Being able to use lower requirements on the lepton transverse momenta will result in a somewhat higher sensitivity for small mass gaps and higher LSP and NLSP masses. However, even with the current ATLAS trigger requirements on the lepton transverse momenta, we are able to get more sensitive to compressed SUSY scenarios than ATLAS and CMS are now. This is because of the combined effects of the funnel cut and the invariant mass cut. The first cut makes use of the difference between the signal and background topology. Contrary to the standard intuition, the considered signal events result in a relatively low missing transverse energy when compared to the SM background events, because the LSPs are often produced back-to-back. The funnel cut takes this effect into account. The invariant mass cut allows us to remove background events with resonances originating from on-shell Z decays. Figure 5.16 shows that if we are able to reduce the systematic background error, the exclusion reach can be improved tremendously.

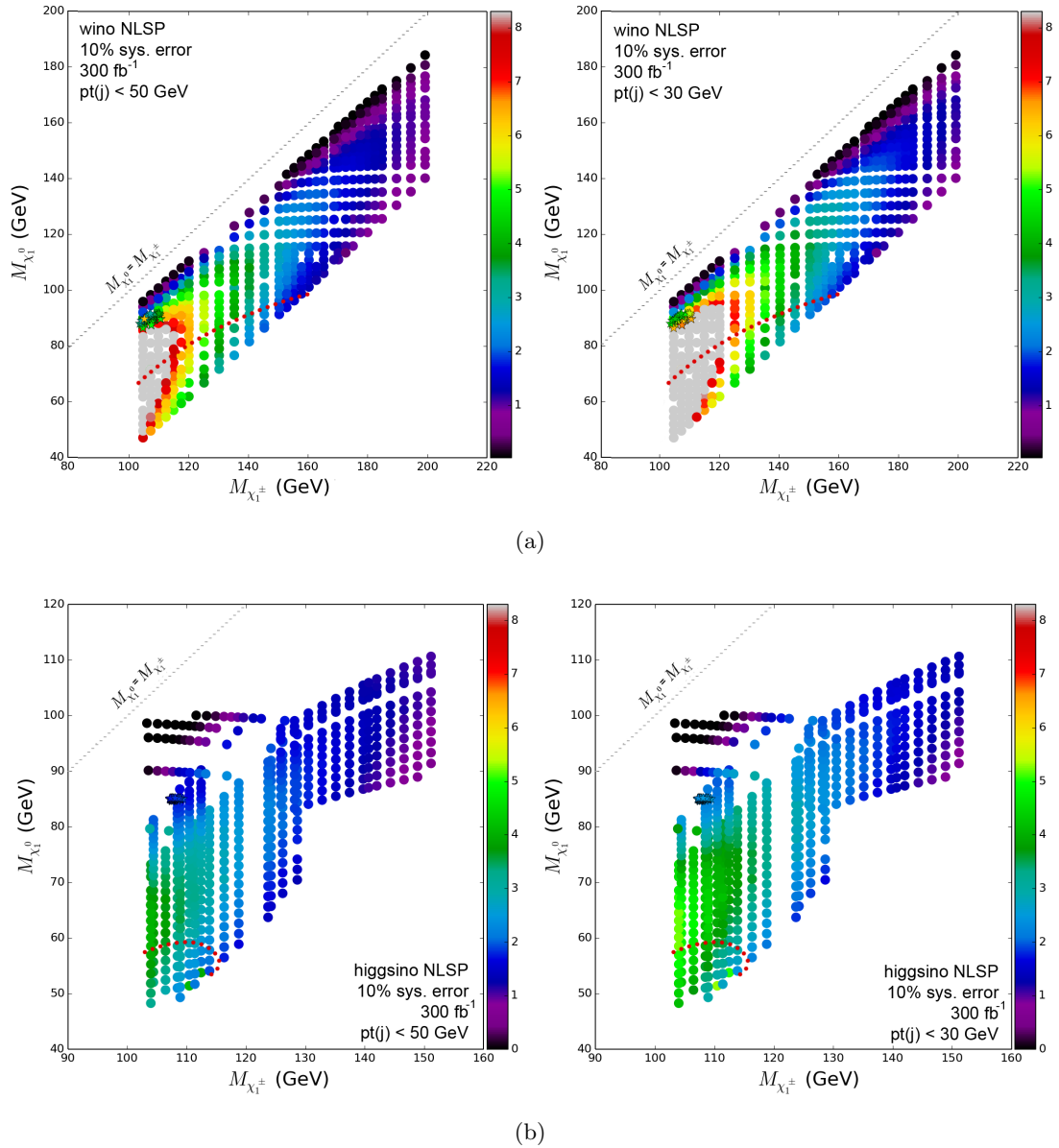


FIGURE 5.14: Sensitivity for *left*: $p_T(j) < 50$ GeV and *right*: $p_T(j) < 30$ GeV cut for wino NLSP (a) and higgsino NLSP (b) assuming a background systematic uncertainty of 10%. The stars indicate the GC regions WW(2) (a) and WW(1) (b). The dashed gray line indicates the limit $m_{\tilde{\chi}_1^0} = m_{\tilde{\chi}_1^\pm}$. The dotted red line indicates the ATLAS limit obtained for the wino NLSP (a) and the higgsino NLSP (b) models.

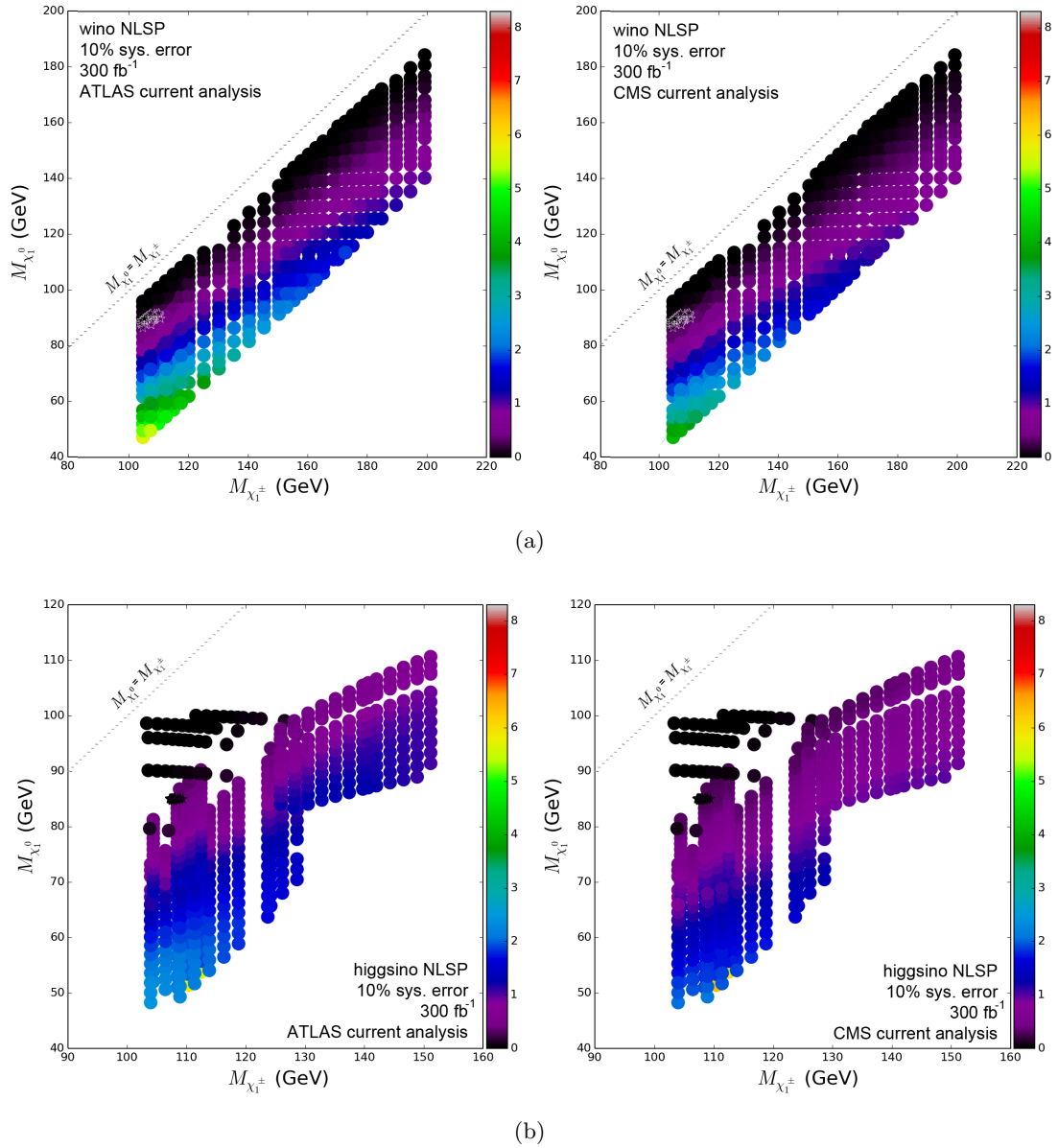


FIGURE 5.15: Standard ATLAS and CMS tri-lepton searches sensitivity for wino NLSP (a) and higgsino NLSP (b). The stars indicate the GC regions WW(2) (a) and WW(1) (b). Note that the significance is somewhat lower than for the simplified SUSY models. This is due to the cross section for our models in comparison with the simplified SUSY models.

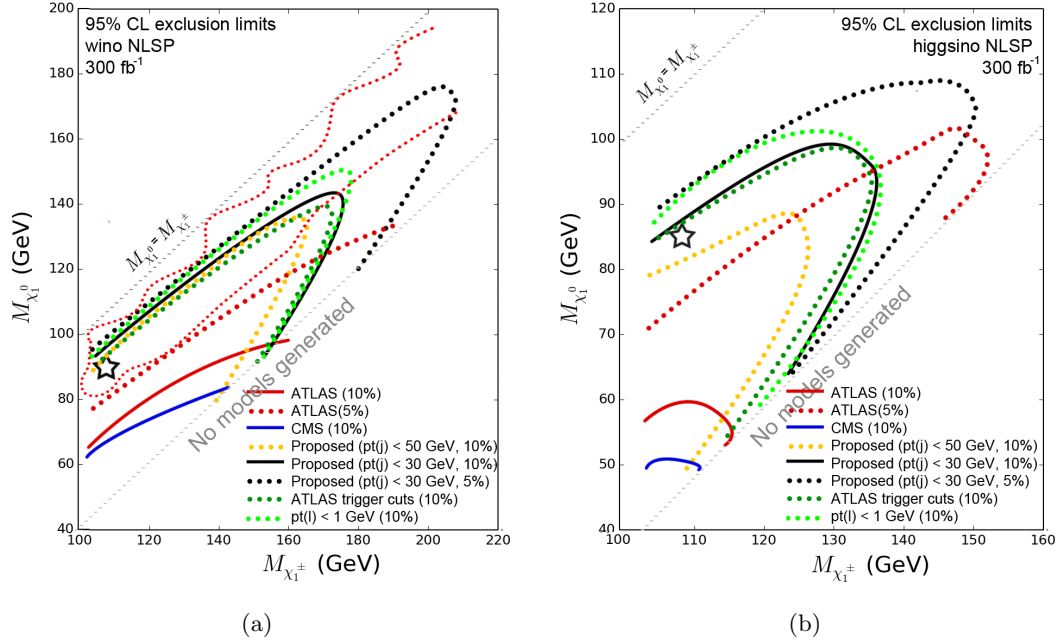


FIGURE 5.16: The expected 2σ exclusion reach for the LHC at 14 TeV and with 300 fb^{-1} of data for the wino NLSP (a) and higgsino NLSP (b) models. The current CMS and ATLAS reach is indicated by the blue and red solid (dotted) line, using a systematic background uncertainty of 10% (5%). The solid (dotted) black line indicate the limit obtained using the default lepton transverse momentum cuts with the requirement $p_T(j) < 30 \text{ GeV}$, using a background uncertainty of 10% (5%). The yellow dotted line indicates the limit using these same cuts and $p_T(j) < 50 \text{ GeV}$. The light and dark green dotted lines indicate the reach for other possible lepton transverse momentum cuts ($p_T(l) > 1 \text{ GeV}$ and the ATLAS trigger cuts respectively). The stars indicate the GC best fit pMSSM models WW(1) (a) and WW(2) (b), which coincide with the best global fit models obtained by [111]. The finely dotted red line indicates the 1σ contour of the most likely pMSSM10 models from ref. [110] (only for wino NLSP).

Conclusion

I spy with my little eye...

A systematic search for dark matter annihilation in the Galactic Center (GC) resulted in three regions of pMSSM parameter space that explain the observed excess of γ -rays. These regions are not excluded by any limits on dark matter or supersymmetry. Furthermore, these models predict a similar value for the dark matter relic density as is reported by the Planck satellite.

The regions found to explain the Galactic Center excess as measured by the Fermi satellite, are also consistent with a small excess reported in the dwarf galaxy Reticulum II. The resulting J -factor, obtained by fitting the pMSSM GC regions to the Reticulum II photon spectrum, is $(20.3 - 20.5)_{-0.3}^{+0.2} \text{ GeV}^2 \text{ cm}^{-5}$, which is consistent with J -factor determinations based on other methods for this dwarf galaxy. These results are published in the Journal of Cosmology and Astrophysics [112]. At the time of writing, eight ultra-faint dwarf galaxies have been discovered. One of these galaxies, Tuc III, is of particular interest, as it shows a small excess of γ -rays. Tuc III's J -factor is estimated to be of similar size as Reticulum II's and its photon spectrum resembles the one of Reticulum II and the Galactic Center.

Furthermore, Fermi published an extensive background analysis on the Galactic Center. They reported that, after the subtraction of all known background and accounting for an unknown component, a small residue of γ -rays is still unaccounted for. The peak of the γ -ray excess photon spectrum has shifted to somewhat higher energies, which means that the proposed GC solutions probably will result in a better fit. Work is in progress to perform a combined fit to dwarf galaxies and the Galactic Center.

In two of the three pMSSM GC regions, the lightest neutralino (that is considered the lightest supersymmetric particle or LSP) is bino-like and the next to lightest neutralinos and charginos (NLSP) are wino or higgsino-like and near-degenerate in mass. The regions are characterized by a small mass gap between the LSP and NLSP. Motivated by these GC regions, we probe the LHC sensitivities for these regions of pMSSM parameter space. In particular, we focus on the tri-lepton plus missing transverse energy ($3l + \cancel{E}_T$) final state arising from WZ -mediated leptonic chargino and neutralino decays. Standard ATLAS and CMS $3l + \cancel{E}_T$ searches fail when the mass gap between the LSP and NLSPs becomes too small. Often these searches are focused on large missing transverse energy. We find, however, that LSPs are often produced back to back in small mass gap pMSSM scenarios, resulting in a relatively low missing transverse energy! We therefore propose a soft lepton and low missing transverse energy SUSY search. We note that it might be difficult to record events with low lepton p_T , as lepton identification becomes less efficient for lower transverse momenta. In addition, triggering on very soft leptons

and low missing transverse energy may be problematic for ATLAS and CMS. To probe the sensitivity for the 14 TeV LHC with 300 fb^{-1} luminosity with a 10% systematic error, we use pMSSM models inspired by the GC regions WW(1) and WW(2). The main irreducible background for this search channel is the production of WZ decaying leptonically. The main reducible backgrounds are $t\bar{t}$ and Zb .

One particularly useful variable to distinguish signal from background is the invariant mass of the lepton pair originating from $\tilde{\chi}_2^0$ decay. Vetoing events with large M_{l+l-} can increase the sensitivity, because signal events peak around $\Delta m = m_{\tilde{\chi}_{\text{NLSP}}} - m_{\tilde{\chi}_{\text{LSP}}}$, while background events where these two leptons originate from Z -boson decay peak at m_Z . Additionally, a *funnel cut* ($\cancel{E}_T > 5 \text{ GeV}$ and if $\cancel{E}_T < 50 \text{ GeV}$: $p_T(l_W) + \frac{3}{5}\cancel{E}_T < 50 \text{ GeV}$, else $p_T(l_W) < 20 \text{ GeV}$) and a cut on $\Delta\phi(\cancel{E}_T, l_W) < 2$ have been introduced to enhance the sensitivity. Jets with $p_T > 50 \text{ GeV}$ or $p_T > 30 \text{ GeV}$ are vetoed to reduce the $t\bar{t}$ background.

We find that pMSSM models in the wino NLSP region can be excluded for LSP masses up to 140 GeV and mass gaps as low as 9 GeV if we assume a 10% systematic error. For higher masses and the higgsino NLSP region, the production cross section is the limiting factor. If we are able to reduce the systematic error to 5%, exclusion limits for LSP masses $> 170 \text{ GeV}$ with mass gaps $\gtrsim 6 \text{ GeV}$ can be realized. The higgsino NLSP scenarios can be probed for LSP masses up to 110 GeV and mass gaps of $\gtrsim 15 \text{ GeV}$. Being able to use lepton transverse momenta lower than 5 GeV for muons and 10 GeV for electrons would also increase the sensitivity a little bit, allowing us to probe wino NLSP models with $\Delta m \gtrsim 7 \text{ GeV}$.

To come to this conclusion, the introduction of the funnel cut and the invariant mass cut played a significant role. We therefore propose an updated tri-lepton search strategy, and stress the importance of a search for signs of supersymmetry resulting from events containing low missing transverse energy, contrary to what might be intuitive. If we are able to lower the trigger p_T requirements for the leptons, this would also be worth to pursue, although to a lesser extent. Being able to use lower lepton transverse momenta would increase the sensitivity, allowing us to probe $\sim 2 \text{ GeV}$ smaller mass gaps and $\sim 10 \text{ GeV}$ higher LSP masses as compared to the standard lepton transverse momentum trigger requirements.

We stress the importance of these pMSSM models with a $\sim 100 \text{ GeV}$ bino-like DM particle. Three independent studies (two global fit studies and the GC photon excess pMSSM explanation) suggest that these models might be realized in nature [51, 109–111], but the LHC experiments are not sensitive for these models using their current electroweak supersymmetry search strategy! An updated search strategy is therefore needed, and could be implemented in the way as presented in this thesis. These results are prepared to be published in the Journal of High Energy Physics (ref. [113]).

Appendix A

Composition model points

These figures present the bino, wino and higgsino compositions of the neutralinos and charginos of the SUSY model points used in chapter 5.

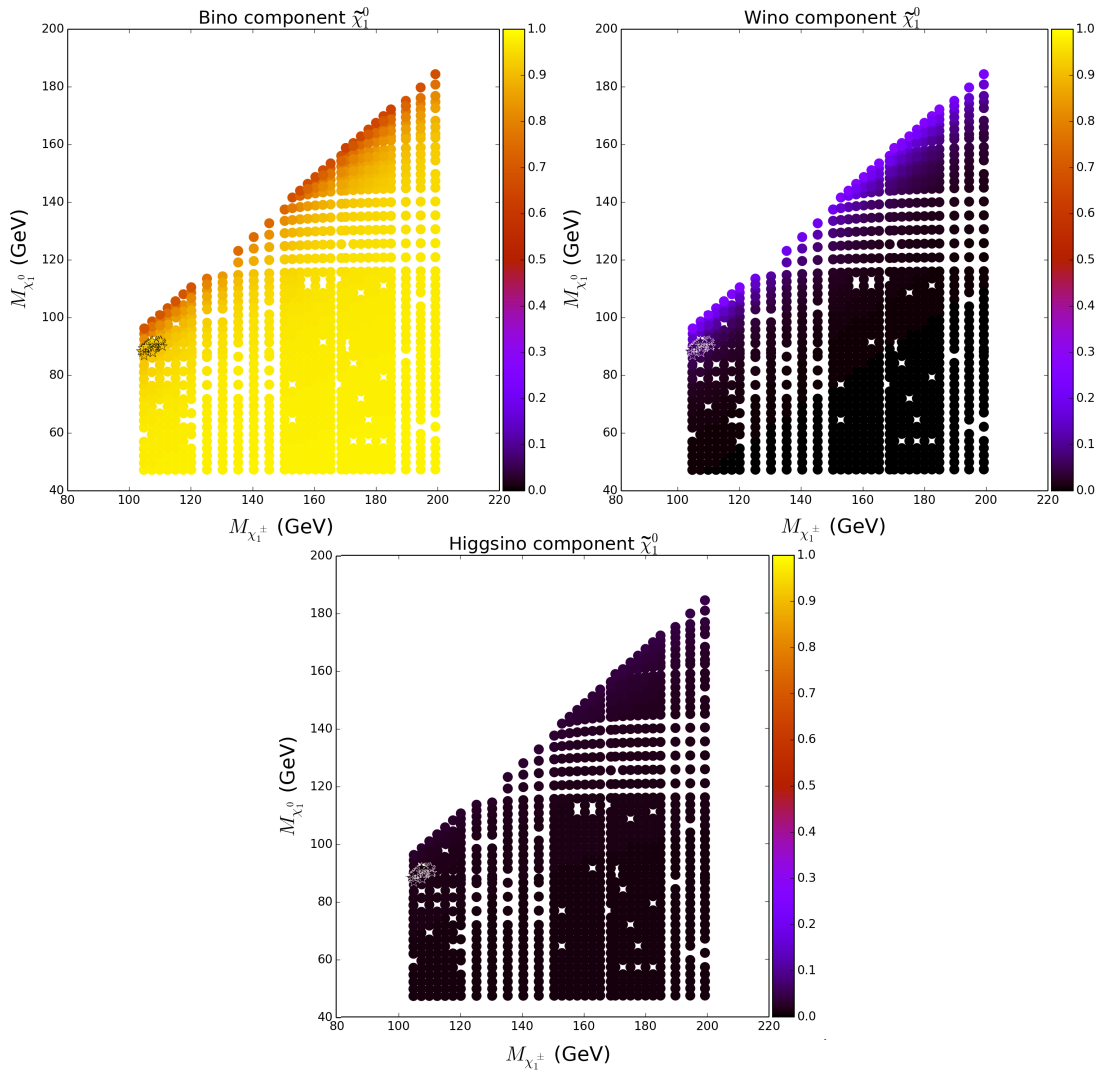


FIGURE A.1: Wino NLSP: Mass of $\tilde{\chi}_1^0$ as function of $m_{\tilde{\chi}_{1,\pm}}$ with bino, wino and higgsino composition of $\tilde{\chi}_1^0$ as color code. The stars indicate the WW(2) GC region.

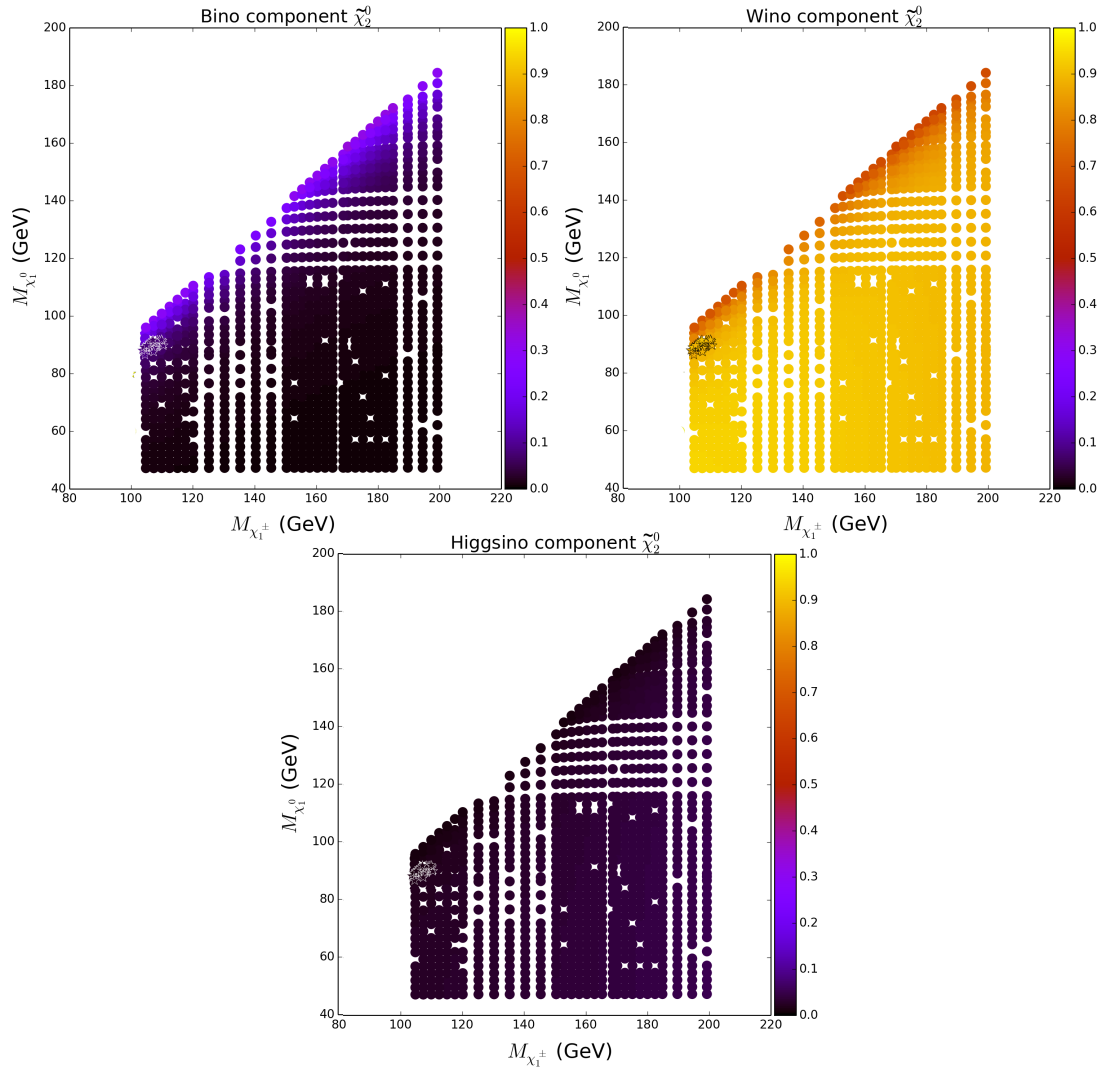


FIGURE A.2: Wino NLSP: Mass of $\tilde{\chi}_1^0$ as function of $m_{\tilde{\chi}_1^\pm}$ with bino, wino and higgsino composition of $\tilde{\chi}_2^0$ as color code. The stars indicate the WW(2) GC region.

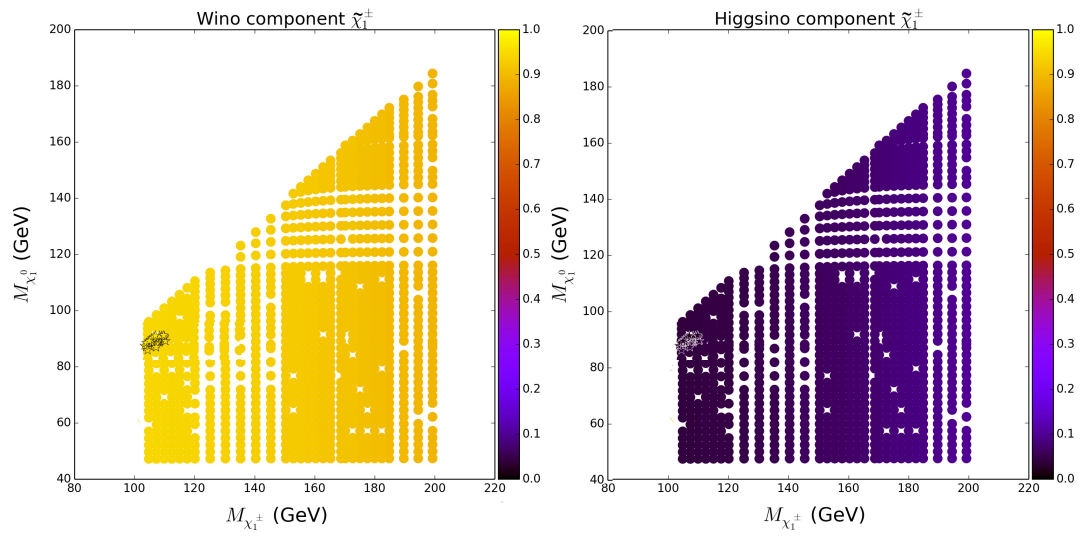


FIGURE A.3: Wino NLSP: Mass of $\tilde{\chi}_1^0$ as function of $m_{\tilde{\chi}_1^\pm}$ with wino and higgsino composition of $\tilde{\chi}_1^\pm$ as color code. The stars indicate the WW(2) GC region.

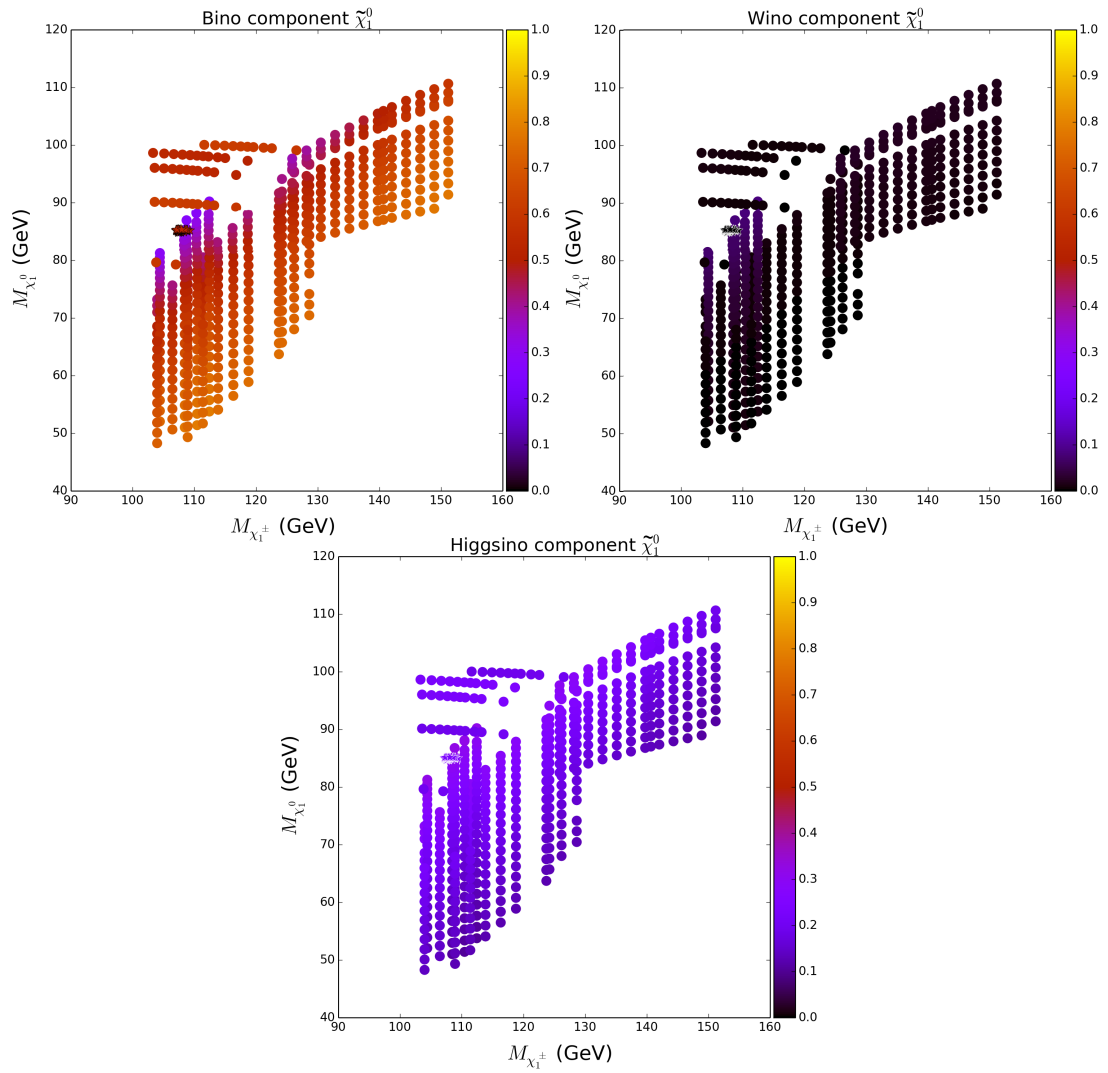


FIGURE A.4: Higgsino NLSP: Mass of $\tilde{\chi}_1^0$ as function of $m_{\tilde{\chi}_{1\pm}}$ with bino, wino and higgsino composition of $\tilde{\chi}_1^0$ as color code. The stars indicate the WW(1) GC region.

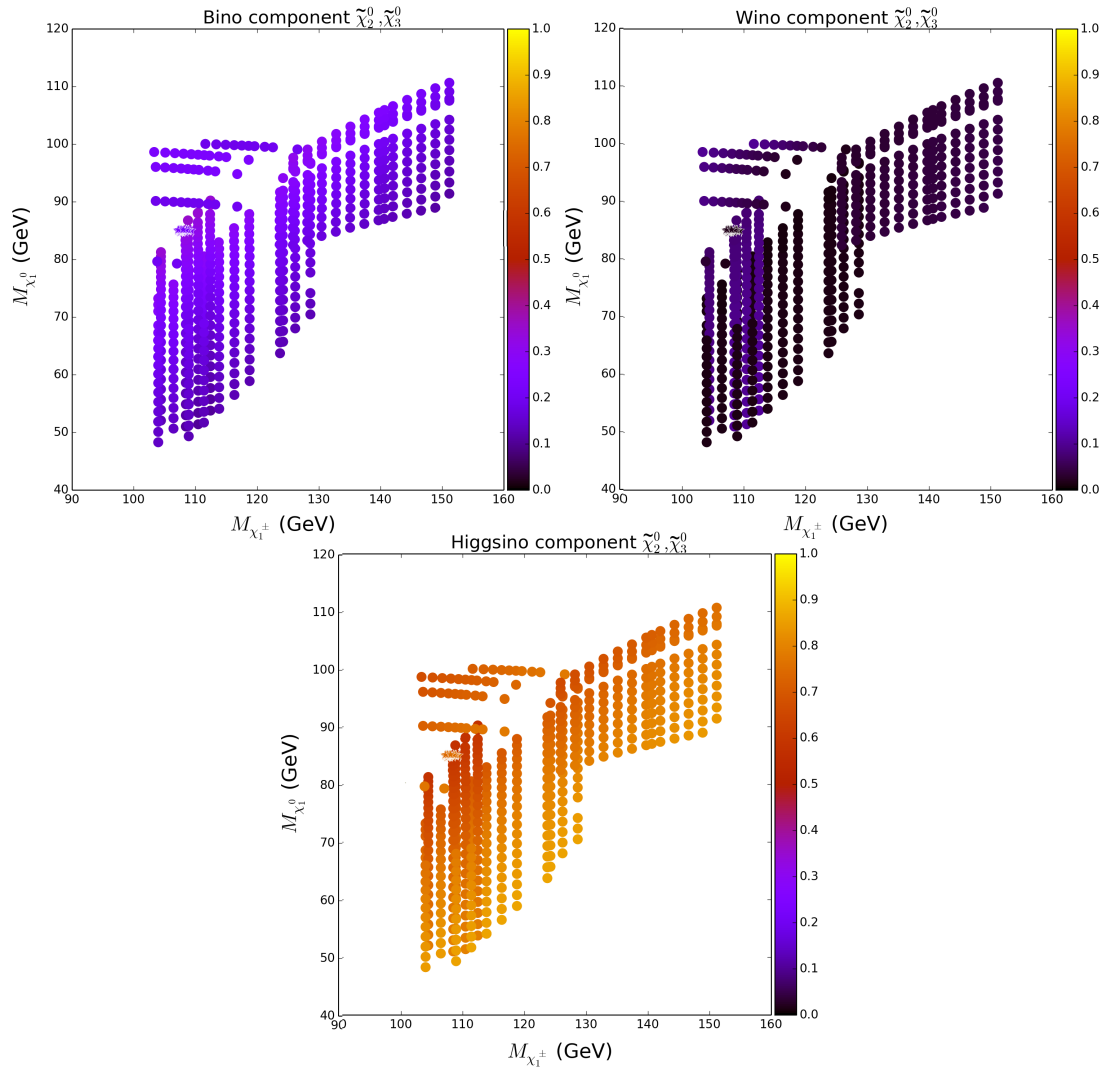


FIGURE A.5: Higgsino NLSP: Mass of $\tilde{\chi}_1^0$ as function of $m_{\tilde{\chi}_1^\pm}$ with bino, wino and higgsino composition of $\tilde{\chi}_2^0$ and $\tilde{\chi}_3^0$ as color code. The stars indicate the WW(1) GC region.

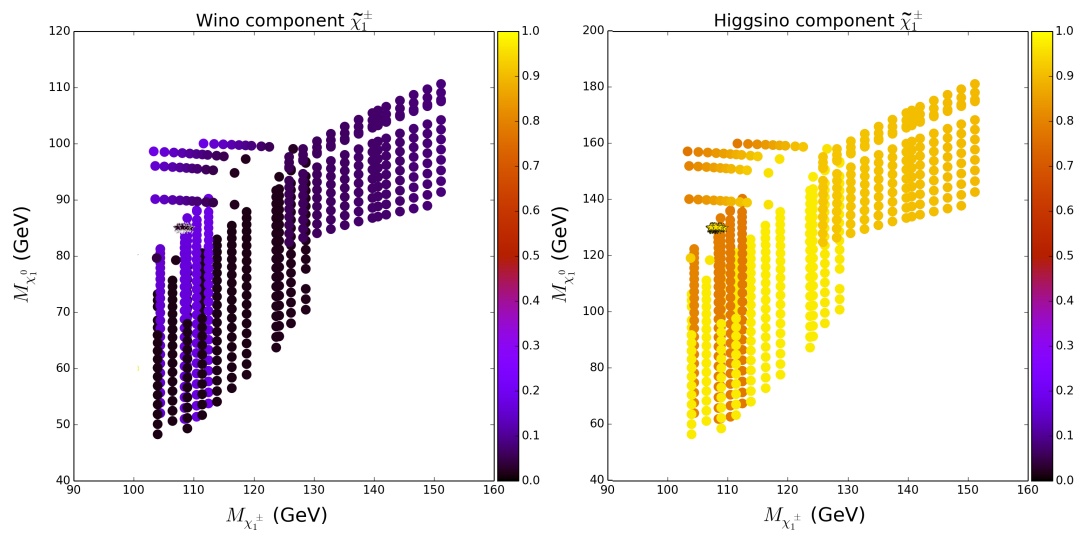


FIGURE A.6: Higgsino NLSP: Mass of $\tilde{\chi}_1^0$ as function of $m_{\tilde{\chi}_1^\pm}$ with wino and higgsino composition of $\tilde{\chi}_1^\pm$ as color code. The stars indicate the WW(1) GC region.

Appendix B

Sensitivities for different cuts and background assumptions

These figures show different significances for different assumptions on the background systematic error, luminosity and cuts. The default sets of cuts is:

- $N(l) = 3$
- $N(l^+l^-) > 0$ (at least on OSSF lepton pair)
- $5 \text{ GeV} < p_T(\mu) < 50 \text{ GeV}$ and $10 \text{ GeV} < p_T(e) < 50 \text{ GeV}$
- $12 \text{ GeV} < M(l^+l^-) < 60 \text{ GeV}$
- $p_T(j_1) < 30 \text{ GeV}$
- *Funnel cut*: $5 \text{ GeV} < \cancel{E}_T < 150 \text{ GeV}$ **and**
 - * if $\cancel{E}_T < 50 \text{ GeV}$: $p_T(l_W) + \frac{3}{5}\cancel{E}_T < 50 \text{ GeV}$
 - * else: $p_T(l_W) < 20 \text{ GeV}$
- $\Delta\phi(\cancel{E}_T, l_W) < 2$

Unless otherwise indicated, a default luminosity of 300 fb^{-1} is used. The default systematic error on the background is assumed to be 10%. The dashed gray line indicates the limit $m_{\tilde{\chi}_1^\pm} = m_{\tilde{\chi}_1^0}$. Stars indicate the WW(2) GC region in the wino NLSP plots and the WW(1) GC region in the higgsino NLSP plots.

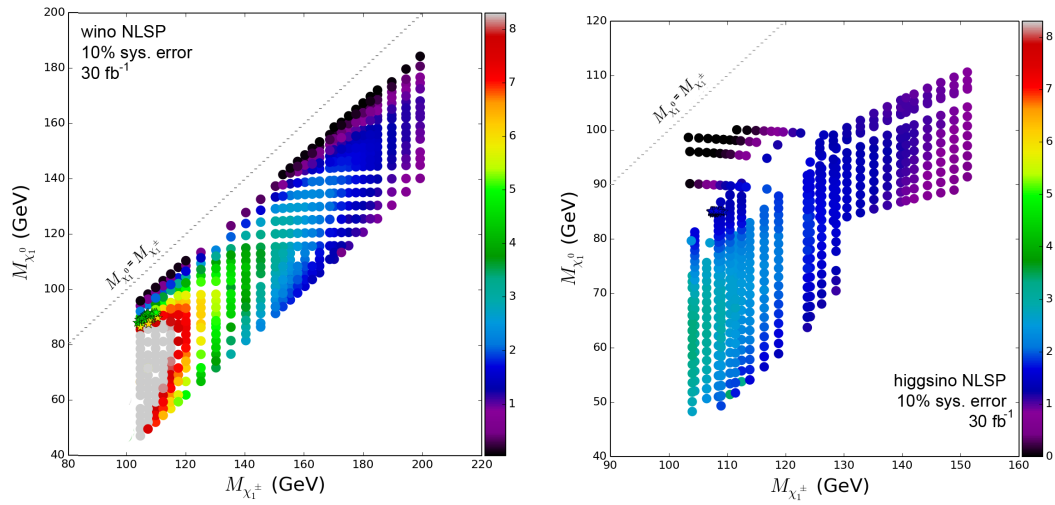


FIGURE B.1: Sensitivity for *left*: wino NLSP and *right*: higgsino NLSP models for a luminosity of 30 fb^{-1} .

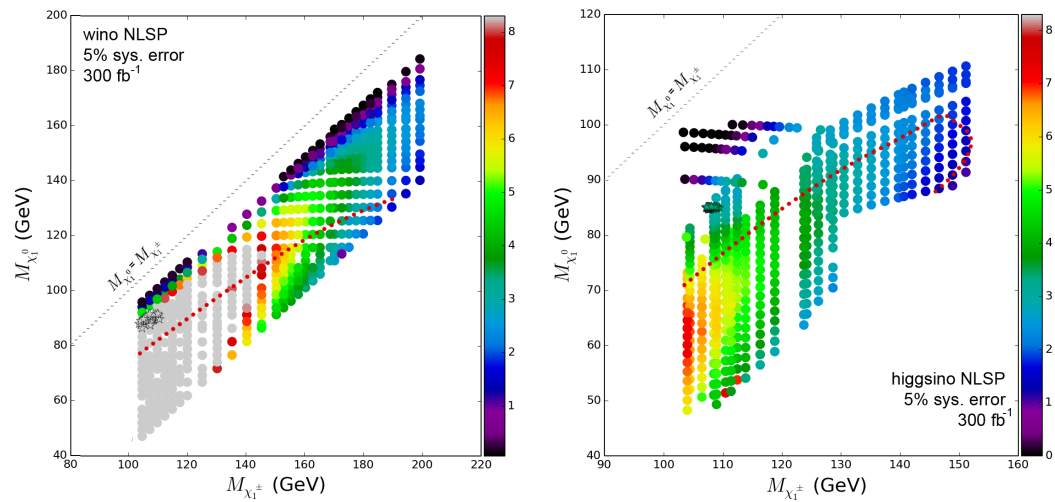


FIGURE B.2: Sensitivity for *left*: wino NLSP and *right*: higgsino NLSP models assuming a background systematic uncertainty of 5%. The dotted red line indicates the current ATLAS reach obtained for the models, assuming a background uncertainty of 5%.

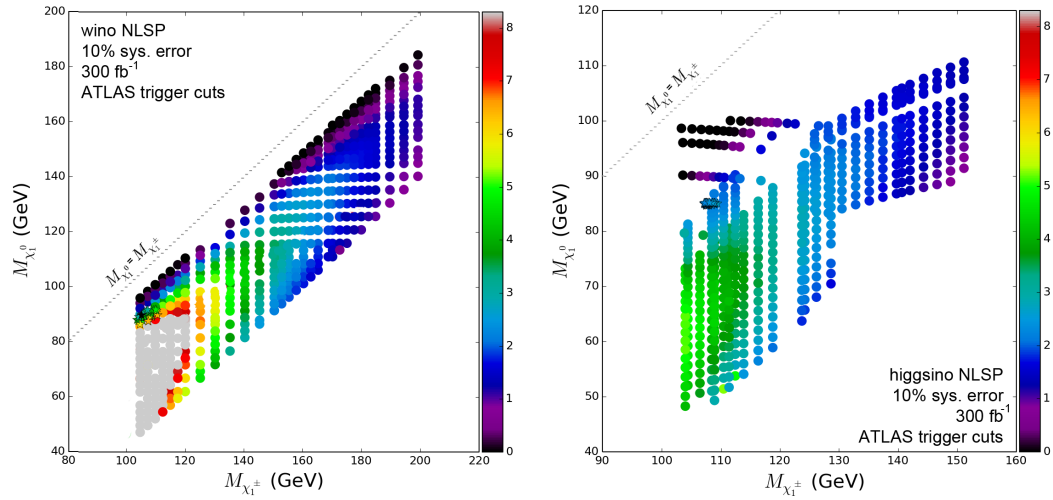


FIGURE B.3: Sensitivity for *left*: wino NLSP and *right*: higgsino NLSP models using the ATLAS trigger cuts as defined in section 5.6.1 as a requirement on the lepton transverse momenta.

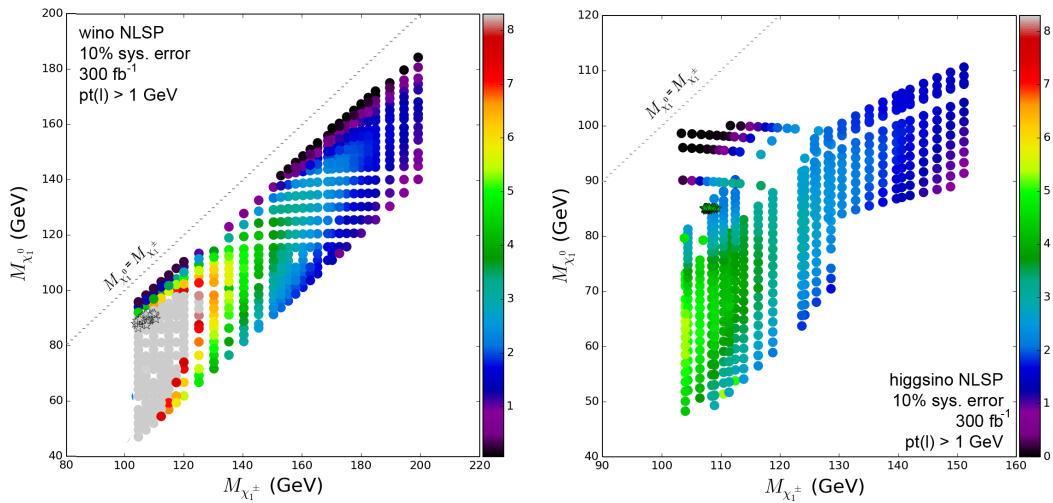


FIGURE B.4: Sensitivity for *left*: wino NLSP and *right*: higgsino NLSP models using $p_T(l) > 1$ GeV for the lepton transverse momentum.

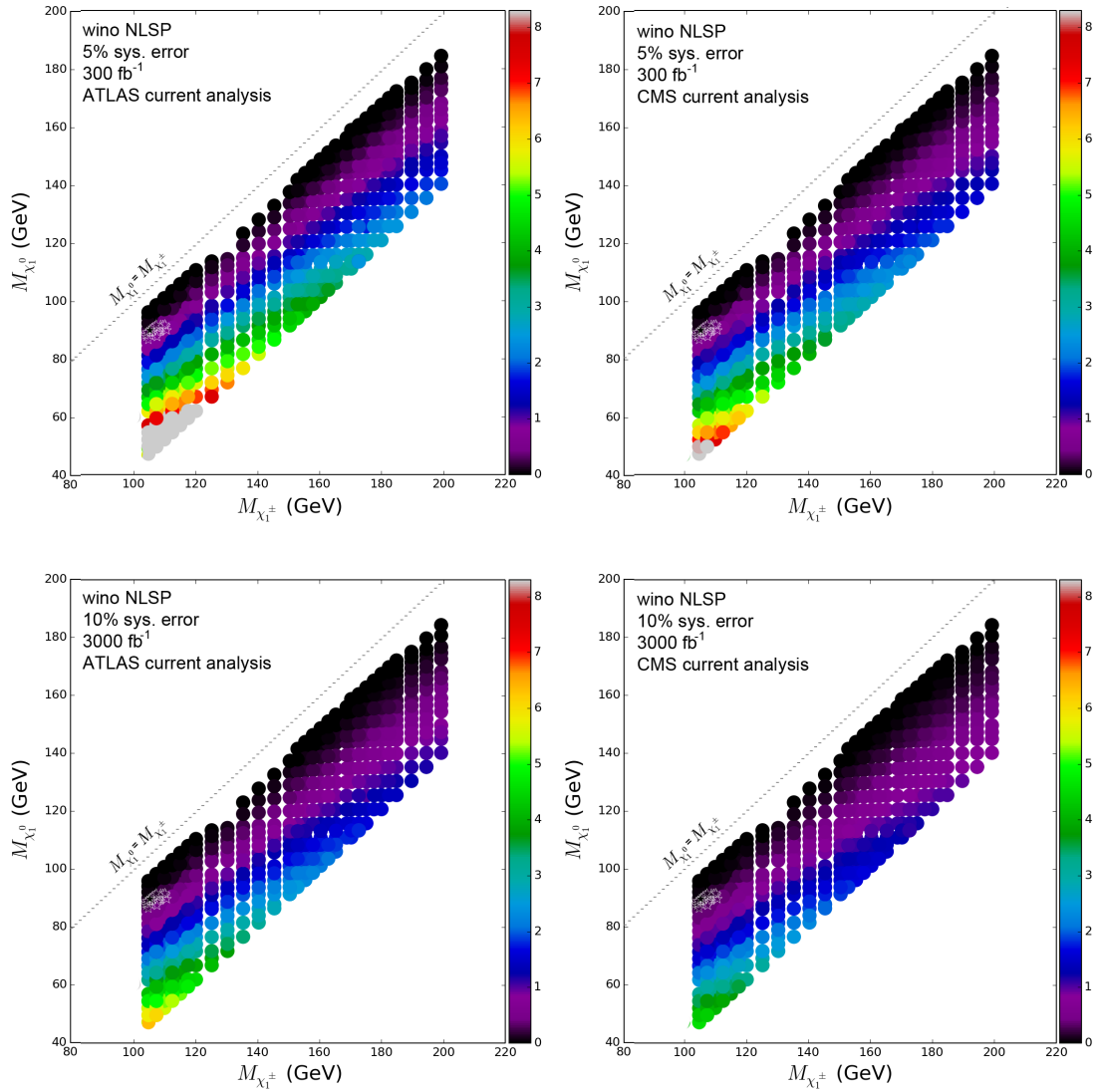


FIGURE B.5: Standard ATLAS and CMS tri-lepton searches sensitivity for the wino NLSP models. Figure (a) is made assuming a systematic background uncertainty of 5%. Figure (b) is made assuming an integrated luminosity of 3000 fb^{-1} .

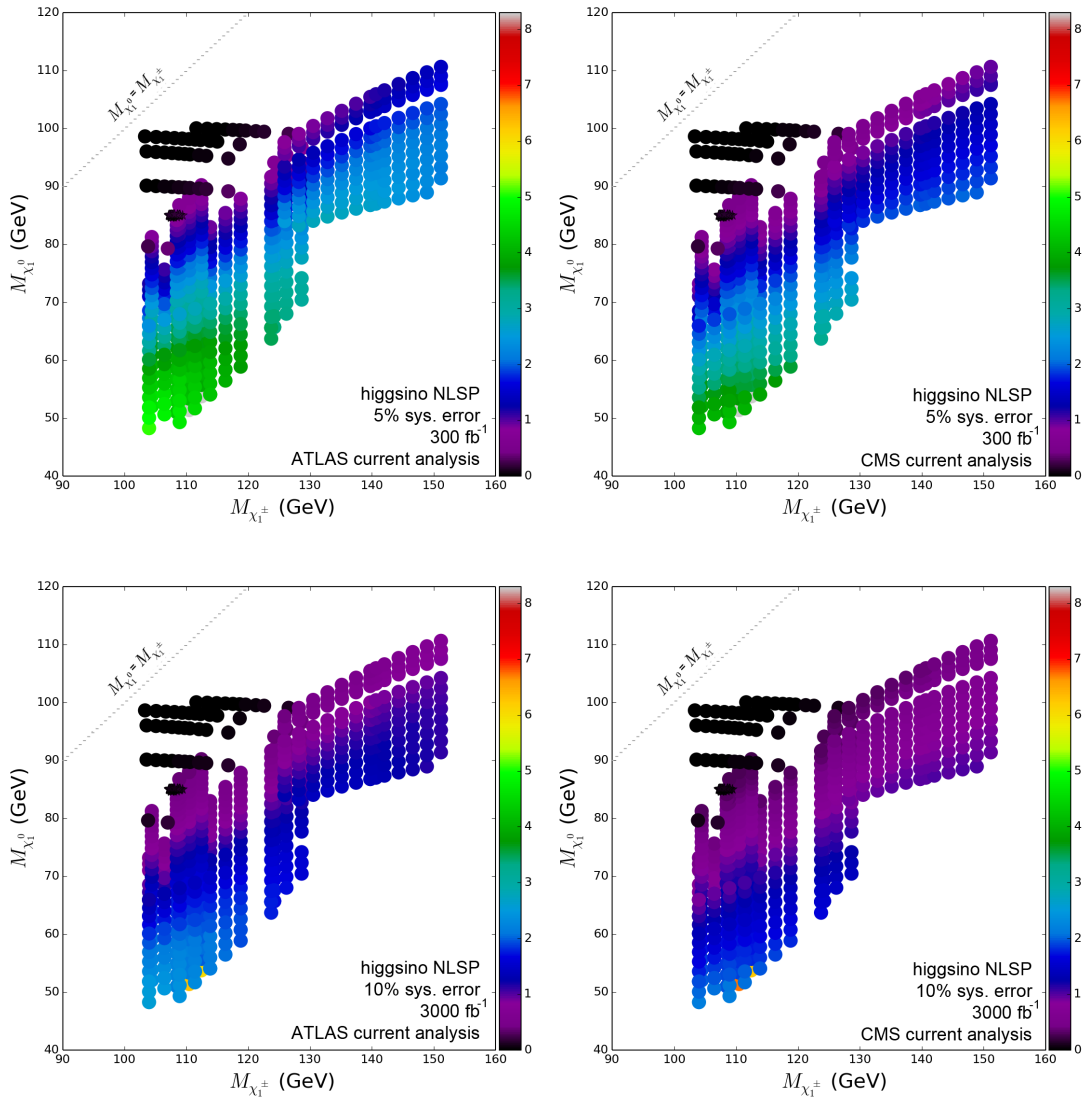


FIGURE B.6: Standard ATLAS and CMS tri-lepton searches sensitivity for the higgsino NLSP models. Figure (a) is made assuming a systematic background uncertainty of 5%. Figure (b) is made assuming an integrated luminosity of 3000 fb^{-1} .

Acronyms

ATLAS A Toroidal LHC ApparatuS

BSM Beyond the Standard Model

CMB Cosmic Microwave Background

CMS Compact Muon Solenoid

CMSSM Constrained Minimal Supersymmetric Standard Model

COBE COsmic Background Explorer

DM Dark Matter

dSph dwarf Spheriodal galaxy

FCNC Flavor Changing Neutral Currents

FSR Final State Radiation

GC Galactic Center

GUT Grand Unified Theory

ISR Initial State Radiation

LEP Large Electron Positron collider

LHC Large Hadron Collider

LHCb Large Hadron Collider beauty

LO Leading Order

LSP Lightest Supersymmetric Particle

LUX Large Underground Xenon experiment

MACHO MAssive Compact Halo Object

MOND MOdified Newtonian Dynamics

MSSM Minimal Supersymmetric Standard Model

mSUGRA minimal SUpEr GRAvity

NFW Navarro Frenk White

NLO Next-to-Leading Order

NLSP Next-to-Lightest Supersymmetric Particle

OSSF Opposite Sign Same Flavor

PDF Parton Distribution Function

PL Power Law

pMSSM phenomenological Minimal Supersymmetric Standard Model

QCD Quantum ChromoDynamics

QED Quantum ElectroDynamics

SD Spin-Dependent

SI Spin-Independent

SM Standard Model

SUSY SUpErSYmmetry

WIMP Weakly Interacting Massive Particle

WMAP Wilkinson Microwave Anisotropy Probe

XENON XENON dark matter project

Bibliography

- [1] **Planck** Collaboration, P. Ade et al., *Planck 2013 results. XVI. Cosmological parameters*, *Astron.Astrophys.* **571** (2014) A16, [[arXiv:1303.5076](#)].
- [2] K. Garrett and G. Duda, *Dark Matter: A Primer*, *Adv. Astron.* **2011** (2011) 968283, [[arXiv:1006.2483](#)].
- [3] J. L. Feng, *Dark Matter Candidates from Particle Physics and Methods of Detection*, *Ann. Rev. Astron. Astrophys.* **48** (2010) 495–545, [[arXiv:1003.0904](#)].
- [4] G. Bertone, D. Hooper, and J. Silk, *Particle dark matter: Evidence, candidates and constraints*, *Phys.Rept.* **405** (2005) 279–390, [[hep-ph/0404175](#)].
- [5] G. Bertone and J. Silk, *Particle dark matter*, p. 3. Cambridge University Press, 2010.
- [6] J. F. Navarro, C. S. Frenk, and S. D. M. White, *A Universal Density Profile from Hierarchical Clustering*, *Astrophys. J.* **490** (Dec., 1997) 493–508, [[astro-ph/9611107](#)].
- [7] J. F. Navarro, C. S. Frenk, and S. D. White, *The Structure of cold dark matter halos*, *Astrophys.J.* **462** (1996) 563–575, [[astro-ph/9508025](#)].
- [8] T. S. van Albada, J. N. Bahcall, K. Begeman, and R. Sancisi, *Distribution of dark matter in the spiral galaxy NGC 3198*, *Astrophys. J.* **295** (Aug., 1985) 305–313.
- [9] A. A. Penzias and R. W. Wilson, *A Measurement of Excess Antenna Temperature at 4080 Mc/s.*, *Astrophys. J.* **142** (July, 1965) 419–421.
- [10] M. Cirelli, G. Corcella, A. Hektor, G. Hutsi, M. Kadastik, et al., *PPPC 4 DM ID: A Poor Particle Physicist Cookbook for Dark Matter Indirect Detection*, *JCAP* **1103** (2011) 051, [[arXiv:1012.4515](#)].
- [11] E. de Blok, S. McGaugh, and V. Rubin, *High-resolution rotation curves of lsb galaxies: mass models*, *ArXiv e-prints* (2001) [[astro-ph/0107366](#)].
- [12] J. Edsjo and P. Gondolo, *Neutralino relic density including coannihilations*, *Phys. Rev.* **D56** (1997) 1879–1894, [[hep-ph/9704361](#)].
- [13] R. J. Scherrer and M. S. Turner, *On the relic, cosmic abundance of stable, weakly interacting massive particles*, *Phys. Rev.* **D33** (Mar, 1986) 1585–1589.
- [14] G. Steigman, *Cosmology confronts particle physics.*, *Annual Review of Nuclear and Particle Science* **29** (1979) 313–338.

- [15] J. L. Rosner, *The Standard model in 2001*, *ArXiv e-prints* (2001) 1–56, [[hep-ph/0108195](#)].
- [16] S. Novaes, *Standard model: An Introduction*, *ArXiv e-prints* (1999) [[hep-ph/0001283](#)].
- [17] S. Troitsky, *Unsolved problems in particle physics*, *Phys. Usp.* **55** (2012) 72–95, [[arXiv:1112.4515](#)]. [*Usp. Fiz. Nauk*182,77(2012)].
- [18] S. Dimopoulos and D. W. Sutter, *The Supersymmetric flavor problem*, *Nucl. Phys.* **B452** (1995) 496–512, [[hep-ph/9504415](#)].
- [19] M. van Beekveld, W. Beenakker, S. Caron, R. Castelijns, M. Lanfermann, and A. Strubig, *Higgs, di-Higgs and tri-Higgs production via SUSY processes at the LHC with 14 TeV*, *JHEP* **1505** (May, 2015) 44, [[arXiv:1501.02145](#)].
- [20] A. Samanta, S. K. Mandal, and H. Manna, *Is mSUGRA under tension for testing at colliders?*, *ArXiv e-prints* (Nov., 2014) [[arXiv:1411.6855](#)].
- [21] S. P. Martin, *A Supersymmetry primer*, *Adv.Ser.Direct.High Energy Phys.* **21** (2010) 1–153, [[hep-ph/9709356](#)].
- [22] **LUX** Collaboration, D. Akerib et al., *First results from the LUX dark matter experiment at the Sanford Underground Research Facility*, *Phys. Rev.* **112** (2014) 091303, [[arXiv:1310.8214](#)].
- [23] **XENON** Collaboration, E. Aprile et al., *Dark Matter Results from 225 Live Days of XENON100 Data*, *Phys. Rev.* **109** (Nov., 2012) 181301, [[arXiv:1207.5988](#)].
- [24] **XENON** Collaboration, *First limits on WIMP dark matter from the XENON10 experiment*, *J.Phys.Conf.Ser.* **110** (2008) 062020.
- [25] **DAMA** Collaboration, *Particle Dark Matter in DAMA/LIBRA*, *ArXiv e-prints* (July, 2010) [[arXiv:1007.0595](#)].
- [26] T. M. Undagoitia and L. Rauch, *Dark matter direct-detection experiments*, *ArXiv e-prints* (2015) [[arXiv:1509.08767](#)].
- [27] T. Bringmann and C. Weniger, *Gamma Ray Signals from Dark Matter: Concepts, Status and Prospects*, *Phys.Dark Univ.* **1** (2012) 194–217, [[arXiv:1208.5481](#)].
- [28] T. Daylan, D. P. Finkbeiner, D. Hooper, T. Linden, S. K. N. Portillo, et al., *The Characterization of the Gamma-Ray Signal from the Central Milky Way: A Compelling Case for Annihilating Dark Matter*, *ArXiv e-prints* (2014) [[arXiv:1402.6703](#)].
- [29] **DES, Fermi-LAT** Collaboration, A. Drlica-Wagner et al., *Search for Gamma-Ray Emission from DES Dwarf Spheroidal Galaxy Candidates with Fermi-LAT Data*, *Astrophys. J.* **809** (2015), no. 1 L4, [[arXiv:1503.02632](#)].
- [30] W. B. Atwood, A. A. Abdo, M. Ackermann, W. Althouse, B. Anderson, M. Axelsson, L. Baldini, J. Ballet, D. L. Band, G. Barbiellini, and et al., *The Large Area Telescope on the Fermi Gamma-Ray Space Telescope Mission*, *Astrophys. J.* **697** (June, 2009) 1071–1102, [[arXiv:0902.1089](#)].

- [31] **Fermi-LAT** Collaboration, M. Ackermann et al., *Searching for Dark Matter Annihilation from Milky Way Dwarf Spheroidal Galaxies with Six Years of Fermi-LAT Data*, *Phys. Rev.* **115** (Dec., 2015) 231301, [[arXiv:1503.02641](#)].
- [32] **IceCube** Collaboration, M. Aartsen et al., *Search for dark matter annihilations in the Sun with the 79-string IceCube detector*, *Phys. Rev.* **110** (2013), no. 13 131302, [[arXiv:1212.4097](#)].
- [33] **LHCb, CMS** Collaboration, V. Khachatryan et al., *Observation of the rare $B_s^0 \rightarrow \mu^+ \mu^-$ decay from the combined analysis of CMS and LHCb data*, *Nature* **522** (2015) 68–72, [[arXiv:1411.4413](#)].
- [34] L. Evans and P. Bryant, *LHC Machine*, *JINST* **3** (2008) S08001.
- [35] **ATLAS** Collaboration, G. Aad et al., *Measurement of the Higgs boson mass from the $H \rightarrow \gamma\gamma$ and $H \rightarrow ZZ^* \rightarrow 4\ell$ channels with the ATLAS detector using 25 fb^{-1} of pp collision data*, *Phys. Rev.* **D90** (2014) 052004, [[arXiv:1406.3827](#)].
- [36] **CMS** Collaboration, V. Khachatryan et al., *Precise determination of the mass of the Higgs boson and studies of the compatibility of its couplings with the standard model*, *European Physical Journal C* **75** (May, 2015) 212, [[arXiv:1412.8662](#)].
- [37] A. Arbey, M. Battaglia, A. Djouadi, F. Mahmoudi, and J. Quevillon, *Implications of a 125 GeV Higgs for supersymmetric models*, *Phys. Lett.* **B708** (2012) 162–169, [[arXiv:1112.3028](#)].
- [38] G. Benelli, *Search for stable and long lived heavy charged particles in electron positron collisions at center of mass energies from 130-GeV to 209-GeV with the OPAL detector at LEP*, . Ph.D. Thesis.
- [39] M. Carena, A. de Gouvea, A. Freitas, and M. Schmitt, *Invisible Z boson decays at $e^+ e^-$ colliders*, *Phys. Rev.* **D68** (2003) 113007, [[hep-ph/0308053](#)].
- [40] D. C. Backer and R. A. Sramek, *Proper motion of the compact, nonthermal radio source in the galactic center, sagittarius a**, *Astrophys. J.* **524** (1999), no. 2 805.
- [41] **H.E.S.S.** Collaboration, A. Abramowski et al., *Search for a Dark Matter annihilation signal from the Galactic Center halo with H.E.S.S.*, *Phys. Rev.* **106** (2011) 161301, [[arXiv:1103.3266](#)].
- [42] C. Fichtel and J. Trombka, *Gamma-Ray Astrophysics: New insight into the universe*. NASA Reference Publication, 1997.
- [43] **Fermi-LAT** Collaboration, M. Ajello et al., *Fermi-LAT Observations of High-Energy Gamma-Ray Emission Toward the Galactic Center*, *ArXiv e-prints* (2015) [[arXiv:1511.02938](#)].
- [44] J. Petrovic, P. D. Serpico, and G. Zaharijas, *Millisecond pulsars and the Galactic Center gamma-ray excess: the importance of luminosity function and secondary emission*, *JCAP* **1502** (2015), no. 02 023, [[arXiv:1411.2980](#)].
- [45] F. Calore, I. Cholis, and C. Weniger, *Background model systematics for the Fermi GeV excess*, *ArXiv e-prints* (Aug., 2014) [[arXiv:1409.0042](#)].

- [46] A. Geringer-Sameth, M. G. Walker, S. M. Koushiappas, S. E. Kopusov, V. Belokurov, G. Torrealba, and N. W. Evans, *Indication of Gamma-Ray Emission from the Newly Discovered Dwarf Galaxy Reticulum II*, *Phys. Rev.* **115** (Aug., 2015) 081101, [[arXiv:1503.02320](#)].
- [47] M. Di Mauro and F. Donato, *Composition of the Fermi-LAT isotropic gamma-ray background intensity: Emission from extragalactic point sources and dark matter annihilations*, *Phys. Rev.* **D91** (2015), no. 12 123001, [[arXiv:1501.05316](#)].
- [48] L. Goodenough and D. Hooper, *Possible Evidence For Dark Matter Annihilation In The Inner Milky Way From The Fermi Gamma Ray Space Telescope*, *ArXiv e-prints* (Oct., 2009) [[arXiv:0910.2998](#)].
- [49] A. Alves, S. Profumo, F. S. Queiroz, and W. Shepherd, *The Effective Hooperon*, *ArXiv e-prints* (2014) [[arXiv:1403.5027](#)].
- [50] M. Cahill-Rowley, J. Gainer, J. Hewett, and T. Rizzo, *Towards a Supersymmetric Description of the Fermi Galactic Center Excess*, *JHEP* **1502** (2015) 057, [[arXiv:1409.1573](#)].
- [51] A. Achterberg, S. Caron, L. Hendriks, R. Ruiz de Austri, and C. Weniger, *A description of the Galactic Center excess in the Minimal Supersymmetric Standard Model*, *JCAP* **1508** (Aug., 2015) 6, [[arXiv:1502.05703](#)].
- [52] A. Djouadi, M. M. Muhlleitner, and M. Spira, *Decays of supersymmetric particles: The Program SUSY-HIT (SUSpect-SdecaY-Hdecay-InTerface)*, *Acta Phys. Polon.* **B38** (2007) 635–644, [[hep-ph/0609292](#)].
- [53] A. Djouadi, J.-L. Kneur, and G. Moultaka, *SuSpect: A Fortran code for the supersymmetric and Higgs particle spectrum in the MSSM*, *Comput. Phys. Commun.* **176** (2007) 426–455, [[hep-ph/0211331](#)].
- [54] A. Djouadi, J. Kalinowski, and M. Spira, *HDECAY: A Program for Higgs boson decays in the standard model and its supersymmetric extension*, *Comput. Phys. Commun.* **108** (1998) 56–74, [[hep-ph/9704448](#)].
- [55] M. Muhlleitner, A. Djouadi, and Y. Mambrini, *SDECAY: A Fortran code for the decays of the supersymmetric particles in the MSSM*, *Comput. Phys. Commun.* **168** (2005) 46–70, [[hep-ph/0311167](#)].
- [56] P. Z. Skands et al., *SUSY Les Houches accord: Interfacing SUSY spectrum calculators, decay packages, and event generators*, *JHEP* **0407** (2004) 036, [[hep-ph/0311123](#)].
- [57] P. Gondolo, J. Edsjö, P. Ullio, L. Bergström, M. Schelke, E. Baltz, T. Bringmann, and G. Duda. <http://www.darksusy.org>.
- [58] G. Bélanger, F. Boudjema, A. Pukhov, and A. Semenov, *micrOMEGAs4.1: two dark matter candidates*, *Comput. Phys. Commun.* **192** (2015) 322–329, [[arXiv:1407.6129](#)].
- [59] A. Lapi, A. Paggi, A. Cavaliere, A. Lionetto, A. Morselli, and V. Vitale, *Gamma rays from annihilations at the galactic center in a physical dark matter distribution*, *Astronomy and Astrophysics* **510** (Feb., 2010) A90, [[arXiv:0912.1766](#)].

- [60] J. A. R. Cembranos, A. de la Cruz-Dombriz, A. Dobado, R. A. Lineros, and A. L. Maroto, *Photon spectra from WIMP annihilation*, *Phys. Rev.* **D83** (2011) 083507, [[arXiv:1009.4936](#)].
- [61] D. Hooper and T. Linden, *On The gamma-ray emission from Reticulum II and other dwarf galaxies*, *JCAP* **1509** (Sept., 2015) 16, [[arXiv:1503.06209](#)].
- [62] G. Battaglia, A. Helmi, and M. Breddels, *Internal kinematics and dynamical models of dwarf spheroidal galaxies around the milky way*, *New Astronomy Reviews* **57** (2013), no. 3–4 52 – 79. Galactic Archaeology.
- [63] V. Bonnavard, C. Combet, D. Maurin, A. Geringer-Sameth, S. M. Koushiappas, M. G. Walker, M. Mateo, E. W. Olszewski, and J. I. Bailey, III, *Dark Matter Annihilation and Decay Profiles for the Reticulum II Dwarf Spheroidal Galaxy*, *Astrophys. J.* **808** (Aug., 2015) L36, [[arXiv:1504.03309](#)].
- [64] **DES** Collaboration, *Stellar Kinematics and Metallicities in the Ultra-faint Dwarf Galaxy Reticulum II*, *Astrophys. J.* **808** (July, 2015) 95, [[arXiv:1504.02889](#)].
- [65] K. Bechtol et al., *Eight New Milky Way Companions Discovered in First-year Dark Energy Survey Data*, *Astrophys. J.* **807** (July, 2015) 50, [[arXiv:1503.02584](#)].
- [66] V. Bonnavard, D. Maurin, and M. G. Walker, *Sensitivity to interlopers in stellar-kinematic samples for ultrafaint dwarf galaxies: Uncertainty about the dark matter annihilation profile of Segue I*, *ArXiv e-prints* (June, 2015) [[arXiv:1506.08209](#)].
- [67] **DES** Collaboration, A. Drlica-Wagner et al., *Eight Ultra-faint Galaxy Candidates Discovered in Year Two of the Dark Energy Survey*, *Astrophys. J.* **813** (2015), no. 2 109, [[arXiv:1508.03622](#)].
- [68] S. Li et al., *Search for Gamma-ray emission from the eight newly-released DES dwarf spheroidal galaxy candidates with Fermi-LAT data*, *ArXiv e-prints* (Nov., 2015) [[arXiv:1511.09252](#)].
- [69] IceCube Collaboration, M. G. Aartsen, K. Abraham, M. Ackermann, J. Adams, J. A. Aguilar, M. Ahlers, M. Ahrens, D. Altmann, T. Anderson, and et al., *Improved limits on dark matter annihilation in the Sun with the 79-string IceCube detector and implications for supersymmetry*, *ArXiv e-prints* (Jan., 2016) [[arXiv:1601.00653](#)].
- [70] W. Beenakker, R. Hoepker, and M. Spira, *PROSPINO: A Program for the Production of Supersymmetric Particles in Next-to-leading Order QCD*, *ArXiv High Energy Physics - Phenomenology e-prints* (Nov., 1996) [[hep-ph/9611232](#)].
- [71] A. D. Martin, W. J. Stirling, R. S. Thorne, and G. Watt, *Parton distributions for the LHC*, *Eur. Phys. J.* **C63** (2009) 189–285, [[arXiv:0901.0002](#)].
- [72] T. Gleisberg, S. Höche, F. Krauss, M. Schönherr, S. Schumann, F. Siegert, and J. Winter, *Event generation with SHERPA 1.1*, *JHEP* **0902** (Feb., 2009) 007, [[arXiv:0811.4622](#)].
- [73] J. Alwall, P. C. Schuster, and N. Toro, *Simplified models for a first characterization of new physics at the LHC*, *Phys. Rev.* **79** (Apr., 2009) 075020, [[arXiv:0810.3921](#)].

- [74] V. Khachatryan et al., *Searches for electroweak production of charginos, neutralinos, and sleptons decaying to leptons and W, Z, and Higgs bosons in pp collisions at 8 TeV*, *Eur. Phys. J.* **C74** (Sept., 2014) 3036, [[arXiv:1405.7570](#)].
- [75] **ATLAS** Collaboration. https://atlas.web.cern.ch/Atlas/GROUPS/PHYSICS/CombinedSummaryPlots/SUSY/ATLAS_SUSY_EWSummary/ATLAS_SUSY_EWSummary.png.
- [76] G. F. Giudice, T. Han, K. Wang, and L.-T. Wang, *Nearly Degenerate Gauginos and Dark Matter at the LHC*, *Phys. Rev.* **D81** (2010) 115011, [[arXiv:1004.4902](#)].
- [77] K. Rolbiecki and K. Sakurai, *Constraining compressed supersymmetry using leptonic signatures*, *JHEP* **1210** (2012) 071, [[arXiv:1206.6767](#)].
- [78] P. Schwaller and J. Zurita, *Compressed electroweakino spectra at the LHC*, *JHEP* **1403** (2014) 060, [[arXiv:1312.7350](#)].
- [79] **CMS** Collaboration, *Search for electroweak production of charginos, neutralinos, and sleptons using leptonic final states in pp collisions at 8 TeV*, .
- [80] **ATLAS** Collaboration, *Search for squarks and gluinos in events with isolated leptons, jets and missing transverse momentum at 8 TeV with the ATLAS detector*, . ATLAS-CONF-2013-062.
- [81] **ATLAS** Collaboration, *Search for direct production of charginos and neutralinos in events with three leptons and missing transverse momentum in 21fb^{-1} of pp collisions at $\sqrt{s} = 8\text{ TeV}$ with the ATLAS detector*, Tech. Rep. ATLAS-CONF-2013-035, CERN, Geneva, Mar, 2013.
- [82] **ATLAS** Collaboration, *Search for the electroweak production of supersymmetric particles in $\sqrt{s}=8\text{ TeV}$ pp collisions with the ATLAS detector*, *ArXiv e-prints* (Sept., 2015) [[arXiv:1509.07152](#)].
- [83] **ATLAS** Collaboration, *Search for direct production of charginos and neutralinos in events with three leptons and missing transverse momentum in $\sqrt{s} = 8\text{ TeV}$ pp collisions with the ATLAS detector*, *ArXiv e-prints* (Feb., 2014) [[arXiv:1402.7029](#)].
- [84] H. K. Dreiner, M. Kramer, and J. Tattersall, *How low can SUSY go? Matching, monojets and compressed spectra*, *Eur. Phys. J.* **99** (2012) 61001, [[arXiv:1207.1613](#)].
- [85] M. Berggren, F. Brümmer, J. List, G. Moortgat-Pick, T. Robens, K. Rolbiecki, and H. Sert, *Tackling light higgsinos at the ILC*, *Eur. Phys. J.* **C73** (2013), no. 12 2660, [[arXiv:1307.3566](#)].
- [86] A. Delgado, G. F. Giudice, G. Isidori, M. Pierini, and A. Strumia, *The light stop window*, *Eur. Phys. J.* **C73** (2013), no. 3 2370, [[arXiv:1212.6847](#)].
- [87] **OPAL** Collaboration, G. Abbiendi et al., *Search for nearly mass degenerate charginos and neutralinos at LEP*, *Eur. Phys. J.* **C29** (2003) 479–489, [[hep-ex/0210043](#)].

- [88] **ALEPH** Collaboration, A. Heister et al., *Search for charginos nearly mass degenerate with the lightest neutralino in e^+e^- collisions at center-of-mass energies up to 209-GeV*, *Phys. Rev.* **B533** (2002) 223–236, [[hep-ex/0203020](#)].
- [89] **DELPHI** Collaboration, P. Abreu et al., *Update of the search for charginos nearly mass-degenerate with the lightest neutralino*, *Phys. Rev.* **B485** (2000) 95–106, [[hep-ex/0103035](#)].
- [90] P. Zarzhitsky, R. Kehoe, and R. Stroynowski, *Search for Supersymmetry in a Three Lepton Plus Jets Signature*. PhD thesis, Southern Methodist U., Dec, 2008. Presented 01 Nov 2008.
- [91] S. Gori, S. Jung, and L.-T. Wang, *Cornering electroweakinos at the LHC*, *JHEP* **1310** (2013) 191, [[arXiv:1307.5952](#)].
- [92] **ATLAS** Collaboration, G. Aad et al., *Search for direct production of charginos, neutralinos and sleptons in final states with two leptons and missing transverse momentum in pp collisions at $\sqrt{s} = 8$ TeV with the ATLAS detector*, *JHEP* **1405** (2014) 071, [[arXiv:1403.5294](#)].
- [93] J. Cao, Y. He, L. Shang, W. Su, and Y. Zhang, *Testing the light dark matter scenario of the MSSM at the LHC*, *ArXiv e-prints* (2015) [[arXiv:1511.05386](#)].
- [94] **ATLAS** Collaboration, *Search for direct production of charginos and neutralinos in events with three leptons and missing transverse momentum in 13.0 fb⁻¹ of pp collisions at $\sqrt{s}=8$ TeV with the ATLAS detector*, .
- [95] **ATLAS** Collaboration, G. Aad et al., *Search for direct production of charginos and neutralinos in events with three leptons and missing transverse momentum in $\sqrt{s} = 7$ TeV pp collisions with the ATLAS detector*, *Phys. Rev.* **B718** (2013) 841–859, [[arXiv:1208.3144](#)].
- [96] **ATLAS** Collaboration, G. Aad et al., *Search for direct slepton and gaugino production in final states with two leptons and missing transverse momentum with the ATLAS detector in pp collisions at $\sqrt{s} = 7$ TeV*, *Phys. Rev.* **B718** (2013) 879–901, [[arXiv:1208.2884](#)].
- [97] **ATLAS** Collaboration, *Search for direct production of charginos and neutralinos in events with three leptons and missing transverse momentum in 21 fb⁻¹ of pp collisions at $\sqrt{s} = 8$ TeV with the ATLAS detector*, .
- [98] **CMS** Collaboration, S. Chatrchyan et al., *Search for electroweak production of charginos and neutralinos using leptonic final states in pp collisions at $\sqrt{s} = 7$ TeV*, *JHEP* **1211** (2012) 147, [[arXiv:1209.6620](#)].
- [99] **CMS** Collaboration, M. Sigamani, *SUSY searches in CMS*, in *20th International Symposium on Particles, Strings and Cosmology (PASCOS 2014) Warsaw, Poland, June 22-27, 2014*, 2014. [arXiv:1411.0250](#).
- [100] **CMS** Collaboration, V. Khachatryan et al., *Searches for electroweak production of charginos, neutralinos, and sleptons decaying to leptons and W , Z , and Higgs bosons in pp collisions at 8 TeV*, *Eur. Phys. J.* **C74** (2014), no. 9 3036, [[arXiv:1405.7570](#)].

- [101] CMS Collaboration, *Performance of CMS muon reconstruction in pp collision events at $\sqrt{s} = 7$ TeV*, *Journal of Instrumentation* **7** (Oct., 2012) 2P, [[arXiv:1206.4071](#)].
- [102] J. Alwall, M. Herquet, F. Maltoni, O. Mattelaer, and T. Stelzer, *MadGraph 5 : Going Beyond*, *JHEP* **1106** (2011) 128, [[arXiv:1106.0522](#)].
- [103] F. Maltoni and T. Stelzer, *MadEvent: automatic event generation with MadGraph*, *Journal of High Energy Physics* **2** (Feb., 2003) 27, [[hep-ph/0208156](#)].
- [104] T. Sjostrand, S. Mrenna, and P. Z. Skands, *A Brief Introduction to PYTHIA 8.1*, *Comput. Phys. Commun.* **178** (2008) 852–867, [[arXiv:0710.3820](#)].
- [105] M. Cacciari, G. P. Salam, and G. Soyez, *FastJet User Manual*, *Eur. Phys. J.* **C72** (2012) 1896, [[arXiv:1111.6097](#)].
- [106] DELPHES 3 Collaboration, *DELPHES 3, A modular framework for fast simulation of a generic collider experiment*, *JHEP* **1402** (2014) 057, [[arXiv:1307.6346](#)].
- [107] J. Alwall, S. Höche, F. Krauss, N. Lavesson, L. Lönnblad, F. Maltoni, M. L. Mangano, M. Moretti, C. G. Papadopoulos, F. Piccinini, S. Schumann, M. Treccani, J. Winter, and M. Worek, *Comparative study of various algorithms for the merging of parton showers and matrix elements in hadronic collisions*, *Eur. Phys. J.* **C53** (Feb., 2008) 473–500, [[arXiv:0706.2569](#)].
- [108] J. Linnemann, *Measures of Significance in HEP and Astrophysics*, in *Statistical Problems in Particle Physics, Astrophysics, and Cosmology* (L. Lyons, R. Mount, and R. Reitmeyer, eds.), p. 35, 2003. [[physics/0312059](#)].
- [109] K. J. de Vries, E. A. Bagnaschi, O. Buchmueller, R. Cavanaugh, M. Citron, A. De Roeck, M. J. Dolan, J. R. Ellis, H. Flücher, S. Heinemeyer, G. Isidori, S. Malik, J. Marrouche, D. M. Santos, K. A. Olive, K. Sakurai, and G. Weiglein, *The pMSSM10 after LHC run 1*, *Eur. Phys. J.* **C75** (Sept., 2015) 422, [[arXiv:1504.03260](#)].
- [110] E. A. Bagnaschi et al., *Supersymmetric Dark Matter after LHC Run 1*, *Eur. Phys. J.* **C75** (2015) 500, [[arXiv:1508.01173](#)].
- [111] G. Bertone, F. Calore, S. Caron, R. Ruiz de Austri, J. S. Kim, R. Trotta, and C. Weniger, *Global analysis of the pMSSM in light of the Fermi GeV excess: prospects for the LHC Run-II and astroparticle experiments*, *ArXiv e-prints* (July, 2015) [[arXiv:1507.07008](#)].
- [112] A. Achterberg, M. van Beekveld, W. Beenakker, S. Caron, and L. Hendriks, *Comparing Galactic Center MSSM dark matter solutions to the Reticulum II gamma-ray data*, *JCAP* **1512** (2015), no. 12 013, [[arXiv:1507.04644](#)].
- [113] M. van Beekveld, W. Beenakker, S. Caron, and R. R. de Austri, *The case for 100 GeV bino dark matter: A dedicated LHC tri-lepton search*, [[arXiv:1602.00590](#)].